Epitaxy and Spectroscopy of Two-Dimensional Adatom Systems: the Elemental Topological Insulator Indenene on SiC

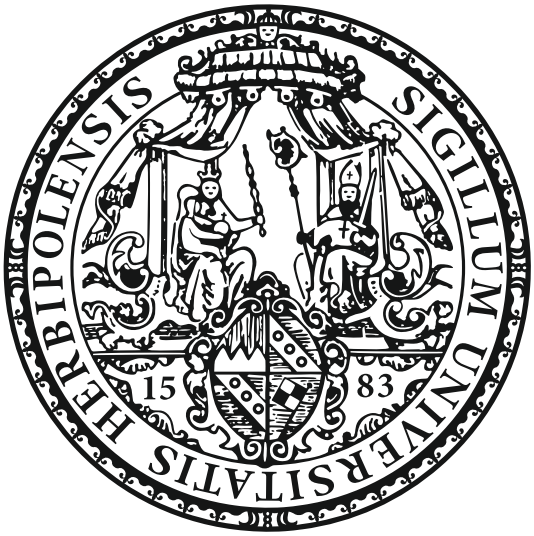

Dissertation zur Erlangung des
naturwissenschaftlichen Doktorgrades
der Julius-Maximilians-Universität Würzburg

vorgelegt von

Maximilian Josef Xaver Bauernfeind
aus Heilbronn

Würzburg 2022

Eingereicht am: 11. Juli 2022

bei der Fakultät für Physik und Astronomie

1. Gutachter: Prof. Dr. Jörg Schäfer

2. Gutachter: Prof. Dr. Matthias Bode

3. Gutachter:

der Dissertation

Vorsitzender: Prof. Dr. Haye Hinrichsen

1. Prüfer: Prof. Dr. Jörg Schäfer

2. Prüfer: Prof. Dr. Matthias Bode

3. Prüfer: Prof. Dr. Giorgio Sangiovanni

im Promotionskolloquium

Tag des Promotionskolloquiums: 03. Februar 2023

Doktorurkunde ausgehändigt am:

Abstract

Two-dimensional (2D) topological insulators are a new class of materials with properties that are promising for potential future applications in quantum computers. For example, stanene represents a possible candidate for a topological insulator made of Sn atoms arranged in a hexagonal lattice. However, it has a relatively fragile low-energy spectrum and sensitive topology. Therefore, to experimentally realize stanene in the topologically non-trivial phase, a suitable substrate that accommodates stanene without compromising these topological properties must be found. A heterostructure consisting of a SiC substrate with a buffer layer of adsorbed group-III elements constitutes a possible solution for this problem. In this work, 2D adatom systems of Al and In were grown epitaxially on SiC(0001) and then investigated structurally and spectroscopically by scanning tunneling microscopy (STM) and photoelectron spectroscopy.

Al films in the high coverage regime ($\Theta_{ML} \approx 2$ ML) exhibit unusually large, triangular- and rectangular-shaped surface unit cells. Here, the low-energy electron diffraction (LEED) pattern is brought into accordance with the surface topography derived from STM. Another Al reconstruction, the quasi-one-dimensional (1D) Al phase, exhibits a striped surface corrugation, which could be the result of the strain imprinted by the overlayer-substrate lattice mismatch. It is suggested that Al atoms in different surface areas can occupy hexagonal close-packed and face-centered cubic lattice sites, respectively, which in turn lead to close-packed transition regions forming the stripe-like corrugations. On the basis of the well-known herringbone reconstruction from Au(111), a first structural model is proposed, which fits well to the structural data from STM. Ultimately, however, thermal treatments of the sample could not generate lower coverage phases, i.e. in particular, a buffer layer structure.

Strong metallic signatures are found for In high coverage films ($\Theta_{ML} \approx 3$ to ≈ 2 ML) by scanning tunneling spectroscopy (STS) and angle-resolved photoelectron spectroscopy (ARPES), which form a (7×7), $(6 \times 4\sqrt{3})$, and $(4\sqrt{3} \times 4\sqrt{3})$ surface reconstruction. In all these In phases electrons follow the nearly-free electron model. Similar to the Al films, thermal treatments could not obtain the buffer layer system.

Surprisingly, in the course of this investigation a triangular In lattice featuring a (1×1) periodicity is observed to host massive Dirac-like bands at K/K' in ARPES. Based on this strong electronic similarity with graphene at the Brillouin zone boundary, this new structure is referred to as *indenene*. An extensive theoretical analysis uncovers the emergence of an electronic honeycomb network based on triangularly arranged In p orbitals. Due to strong atomic spin-orbit coupling and a comparably small substrate-induced in-plane inversion symmetry breaking this

material system is rendered topologically non-trivial. In indenene, the topology is intimately linked to a bulk observable, i.e., the energy-dependent charge accumulation sequence within the surface unit cell, which is experimentally exploited in STS to confirm the non-trivial topological character. The band gap at K/K', a signature of massive Dirac fermions, is estimated by ARPES to approximately 125 meV. Further investigations by X-ray standing wave, STM, and LEED confirm the structural properties of indenene. Thus, this thesis presents the growth and characterization of the novel quantum spin Hall insulator material indenene.

Zusammenfassung

Zweidimensionale (2D) topologische Isolatoren sind eine neue Materialklasse mit vielversprechenden Eigenschaften für potenzielle zukünftige Anwendungen in Quantencomputern. Stanene stellt hier beispielsweise einen möglichen Kandidaten für einen topologischen Isolator dar. Diese 2D-Schicht besteht aus Sn-Atomen, angeordnet in einem hexagonalen Gitter. Allerdings weist dieses Gitter ein relativ fragiles Niederenergiespektrum und eine empfindliche Topologie auf. Um Stanene daher in der topologisch nicht-trivialen Phase experimentell realisieren zu können, muss ein geeignetes Substrat gefunden werden, das Stanene aufnehmen kann, ohne die topologischen Eigenschaften zu beeinträchtigen. Eine Heterostruktur aus einem SiC-Substrat mit einer Pufferschicht aus adsorbierten Gruppe-III Elementen stellt hier eine mögliche Lösung für dieses Problem dar. Im Hinblick darauf wurden für diese Arbeit 2D-Adatomsysteme aus Al und In epitaktisch auf SiC(0001) gewachsen und mittels Rastertunnelmikroskopie (engl.: scanning tunneling microscopy, STM) und Photoelektronenspektroskopie strukturell und spektroskopisch untersucht.

Al-Schichten mit hoher Bedeckung ($\Theta_{ML} \approx 2$ ML) weisen ungewöhnlich große, dreieckig und rechteckig geformte Oberflächeneinheitszellen auf. Hierbei wird das Beugungsmuster der niederenergetischen Elektronenbeugung (engl.: low-energy electron diffraction, LEED) mit der aus STM abgeleiteten Oberflächentopographie in Einklang gebracht. Eine andere Al-Rekonstruktion, die quasi-eindimensionale (1D) Al-Phase, zeigt eine gestreifte Oberflächenkorrugation, die ein Ergebnis der Verspannung durch die Fehlanpassung des Al-Gitters auf dem Substratgitter sein könnte. Es wird vorgeschlagen, dass Al-Atome in verschiedenen Oberflächenbereichen sowohl jeweils hexagonal-dichtgepackte als auch kubisch flächenzentrierte Gitterplätze einnehmen können. In Übergangsregionen zwischen beiden Bereichen erzeugt dies dicht gepackte Al-Atome, die wiederum die streifenartigen Korrugationen hervorrufen. Auf der Basis der bekannten Fischgrätenrekonstruktion von Au(111) wird ein erstes Strukturmodell vorgeschlagen, das gut mit strukturellen STM-Daten übereinstimmt. Letztendlich konnten jedoch durch thermische Behandlungen der Probe keine Phasen mit geringerer Bedeckung, das heißt insbesondere die Pufferschichtstruktur, erzeugt werden.

In-Hochbedeckungsphasen ($\Theta_{ML} \approx 3$ bis ≈ 2 ML) weisen ein ausgeprägtes metallisches Verhalten auf in der Rastertunnelspektroskopie (engl.: scanning tunneling spectroscopy, STS) und winkelaufgelösten Photoelektronenspektroskopie (engl.: angle-resolved photoelectron spectroscopy, ARPES). Zudem bilden diese Phasen eine (7×7)-, $(6\times4\sqrt{3})$-, und $(4\sqrt{3}\times4\sqrt{3})$-Oberflächenrekonstruktion aus. In all diesen Phasen folgen die Elektronen dem Modell der quasifreien Elek-

tronen. Ähnlich zu den Al-Filmen konnte auch hier nach thermischen Behandlungen der Probe keine Pufferschichtstruktur erzeugt werden.

Überraschenderweise tritt im Laufe dieser Untersuchung ein Dreiecksgitter aus In-Atomen mit einer (1×1)-Periodizität auf, das bei K/K' massive Dirac-artige Bänder in ARPES zeigt. Aufgrund der starken Ähnlichkeit mit der Graphene-Bandstruktur am Brillouinzonenrand, wird dieses neuartige Materialsystem *Indenene* benannt. Eine umfangreiche theoretische Untersuchung legt die Entstehung eines elektronischen Honigwabennetzwerks offen, dass sich aufgrund von dreieckig angeordneten In p-Orbitalen bildet. Durch starke atomare Spin-Bahn-Wechselwirkung und einen vergleichsweisen schwachen substratinduzierten Inversionssymmetriebruch in der Ebene, ist dieses Materialsystem topologisch nicht-trivial. In Indenene ist die Topologie eng mit einer Volumenobservablen, genauer die energieabhängige Ladungsakkumulationsequenz innerhalb der Oberflächeneinheitszelle, verknüpft. Diese Sequenz wird mittels STS experimentell ausgenutzt, um den topologisch nicht-trivialen Charakter zu bestätigen. Die Bandlücke bei K/K', charakteristisch für massive Dirac-Fermionen, wird mittels ARPES auf ungefähr 125 meV abgeschätzt. Weitere Untersuchungen basierend auf stehenden Röntgenwellen, STM, und LEED bestätigen die strukturellen Eigenschaften von Indenene. Dementsprechend wird in dieser Arbeit das Wachstum und auch die Charakterisierung des neuartigen Quanten Spin Hall Isolators Indenene vorgestellt.

Contents

List of acronyms

2D	two-dimensional
1D	one-dimensional
LEED	low-energy electron diffraction
STM	scanning tunneling microscopy
STS	scanning tunneling spectroscopy
PES	photoelectron spectroscopy
ARPES	angle-resolved photoelectron spectroscopy
XPS	X-ray photoelectron spectroscopy
XSW	X-ray standing wave
NIXSW	normal incidence X-ray standing wave
AFM	atomic force microscopy
TEM	transmission electron microscopy
DFT	density functional theory
PBE	Perdew-Burke-Ernzerhof
HSE	Heyd–Scuseria–Ernzerhof
FFT	fast Fourier transform
DOS	density of states
LDOS	local density of states
CITS	current imaging tunneling spectroscopy
ZBA	zero-bias anomaly
EDC	energy distribution curve
MDC	momentum distribution curve
ISB	inversion symmetry breaking
OAM	orbital angular momentum
UHV	ultra-high vacuum
VUV	vacuum ultraviolet

hcp hexagonal close-packed

fcc face-centered cubic

CEC constant energy contour

QHE quantum Hall effect

SOC spin-orbit coupling

QSHE quantum spin Hall effect

QSHI quantum spin Hall insulator

List of Figures

List of Tables

1 Introduction

Given the limited further miniaturization of transistor components, the computer industry is currently undergoing a profound transformation in which new types of computers are being explored. In the future, quantum computing could replace the "classical" way of processing information by using *qubits*, especially for certain computationally intensive tasks [1]. This fundamentally different computer architecture may circumvent the miniaturization limit of current computers.

Topological insulators are promising candidates for use in quantum computing devices [2–4]. Their 2D version, also called a quantum spin Hall insulator (QSHI), is the focus here due to the importance of miniaturizing potential devices. This new class of materials accommodates spin-polarized, counter-propagating edge currents at their boundary, allowing dissipationless electron transport while their interior remains insulating [5, 6]. Moreover, electrons at these interfaces exhibit a linear band dispersion, which renders them Dirac fermions. All of these properties are protected by the fundamental time-reversal symmetry and were first demonstrated experimentally in the quantum spin Hall effect (QSHE) in a HgTe quantum well structure [7]. In the last 15 years, enormous efforts have been made worldwide to explore novel topological materials. The main objective is to find material candidates with a technologically relevant band gap that will allow potential applications at room temperature and above. References [8, 9] provide here an overview of this active research field.

Graphene, the purely 2D hexagonal carbon lattice, is another famous candidate predicted to host a quantum spin Hall insulating phase [10, 11]. Based on the model from Kane and Mele, the inherently present spin-orbit coupling (SOC) renders this material non-trivial [10, 11]. However, SOC enters as a second-nearest neighbor hopping term, which results in a minute band gap at K/K' on the order of $1\,\mu\text{eV}$ [12, 13]. Since the size of the non-trivial band gap in general scales with the atomic SOC, hexagonal lattices made of high-Z elements offer a more promising route. Extensive research has been conducted on buckled group-IV graphene analogs such as silicene (Si), germanene (Ge), and stanene (Sn) [14, 15]. With the exception of silicene, all exhibit relevant band gap sizes in their freestanding form. However, in order to utilize these graphene analogs technologically, these 2D lattices must be synthesized on a substrate. It is important to note, however, that a substrate can strongly influence the structural, electronic, and topological properties of the adlayers. Stanene, for example, was experimentally realized on three-fold symmetric (111) surfaces of various metallic substrates such as Ag, Au, Sb, Cu, and Bi_2Te_3 [16–23]. In all these cases, the strong substrate interaction renders stanene metallic, which promotes the hybridization of the edge states with substrate surface states and eventually

prevents a quantized edge state transport. Moreover, due to strong compressive strain stanene exhibits a trivially insulating ground state on PbTe(111) [24]. Also germanene renders metallic when accommodated on MoS_2 [25].

It is therefore crucial to find a suitable substrate that matches the symmetry and lattice constant of the 2D layers without compromising their sensitive electronic and topological properties. Si-terminated SiC(0001) is an insulating substrate that fulfills all requirements described above to accommodate stanene [26, 27]. Nevertheless, strong covalent bonding of stanene to the substrate would be detrimental for the topological character. Passivating the dangling bonds on the substrate surface with hydrogen would result in a weak van der Waals-like bonding of the adlayer [26], which would be challenging for its epitaxial growth.

Group-III elements are well-known to passivate other semiconductor surfaces efficiently, since one adatom is covalently bonded to three unsaturated bonds on the (111) plane [28, 29]. In a collaborative study, Di Sante *et al.* proposed therefore to use a buffer layer made of group-III elements between the SiC substrate and stanene [27]. By doing so, the passivated surface reduces the stanene-substrate interaction, leaving the non-trivial properties intact. At the same time, the bonding is still sufficiently strong enough to support stanene on a substrate. Since Al and In are known for passivating the structurally related Si(111) surface [28–31], both elements were chosen as buffer layer material here.

This is the starting point of this dissertation with the goal of experimentally synthesizing buffer layers of Al and In on SiC(0001) and subsequently characterizing their structural and spectroscopic properties. In pursuing this goal, a triangular monolayer of In atoms was surprisingly found to feature massive Dirac fermions based on an electronic hidden honeycomb network. Moreover, the influence of the substrate enables the robust classification of the topological character purely on bulk-observables in contrast to commonly employed edge state spectroscopy. The simple triangular geometry allows for large-scale domain growth that utilizes edge state transport, which is technologically valuable. Hence, this novel QSHI opens up a new design concept for non-trivial quantum matter, which are also potentially relevant in quantum computing.

The thesis structure is as follows: In Chapter 2 the theoretical basis of topology in hexagonal lattices and the buffer layer concept will be presented. Chapter 3 will introduce structural and electronic properties as well as the surface preparation method of the 4H-SiC(0001) substrate. An overview of different experimental surface analysis methods utilized in this work will be given in Chapter 4. The epitaxial growth of buffer layers on SiC(0001) made of aluminum and indium will be discussed in the subsequent Chapters 5 and 6. The occurrence of massive Dirac fermions in an indium monolayer – *indenene* – sparked a thorough theoretical analysis on the emergent honeycomb connectivity, which will be presented in Chapter 7. Subsequently, Chapter 8 will focus on a full experimental characterization of indenene with the topological classification based on bulk observables detected in STS. Lastly, a general conclusion and outlook will be given in Chapter 9.

2 Theoretical background of the buffer layer concept on SiC(0001)

The demand for a buffer layer made of group-III elements on SiC(0001) to host a decoupled stanene layer will be addressed from a theoretical stand point in this chapter. Using graphene, topologically non-trivial properties of 2D hexagonal lattices will be derived on a general basis, eventually culminating in the Kane-Mele model, where SOC plays the crucial role. The resulting minute topological band gap at K/K' can be boosted by utilizing high-Z group-IV elements such as tin (stanene), which render these graphene analogs technologically promising QSHI candidates. In order to preserve their sensitive topology on a substrate, however, a buffer layer is necessary to decouple the graphene analog from detrimental substrate interactions, as it will be exemplarily demonstrated for stanene. Here, aluminum and indium are identified as promising group-III elements for the realization of a buffer layer on SiC(0001).

2.1 Graphene and the Kane-Mele model

2.1.1 Lattice structure and tight-binding model

The fundamental crystal structure of graphene, a planar 2D layer of hexagonally arranged carbon atoms, is depicted in Figure 2.1a. The lattice unit cell (gray rhombus) is spanned by the vectors $\boldsymbol{a}_1$ and $\boldsymbol{a}_2$. Within this unit cell a bipartite atomic basis is present, which creates two equivalent sublattices A and B (blue and red circles, respectively) rotated by 120° with respect to each other. In the flat graphene layer the orbitals of the C atoms undergo a sp^2 hybridization [32, 33]. This results in three in-plane oriented, energetically degenerate sp hybridization orbitals, which are responsible for the in-plane covalent bonding (σ-bonding) between neighboring C atoms. In addition, non-hybridized p_z orbitals pointing out of the 2D layer create an out-of-plane covalent π-bonding. Because the in-plane bonding is much stronger than the π-bonding, the σ-bonding and -antibonding states are energetically far away from the Fermi level [32]. Only the π-states in the low-energy sector of graphene are pivotal for the relevant physics, including the quantum spin Hall insulating phase, which will be discussed in more detail. The low-energy electronic dispersion of these states can be expressed within the tight-binding formalism as [34]:

$$E^{\pm}(\boldsymbol{k}) = \frac{\epsilon_{2p} \pm \gamma_0 \sqrt{f(\boldsymbol{k})}}{1 \pm s_0 \sqrt{f(\boldsymbol{k})}} \text{ with } f(\boldsymbol{k}) = 1 + 4\cos^2\left(\frac{k_y a}{2}\right) + 4\cos\left(\frac{\sqrt{3}k_x a}{2}\right)\cos\left(\frac{k_y a}{2}\right). \quad (2.1)$$

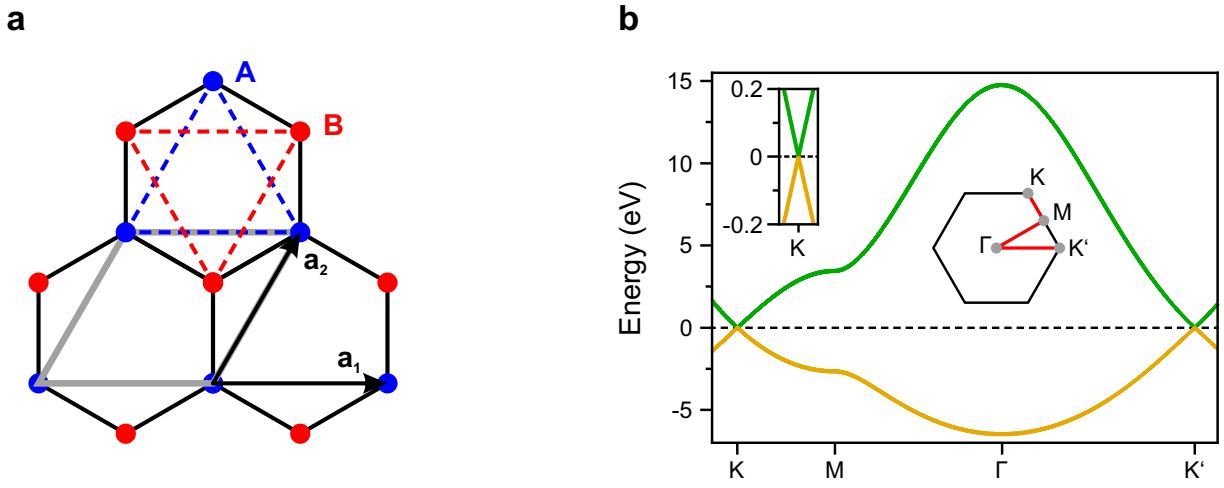

Figure 2.1: Structural and electronic properties of graphene – **a**, Schematic illustration of the 2D hexagonal graphene lattice spanned by the lattice vectors $\boldsymbol{a}_1$ and $\boldsymbol{a}_2$. The unit cell is depicted in gray. Both sublattices A and B connect the next-nearest-neighbors in the lattice with blue and red dashed lines, respectively. **b**, Tight-binding derived band structure along $\overline{KM\Gamma K'}$ (see schematic) of graphene based on Equation 2.1 with the orbital energy of the $2p$ level $\epsilon_{2p} = 0$, the hopping/transfer integral $\gamma_0 = -3$, and the overlap integral $s_0 = -0.13$. Inset: The zoom-in highlights the linear dispersing bands at and around K/K' with the Dirac point at zero energy.

In Equation 2.1 only the nearest-neighbor interactions are included. The + and − indicate the valence and conduction states, respectively. Plotting this band dispersion along $\overline{KM\Gamma K'}$ yields a distinctive band crossing of the valence and conduction band at the corner of the Brillouin zone, the K/K' points (see Fig. 2.1b). In the vicinity of those points, the bands disperse linearly and electrons behave as massless Dirac particles [35, 36]. Therefore, the Dirac-Hamiltonian can be expressed as follows close to the K points:

$$H(\boldsymbol{k}) = v(\tau_z k_x \sigma_x + k_y \sigma_y), \tag{2.2}$$

where v is the Fermi velocity, and $\boldsymbol{\tau}$ and $\boldsymbol{\sigma}$ represent the Pauli matrices for the valley and sublattice degree of freedom, respectively [37].

For a potential technological application as a digital transistor, for instance, an energy gap between the valence and conduction band is necessary [38]. This can be introduced via a diagonal mass term that renders the sublattices inequivalent and break the inversion symmetry [36, 37]. A staggered sublattice potential for example lifts the doubly degenerate bands at the K points and renders the Dirac Hamiltonian [37]:

$$H(\boldsymbol{k}) = v(\tau_z k_x \sigma_x + k_y \sigma_y) + M\sigma_z. \tag{2.3}$$

The band gap opening is described in Equation 2.3 with the last term and leads to a gap size of $2M$. Electrons close to K/K' behave in this situation as massive Dirac fermions.

2.1.2 Non-trivial topological properties of graphene

The Chern number of a 2D system classifies the topological nature of the occupied states [39] and can be obtained via [37]:

$$\begin{aligned} C &= \frac{1}{2\pi} \sum_n \int d^2k \Omega_n(\boldsymbol{k}) \\ \text{with } \Omega_n(\boldsymbol{k}) &= -\sum_{n' \neq n} \frac{2\text{Im}\langle u_n|v_x|u_{n'}\rangle\langle u_{n'}|v_y|u_n\rangle}{(\omega_{n'} - \omega_n)^2} \, . \end{aligned} \tag{2.4}$$

In Equation 2.4 Ω_n represents the z-component of the Berry curvature of the n-th valence band, $|u_n\rangle$ is its periodic Bloch function, and $v_{x(y)}$ is the velocity operator. Non-zero Chern systems are topologically non-trivial and become topological insulators in the case of an excitation gap at the Fermi level [39]. The band gap opening via a staggered sublattice potential, as described above, preserves the time-reversal symmetry. In the 2D hexagonal Brillouin zone this symmetry operation connects K and K' and requires further opposite Berry curvature and therefore opposite Chern numbers in each valley [37]. The total Chern number vanishes and eventually describes a topologically trivial material system [37]. A 2D layer of hexagonal boron nitride (h-BN) represents an example, where the two sublattices are made of two inequivalent chemical species. The Chern number also determines the number of chiral edge states due to the bulk boundary correspondence [39]. In the case of h-BN, though, none of those conducting edge states are present.

Haldane theoretically proposed another approach to obtain a gapped spectrum with a non-zero Chern number in graphene [40]. Here, an alternating periodic magnetic field perpendicularly penetrates the 2D hexagonal lattice and leaves a vanishing total magnetic flux. This leads to mass terms of opposite sign at K and K' and, thus, breaks the time-reversal symmetry [37]. The spinless Hamiltonian from Eq. 2.3 can be extended to [41]:

$$H(\boldsymbol{k}) = v(\tau_z k_x \sigma_x + k_y \sigma_y) + M\sigma_z + m\tau_z\sigma_z \, . \tag{2.5}$$

The last term in Equation 2.5 originates from the second-nearest-neighbor hopping between the two sublattices [37]. As the Chern numbers for both valleys are identical, the total Chern number is non-zero and describes a topologically non-trivial system [37]. A single edge mode on either side of the boundary emerges, which is characteristic for the quantum Hall effect (QHE) in a 2D system.

2.1.3 The Kane-Mele model

Both aforementioned approaches to induce a band gap in graphene break either the inversion symmetry (e.g., in h-BN) or the time-reversal symmetry (Haldane model). By considering now the spin-orbit coupling as a new mechanism that gaps the bulk spectrum at K/K' but respects

all symmetries present in graphene leads to the Kane-Mele model [11]. Here, the SOC is introduced as a second-nearest-neighbor hopping term between both sublattices, which yields a bulk Hamiltonian of [37]:

$$H(\boldsymbol{k}) = v(\tau_z k_x \sigma_x + k_y \sigma_y) + m\tau_z \sigma_z s_z \,. \tag{2.6}$$

The z-component of the spin-Pauli matrix is expressed as s_z in Equation 2.6. Pivotal in this model is the effective breaking of the time-reversal symmetry for each spin channel [37]. Therefore, the Kane-Mele model can be viewed as two copies of the Haldane model, in which spin-up and spin-down electrons have opposite mass terms [37]. Thus, the Chern numbers are integers but spin-dependent and eventually yield two counter-propagating and spin-polarized edge states [37]. Both are hallmark features of the QSHE [11]. The forbidden backscattering of electrons between the two edge modes in the presence of time-reversal symmetry is characteristic of a QSHE. In turn, this guarantees a dissipationless and quantized electron transport in the non-interacting case. The first experimental realization of the QSHE was performed in HgTe quantum wells and indeed yielded a quantized edge conductance of $G = \frac{2e^2}{h}$, where e is the electron charge and h the Planck constant [7].

Not only does breaking the time-reversal symmetry by a magnetic field destroy the quantum spin Hall phase. Kane and Mele also reported about the detrimental impact of the Rashba interaction and a staggered sublattice potential on the non-trivial properties [10]. The Rashba effect comes into play when the mirror symmetry is broken. For instance, placing graphene on a substrate surface could render it topologically trivial. However, as Kane and Mele found out both adverse impacts leave the quantum spin Hall phase intact until the Rashba interaction and/or staggered sublattice potential reach a specific value that exceeds the SOC strength [10]. In summary, the lattice symmetries of graphene in combination with SOC renders this materials system a QSHI.

2.2 Heavy group-IV elemental QSHIs

It is important to note the technological limitation of using the QSHE in graphene. The bulk band gap at K/K' of graphene is on the order of 1 µeV due to the second-order SOC term [12, 13]. Also, because SOC scales with the atomic number Z, the relatively light C atom introduces in general a weak SOC effect. Therefore, thermally activated electrons can easily overcome this small band gap and impede a sole quantized edge state transport, even at cryogenic temperatures [13]. In order to boost the SOC-driven band gap size of graphene one can replace the C atoms by high-Z elements. Graphene analogs from group-IV elements, like silicene (Si), germanene (Ge), and stanene (Sn), also form 2D hexagonal lattices with much larger non-trivial band gaps at the K points. For example, the band gap in stanene was theoretically predicted to be as large as 100 meV [15] (see Fig. 2.2b). A key characteristic of those 2D systems is the buckled hexagonal lattice as depicted in the side view of Figure 2.2a. The buckling of size δ originates in the larger interatomic distances found in these monolayers [14]. This reduces the p_z-overlap and,

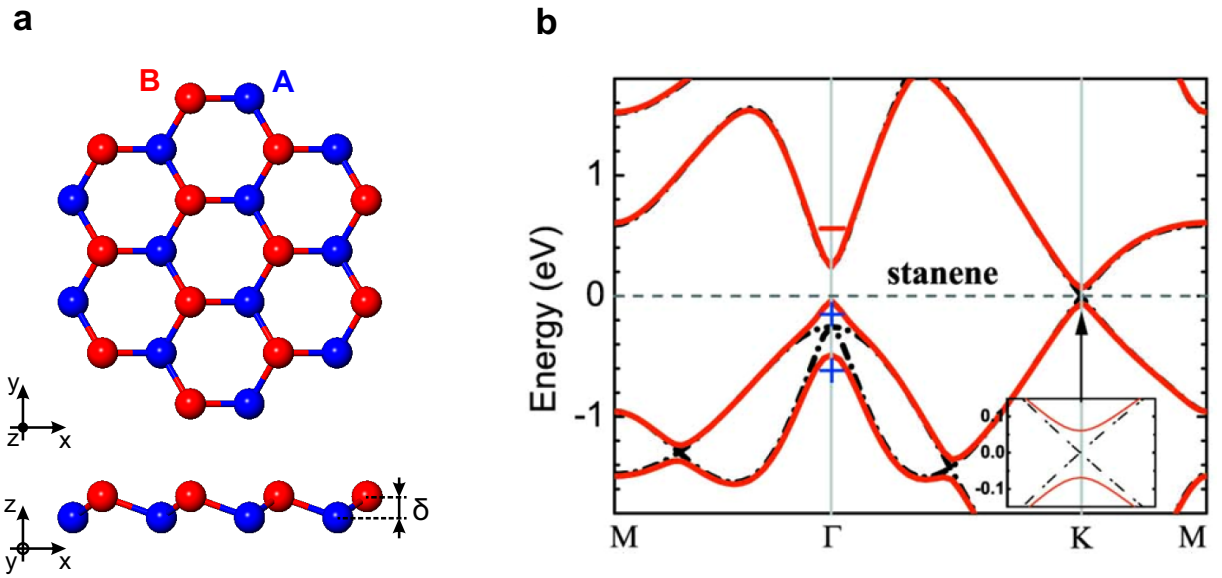

Figure 2.2: High-Z honeycomb structure with electronic properties of stanene – **a**, Lattice structure given in top and side view. High-Z graphene analogs exhibit a buckled structure with a height δ. **b**, Stanene exhibits a non-trivial band structure with a band gap of approximately 100 meV at K/K' after SOC is included (solid red line; black dash-dotted line without considering SOC). The + and − sign at Γ represent the parity of the Bloch wave functions. Figure in **b** was adapted with permission from Ref. [15]. Copyright © (2013) by the American Physical Society.

thus, weakens the resulting π-bonding, which is responsible for the flatness of the 2D layer [14]. Therefore, the atoms move closer together in the buckled structure, which in turn maintains a more stronger π-overlap. The resulting orbital hybridization deviates from pure sp^2 as in planar graphene and leads to sp^3-like hybridized orbitals [14]. The buckling also has a crucial impact on the spin-orbit interaction. Liu *et al.* derived a low-energy Hamiltonian for silicene with a strong first-order SOC term next to the minute second-order contribution [14]. All group-IV graphene analogs are therefore theoretically predicted to show the QSHE at much higher temperatures than in graphene, which could be potentially relevant for technological applications at and above room-temperature.

2.3 Decoupling of detrimental substrate interactions for group-IV QSHIs

A substrate is paramount when synthesizing such buckled hexagonal lattices. However, the mere presence of a substrate surface leads to a much stronger interaction of the adlayer atoms closest to the surface than the atoms farther away (cf. blue and red spheres in Fig. 2.2a, respectively) [27]. This staggered sublattice potential is, as described above, detrimental for the quantum spin Hall phase and can potentially destroy the non-trivial topological properties [10]. In this context, the topology of group-IV graphene analogs can be described as fragile or sensitive, which most likely originates from the exposed π-electrons forming the non-trivial low-energy spectrum.

The experimental realization of germanene on MoS_2 and stanene on Bi_2Te_3 yield for example a metallic ground state [21–23, 25]. Stanene was also realized on various metallic substrates, which however induce a large charge transfer and render the adlayer metallic as well [16–20]. Therefore, the realization of group-IV graphene analogs requires an insulating substrate that prevents short-circuiting of the non-trivial metallic edge state and thus preserves a sole quantized edge transport. Furthermore, the lattice parameters and symmetry must match the adlayer. In the case of stanene, the wide band gap material SiC meets all these requirements. Based on the in-plane lattice parameters of stanene ($a_{Stanene} = 4.68$ Å [9, 15]) and of the underlying SiC(0001) substrate ($a_{SiC} = 3.08$ Å [42]), a (2×2) stanene registry coincides with a (3×3) substrate surface periodicity [27]. However, the substrate surface could still destroy the topological properties of stanene due to its strong interaction.

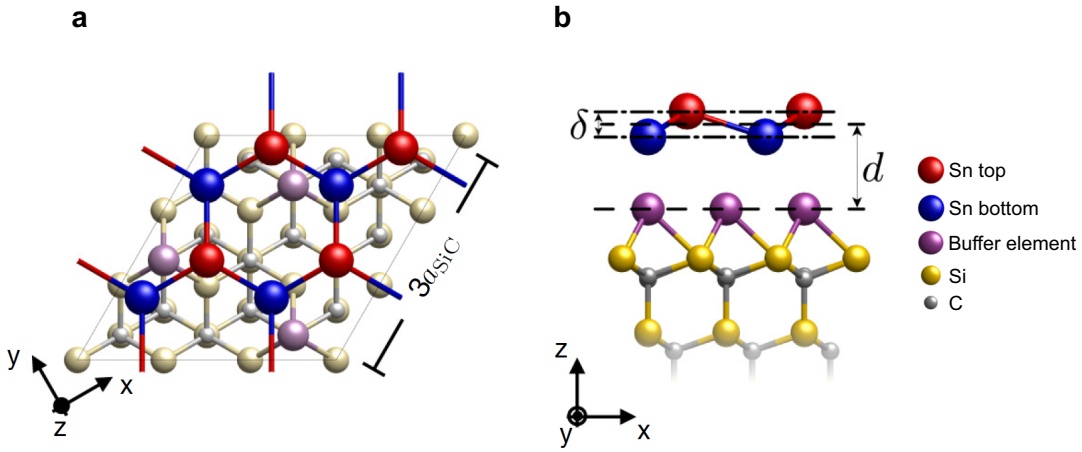

Figure 2.3: Stanene accommodated on buffer layer/SiC(0001) heterostructure – Structural model of stanene on top of buffer layer-SiC(0001) heterostructure in top-view (**a**) and side-view (**b**). **a**, The buffer layer elements form a triangular lattice with a $(\sqrt{3}\times\sqrt{3})$ periodicity and a coverage of 1/3 ML. A (2×2) periodicity of stanene is commensurable with a (3×3) SiC(0001) periodicity. **b**, The distance d between the stanene layer with buckling height δ and the substrate strongly influences the topological character. Figure in **a** and **b** were adapted with permission from Ref. [27]. Copyright © (2019) by the American Physical Society.

To diminish this substrate-adlayer interaction, Di Sante *et al.* proposed in a detailed density functional theory (DFT) study to use a *buffer layer* between the substrate and the stanene lattice on top, as depicted in Figure 2.3 [27]. The main purpose of the buffer layer is to passivate the unsaturated bonds on the substrate surface [26]. Group-III and -V elements such as Al, In, and Bi are arranged in a triangular $(\sqrt{3}\times\sqrt{3})$ lattice with a coverage of 1/3 ML to form the buffer layer (see Fig. 2.3a). Al and In are particularly well-known to passivate the structurally related Si(111) surface [28, 29] and are assumed to do so on Si-terminated SiC(0001) as well. The decisive part, however, is the strength of the ever-present potential acting on the stanene layer. In the DFT study, it became apparent that the antibonding state of the buffer layer made of Al and In, even in the structurally relaxed situation, still interacts inordinately with the bottom part of the buckled stanene lattice. The imposed staggered potential thus drives the entire system into the topologically trivial regime. The study also found indications of a detrimental covalent bonding

between this group-III buffer layer and stanene. According to Di Sante *et al.*, the quantum spin Hall insulating behavior of stanene persists only when group-V buffer layer elements on the C-terminated SiC surface are considered [27]. On this C-terminated surface, a buffer layer is generally bound more strongly and closely to the substrate than on the Si-terminated SiC surface due to the higher difference in electronegativity between the buffer layer element and substrate. This leads to a larger excitation gap for the group-V buffer layer and moves the antibonding state further away from the Fermi level, compared to its group-III buffer layer pendant. Thus, in this configuration, the stanene layer on top of the group-V buffer layer becomes quasi-freestanding with a relatively weak van der Waals-like coupling to the substrate.

As already suggested by Kane and Mele the staggered sublattice can leave the quantum spin Hall insulating phase intact (see Sec. 2.1.3). For instance, in a recently published theory study, it was shown that the non-trivial properties of strained stanene accommodated on Al_2O_3 survive, despite its interaction with the substrate [43]. However, upon reaching a critical strength the non-trivial state transitions to a trivial one accompanied by a band gap closure and a subsequent reopening of a trivial band gap [27]. This impact crucially depends on the distance d between the buffer and the stanene layer [27], as illustrated in the structural model in Fig. 2.3b.

It is important to note that the critical part of the presented theory from Di Sante *et al.* is the energetical position of the antibonding state of the buffer layer [27]. The DFT method that was employed tends to significantly underestimate this energy position, which could leave stanene accommodated on the Al and In buffer layer on the Si-terminated substrate surface in the non-trivial regime.

In conclusion, high-Z graphene analogs such as stanene are technologically promising QSHI candidates. Synthesizing these high-Z graphene analogs requires an insulating substrate that also matches the symmetry of the adlayer in order to take full advantage of all of their properties. In addition, the strong substrate-adlayer interaction needs to be reduced to preserve the topological nature, as theoretically derived for the case of stanene [27]. The SiC(0001) surface passivated with a buffer layer made of group-III and -V elements adsorbed in a $(\sqrt{3}\times\sqrt{3})$ lattice fulfills these requirements. Here, aluminum and indium turn out to be promising elements for the realization of this buffer layer, which will be investigated experimentally in the following work.

3 4H-SiC(0001) substrate

SiC(0001) is the preferential substrate material that meets all requirements to accomodate stanene, as outlined in the previous chapter. This chapter here is dedicated to highlighting the structural and electronic properties of SiC(0001) in more detail on the basis of Ref. [44]. In addition, the gas phase etching preparation of SiC prior the epitaxial growth process of the adlayers will be presented.

3.1 Structural and electronic properties

The term polytypism describes that a crystalline solid can occur in different lattice structures. Silicon carbide (SiC) is a prominent example because more than 200 different polytypes exist. Among the most studied polytypes are the 3C-, 4H-, and 6H-SiC crystals. The prefix denotes, firstly, the stacking sequence within the unit cell between different Si-C bilayers and, secondly, the type of crystal structure (C for cubic and H for hexagonal). The following elaboration on the structural and electronic properties is restricted to the 4H-SiC polytype.

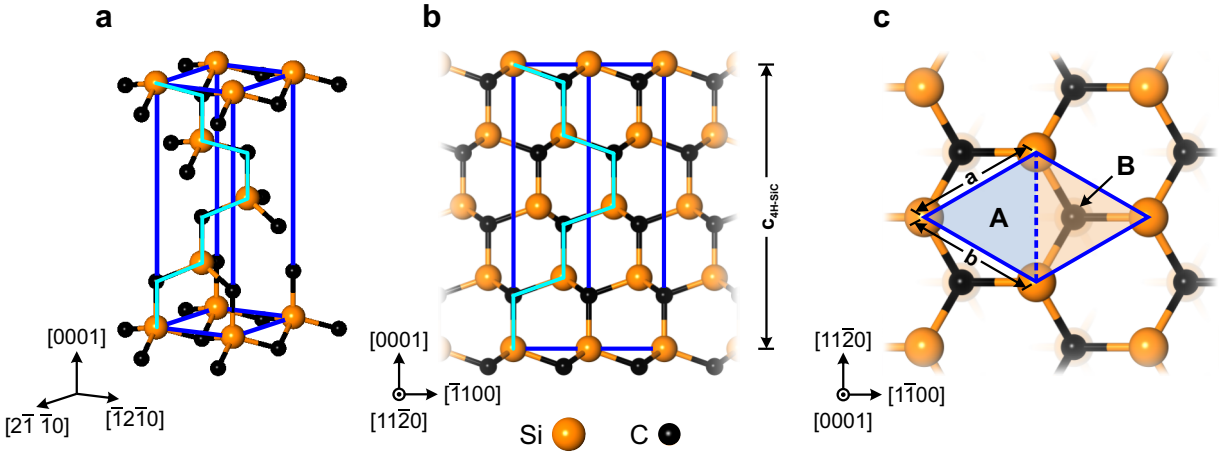

Figure 3.1: Lattice structure of the 4H-SiC(0001) substrate – The unit cell in a three-dimensional representation (**a**) and in the (11$\bar{2}$0) plane together with its lattice constant in c-direction c_{4H-SiC} (**b**). In **a** and **b** the fourfold stacking sequence in [0001]-direction is highlighted in cyan. **c**, Si-terminated (0001) surface unit cell with broken in-plane symmetry due to the underlying C atom depicted with two different triangles A and B. The in-plane lattice constants a and b are also shown. In all three panels the unit cell is highlighted in blue. The images of the crystal structure were generated with the *VESTA* software [45].

The crystal structure of 4H-SiC is illustrated from different perspectives in Figure 3.1. This lattice comprises of Si atoms coordinated tetrahedrally with C atoms and stacked with a fourfold

sequence along the [0001]-direction (marked in cyan in Fig. 3.1a, b) [46]. In this configuration the Si and C atoms are sp^3 hybridized. The height of a full unit cell amounts to $c_{4H-SiC} = 10.08\,\text{Å}$ and the in-plane periodicity is approximately $a = b = 3.08\,\text{Å}$ (see Fig. 3.1b, c) [42].

In this thesis, the Si-terminated (0001) surface plane was utilized. Due to a missing bonding partner in c-direction, an unsaturated bond per Si atom results. Electrons hopping from one site to another experience a strong Coulomb repulsion, which renders this (1×1) surface system a Mott-Hubbard insulator [47, 48]. As it will be discussed further below, a gas phase etching procedure passivates the surface with hydrogen and creates however an uncorrelated, common band insulator.

An important feature of the surface unit cell is the in-plane asymmetry depicted in Fig. 3.1c. The C atom of the uppermost bilayer renders both sides of the unit cell A and B structurally inequivalent. Thus, 2D lattices accommodated on this surface plane, in particular those following the (1×1) periodicity of the substrate, will experience the in-plane inversion symmetry breaking. This bears some intriguing consequences for the topology, as it will be presented later in Chapter 7 and 8.

The size of the band gap in 4H-SiC is 3.27 eV rendering it a wide band gap semiconductor [49]. Spectroscopic measurements, especially at low temperatures, require therefore a high doping level to prevent charging effects. Highly nitrogen-doped (n) 4H-SiC samples with a nominal specific resistance of $\rho = (0.01 - 0.03)\,\Omega\,\text{cm}$ were used throughout this work. The resistance translates to a sheet doping concentration of $n_{SiC} = (1.0 - 8.5) \cdot 10^{12}\,\text{cm}^{-2}$ at room temperature [44]. The samples were cut down in rectangular pieces with dimensions of $12\,\text{mm} \times 2.5\,\text{mm}$. Prior the epitaxy of buffer layer elements, the SiC(0001) samples were prepared in a gas-phase etching procedure based on hydrogen in order to create an atomically flat and well-ordered surface lattice.

3.2 Substrate preparation in flowing hydrogen atmosphere

In the following, this preparation approach will be presented based on a detailed STM and ARPES study published in Ref. [50]. Due to the wafer polishing the commercially purchased SiC wafer pieces usually exhibit deep scratches covered with a thick oxidation layer. This highly disordered surface is therefore unsuitable for any epitaxy. Since the Si-terminated SiC surface is in focus here, the use of wet-chemical treatments known to produce a smooth Si(111) surface can be considered. Hydrofluoric acid, for example, is widely used in the surface preparation of Si samples. After such treatment, the oxidation layer is effectively removed and leaves a hydrogen-terminated Si(111) surface behind [51–53]. Owed to the hardness and chemical inertness of SiC, those treatments lead however to insufficient results [50, 54, 55]. Only with a gas-phase hydrogen etching treatment an epitaxy-ready SiC(0001) surface down to the atomic scale is achievable [50, 56, 57].

Prior the gas-phase etching, the SiC wafer pieces used in this work were treated *ex situ* with acetone and isopropanol in an ultrasonic bath for about two minutes to remove a protective

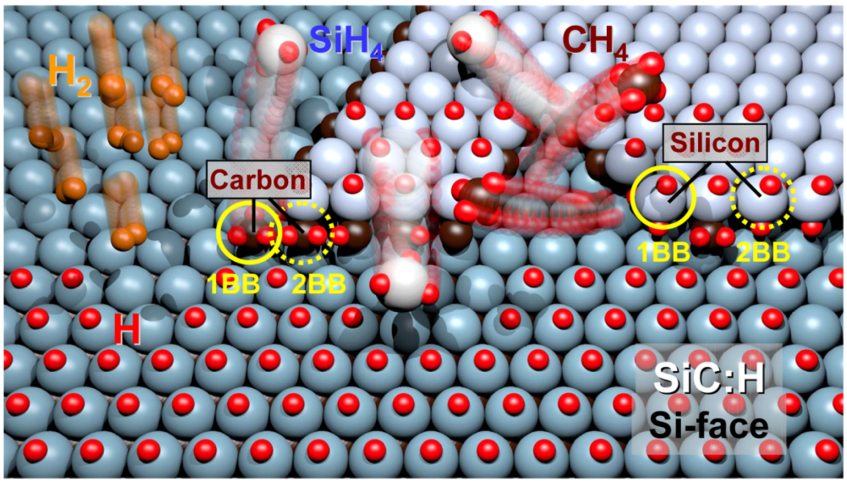

Figure 3.2: Atomistic view of the hydrogen etching process on SiC(0001) – Molecular hydrogen (brown) dissociates on the hot sample surface ($T \approx 1200 - 1300\,°C$) and subsequently binds to unsaturated bonds preferentially on step edges, where Si and C atoms are bound weaker to the SiC lattice compared to the 2D bulk. During hydrogenation, silane and methane are formed, which removes the SiC lattice in a layer-by-layer fashion. This eventually results in an atomically smooth and well-ordered SiC(0001) surface. Eventually, hydrogen atoms passivate the Si dangling bonds and render this surface chemically inert. Adapted with permission from Ref. [50]. Copyright © 2016, American Chemical Society.

coating. Subsequently, both edges of these pieces were roughened with a diamond tip in order to increase the surface area. This reduced the contact resistance after the sample was clamped into the sample carrier. Before that, however, loosely bound organic compounds and dust were removed by a treatment in ultrapure acetone, isopropanol, and methanol for two minutes each. Finally, the sample edges were wrapped with rhodium foil to further reduce the contact resistance before being clamped into the carrier.

Next, the sample was inserted into a dedicated ultra-high vacuum (UHV) etching chamber. A degas step around $900 - 950\,°C$ for about 1 h removed residuals and a larger part of the oxidation layer. The sample temperatures throughout this thesis were measured pyrometrically with an emissivity of $\epsilon = 85\%$. To minimize any oxygen contaminations, ultrapure hydrogen and helium (purity 7.0) from gas bottles were further filtered and introduced into the UHV chamber with a flow rate of 2 slm (standard liter per minute). In principle, the helium gas would dilute the hydrogen atmosphere and also would act as a carrier gas, which would remove the etching products faster from the chamber. In this hydrogen-helium atmosphere with a pressure of 950 mbar the sample was slowly ramped with direct current to a temperature of 1230 °C and kept constant for 2 min.

The etching process at the atomic scale is visualized in Figure 3.2. At such elevated temperatures the molecular hydrogen dissociates at the surface of the sample. Atomic hydrogen then binds preferentially to the dangling bonds of the exposed Si and C atoms at defects and step edges, where both elements are bound weaker to the SiC crystal. This hydrogenation eventually leads to the formation of silane (SiH_4) and methane (CH_4). Si and C are thus leaving the SiC lattice in the gas phase, which results in a layer-by-layer etching at the atomic scale. Since a high

sample temperature leads to a high etching rate, this first, coarse etching step described above removes the residual oxidation layer and large amounts of the deep scratches. However, silane is likely to redeposit and decompose on the surface due to its positive formation enthalpy compared to the thermodynamically more stable methane [58]. Therefore, this step was followed by a second, milder etching step at 1180 °C for 5 min. The result is an atomically flat and well-ordered SiC(0001) surface on large-scales as reported in Ref. [50]. As depicted in Fig. 3.2 the surface is passivated by hydrogen after the etching process. This chemically inert surface protects the substrate from oxidation and prevents any other covalent bonding to adsorbates [50, 56].

The samples used in this thesis were then transferred *in situ* with a UHV suitcase to the desired epitaxy or analysis UHV chamber in order to minimize detrimental adsorbates of any kind on the surface.

4 Experimental methods for surface analysis

This chapter presents the main experimental analysis methods utilized in this work to characterize the epitaxially grown Al and In films. LEED and STM were used to determine their lattice symmetry and structural parameters, which are discussed at the beginning. Subsequently, the STS and ARPES techniques are presented with which information about the electronic properties of the adlayers were obtained, followed by the X-ray photoelectron spectroscopy (XPS) method that was employed to determine the chemical composition and estimate the coverage of these films. The chapter ends with a brief presentation of the X-ray standing wave (XSW) method, which was utilized to resolve the bonding distance of an In-monolayer to the substrate. Adsorbate contamination layers on the surface would impede the applicability of these surface sensitive methods. Therefore, all methods presented here demand the use of a UHV environment.

4.1 Low-energy electron diffraction

After the discovery of diffracting electrons and their characterization on crystalline surfaces by Davisson and Germer in 1927 [59], the technique of low-energy electron diffraction evolved into a common surface characterization tool. The working principle is based on the interference of electron waves, i.e. quantum mechanically, the wave-particle duality of free electrons. Those electrons can be ascribed a wavelength of $\lambda = \frac{h}{\sqrt{2m_e E_{kin}}}$ where h, m_e, and E_{kin} are the Planck constant, the electron's free mass and kinetic energy, respectively. At typical electron energies in a LEED experiment (the range of approximately 50 eV to 100 eV was used in this thesis), the wavelength lies in the same order of magnitude as the lattice constants of solids (approximately 1 Å). This eventually allows for electron diffraction on the periodic atomic lattice.

Moreover, at these typical kinetic energies, electrons interact highly with solids, which can be described by an inelastic mean free path. The pronounced minimum at around 50 eV is generated by an inelastic scattering of the impinging electrons on plasmons (see Fig. 4.1a). This process limits the penetration depth of electrons into the material. Interestingly, the electron's inelastic mean free path follows for the vast majority of elements and material compounds roughly the same dependency described by the universal curve [60]. This is because the plasmon excitation depends on the electron density, which is roughly equal for all materials [61]. Therefore, using the aforementioned kinetic energies renders LEED a highly surface sensitive method, where the

diffraction mainly occurs in the uppermost surface layers of the solid. And vice versa, the information depth is strongly limited to the first few structural layers when excited electrons escape a material. This renders the photoelectron spectroscopy (PES) techniques in Sec. 4.3 also highly surface sensitive.

A conventional static LEED setup consists of an electron emitting filament (also called electron gun) and an electronic lens system to collimate and eventually accelerate the electrons onto the sample (see Fig. 4.1b) [62]. To eliminate unwanted deflections of their trajectory, the drift tube is, as well as the sample, on ground potential. After the diffraction the outgoing electrons pass several hemispherical grids, which mainly suppresses inelastically scattered electrons. Finally, the last grid accelerate the electrons onto a fluorescent screen where the diffraction pattern of the reciprocal surface lattice is displayed. The grids in between ensure a field-free space.

Constructive interference of elastically scattered electrons occurs only when the Laue condition is fulfilled:

$$\boldsymbol{K} = \boldsymbol{k}' - \boldsymbol{k}_0, \tag{4.1}$$

where $\boldsymbol{K}$ is a vector of the reciprocal lattice and $\boldsymbol{k}_0$ ($\boldsymbol{k}'$) is the incident (scattered) wave vector. When the wave vector changes by a reciprocal lattice vector during a scattering event it ultimately generates a diffraction spot. As LEED is highly surface sensitive the reciprocal space is restricted to the 2D surface lattice with the vector $\boldsymbol{K}$:

$$\boldsymbol{K} = h_1 \cdot \boldsymbol{a}_1^* + h_2 \cdot \boldsymbol{a}_2^*. \tag{4.2}$$

Here, both h_1 and h_2 are integers and $\boldsymbol{a}_1^*$ and $\boldsymbol{a}_2^*$ span the in-plane unit cell in reciprocal space. The relationship between the 2D real-space unit cell vectors ($\boldsymbol{a}_1$ and $\boldsymbol{a}_2$) and their respective reciprocal space counterpart is as follows:

$$\boldsymbol{a}_1^* = 2\pi \cdot \frac{\boldsymbol{a}_2 \times \boldsymbol{a}_3}{\boldsymbol{a}_1 \cdot (\boldsymbol{a}_2 \times \boldsymbol{a}_3)} \quad \text{and} \quad \boldsymbol{a}_2^* = 2\pi \cdot \frac{\boldsymbol{a}_3 \times \boldsymbol{a}_1}{\boldsymbol{a}_1 \cdot (\boldsymbol{a}_2 \times \boldsymbol{a}_3)}, \tag{4.3}$$

where $\boldsymbol{a}_3$ represents the unit cell lattice vector normal to the surface.

Another consequence of the surface sensitivity is the inability to probe the lattice periodicity perpendicular to the surface. This leads to infinitesimally small reciprocal lattice vectors or, in other words, so-called reciprocal lattice rods [63]. With the Ewald circle illustrated in Fig. 4.1c the resulting scattering vectors and, thereby, the diffraction pattern can be determined. Here, the incident wave vector $\boldsymbol{k}_0$ defines the radius of the circle. At every intersection of the circle with the lattice rods, the Laue condition is fulfilled.

Upon varying the electron kinetic energy the size of the circle changes which directly influences the scattered wave vectors (cf. Eq. 4.1) and results in moving diffraction spots on the fluorescent screen. The appearing diffraction pattern determines the surface periodicity and lattice symmetry in reciprocal space, which constitutes a qualitative study of the sample in LEED. A quantitative analysis on the size of a diffraction spot can further conclude the degree of the long-range lattice order and, for instance, gain information on the domain sizes [62, 64]. Defects, disorder, and

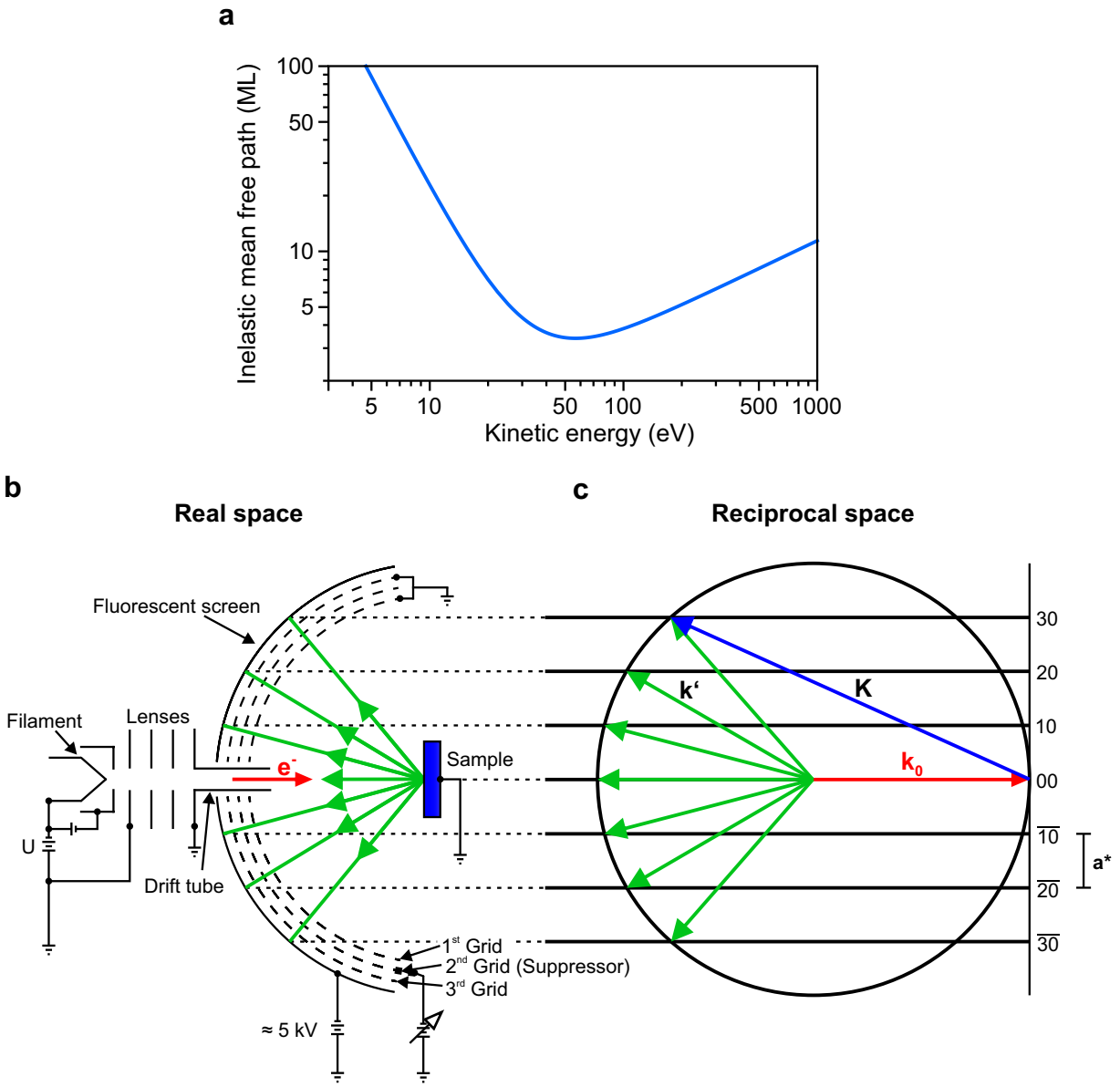

Figure 4.1: Universal curve and working principle of LEED – **a**, Inelastic mean free path λ of electrons in SiC as a function of their kinetic energy E. For this, the empirical function $\lambda = A/E^2 + B\sqrt{aE}$ with $A = 2170$, $B = 0.72$ and $a = 0.251\,\text{nm}$ (vertical spacing between Si-C bilayer in 4H-SiC) after [60] was used. Electrons scatter on the first layers of the material between 20 eV and 100 eV, rendering LEED a highly surface sensitive technique. This universal curve is also applicable to the PES methods discussed in Sec. 4.3. **b**, Conventional static LEED setup after [63] illustrating the working principle. **c**, Ewald circle (radius defined by the incident wave vector $\boldsymbol{k}_0$) intersecting reciprocal lattice rods and construct exemplary scattering wave vectors, which then appear as a diffraction image on the fluorescent screen.

other types of lattice imperfections give rise to incoherent electron scattering, which leads to a broadening of diffraction spots and an increase of the background intensity [64].

In summary, with a conventional LEED apparatus used in this thesis qualitative information on lattice symmetry and long-range atomic order of a sample surface were obtained.

4.2 Scanning tunneling microscopy and spectroscopy

Information on the corrugation and electronic properties at the atomic level is essential to get a full understanding of a surface lattice structure. Based on the pioneering work by Binnig and Rohrer in 1982 [65] STM and STS became prominent measurement techniques in the surface science community. This section introduces the principle behind STM/STS and presents the theoretical concept of the tunneling current based on Ref. [66].

4.2.1 Fundamental working principle

The central aspect of STM is positioning a sharp, metallic tip a few Ångstrom from the sample's surface, separated by a vacuum barrier. Applying a bias voltage between the tip and the sample promotes an electron current based on the quantum mechanical tunneling process. Accordingly, electrons have a finite probability to penetrate through the potential barrier and reach the tip or sample, depending on the polarity of the bias voltage. The transmission coefficient T for electrons with energy E tunneling through a 1D potential barrier of height $\Phi = \sqrt{V_0 - E}$ is proportional to:

$$T(E) \propto \exp\left(-2\kappa \cdot s\right) \text{ with } \kappa = \sqrt{\frac{2m\Phi}{\hbar^2}}\,, \tag{4.4}$$

where κ denotes the energy-dependent decay rate. The exponential dependency in T on the tip-sample-distance s is imprinted in the tunneling current and renders STM highly sensitive to surface corrugations, even at the atomic scale.

Such an experimental setup therefore requires proper damping of mechanical vibrations and shielding of electrical noises. Piezoelectric-driven actuators are used to position the tip with the demanding accuracy on all three axes. Figure 4.2 illustrates schematically the basic STM setup. By applying a voltage to these actuators, the in-plane position of the tip is controlled. This allows one to scan laterally over the sample surface with atomic precision. Furthermore, the sharp tip, which hosts ideally a single atom on its apex, probes only the surface area right underneath it and as a result, generates the high spatial resolution of STM.

Constant current operation mode

Topography data on the atomic scale can be obtained in STM with essentially two different modes of operation. In this work, the *constant current mode* was mainly used to characterize the Al and In surface reconstructions. The principle of this mode of operation can be described as follows. The STM tip is approached to the sample surface with a z-piezo actuator until a previously defined tunneling current I is reached. While the STM tip then scans over the sample surface, the recorded current is fed to a control unit, which maintains a constant current. This is achieved by applying a voltage to the z-piezo actuator, which leads to a vertical displacement of the tip. Thus, the piezo voltage signal constitutes a measure of the surface corrugation and results in topography maps at the atomic scale. However, not only the topography affects the

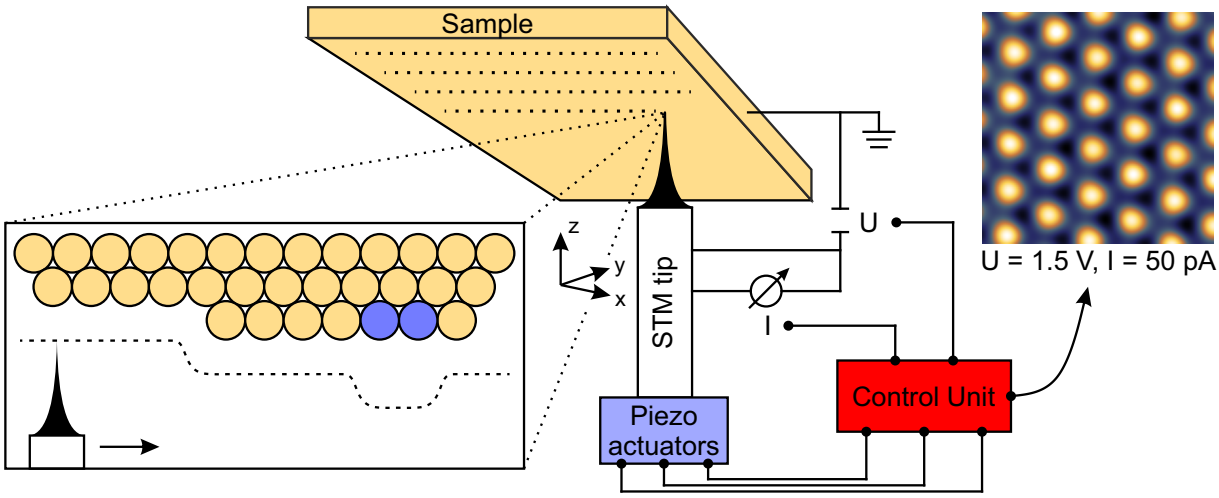

Figure 4.2: Schematic illustration of the working principle of STM – A sharp metallic STM tip is placed with piezoelectric actuators at an Ångstrom distance from the surface of a conducting sample. By applying a bias voltage U between the tip and sample promotes a tunneling current I. In the constant current mode (depicted on the left) the I signal is used to control the z-position of the tip via the control unit. The applied voltage to the z-piezo is then used as a height measure of the surface and yields a corrugation landscape on the atomic scale (illustrated on the right with a topography map of an In-monolayer on SiC). Both, the topography as well as the electronic properties (blue spheres) on the surface influences I and the resulting corrugation profile. Illustration after [65].

tunneling current. The local electronic properties of the surface also leads to a tip displacement. A contour map acquired in this operation mode represents therefore more a constant current map and needs to be analyzed with great care. The theoretical description of the tunneling current presented in Sec. 4.2.2 addresses this characteristic relationship.

Constant height operation mode

The other method to obtain surface topography information is based on the *constant height mode* of STM. In this case, the tip is positioned and scanned over the surface at a predefined z-position. The surface corrugation determines the tip-sample distance and thus the modulation of the tunneling current. Topography information is then reflected in the recorded tunneling signal. A major drawback of this technique however is that it can only be applied to flat surfaces, where the corrugation amplitude is smaller than the configured tip-sample distance. This method is therefore mainly applied to small areas that were scanned previously with the constant current mode. In order to resolve a charge accumulation in real-space within a single unit cell of indenene, the constant height mode in combination with STS was used in this thesis.

4.2.2 Theoretical concept of the tunneling current

The tunneling current I can be derived from perturbation theory as:

$$I = \frac{2\pi e}{\hbar} \sum_{\mu,\nu} \Big\{ f(E_\mu)[1 - f(E_\nu + eU)] - f(E_\nu + eU)[1 - f(E_\mu)] \Big\} \cdot |M_{\mu\nu}|^2 \delta(E_\nu - E_\mu)\,, \qquad (4.5)$$

where $f(E)$, $M_{\mu\nu}$, and $\delta(E_\nu - E_\mu)$ denote the Fermi-Dirac function, the tunneling matrix element between unperturbed tip Ψ_μ and sample surface states Ψ_ν, and the delta function ensuring an elastic tunneling process, respectively. The two different parts in the curly brackets describe a tunneling process from occupied states of the tip to unoccupied states in the sample and vice versa. The tunneling matrix element is central for the tunneling current, as can be seen in Eq. 4.5. It is defined as:

$$M_{\mu\nu} = \frac{-\hbar^2}{2m} \int \left(\Psi_\mu^* \boldsymbol{\nabla} \Psi_\nu - \Psi_\nu \boldsymbol{\nabla} \Psi_\mu^* \right) d\boldsymbol{S} \,, \tag{4.6}$$

and requires knowledge about both states. In general, however, the wave function of the tip and sample surface are unknown. Tersoff and Hamann assumed a local spherical symmetry of radius R for the tip apex centered around $\boldsymbol{r}_0$, i.e., an s orbital-like wave function [67, 68]. In the low temperature as well as low tunneling voltage regime ($eU \ll E_F$), the tunneling current from Equation 4.5 can be expressed as:

$$I \propto U \cdot n_t(E_F) \cdot \exp\left(2\kappa R\right) \cdot \underbrace{\sum_\nu |\Psi_\nu(\boldsymbol{r}_0)|^2 \cdot \delta(E_\nu - E_F)}_{n_s(E_F, \boldsymbol{r}_0)} \,, \tag{4.7}$$

where the $n_t(E_F)$ and κ describe the density of states (DOS) of the tip at the Fermi energy and the decay rate of the tunneling current through a barrier of height Φ (cf. Eq. 4.4), respectively. The last part of Equation 4.7, $n_s(E_F, \boldsymbol{r}_0)$, represents the local density of states (LDOS) of the sample surface at the Fermi level. Hence, the local electronic structure of the sample surface also contributes to STM contours, as illustrated exemplarily for the constant current mode in Fig. 4.2. It is important to note that this mathematical expression is only valid in the low bias regime.

Throughout this work, SiC(0001) with a band gap of approximately 3.3 eV [49] was used as a substrate, which requires, however, high tunneling biases in STM. At such voltages, both the tip and sample wave functions are heavily distorted along with their respective energy states. In a first order approximation the finite bias voltages can be taken into account with a rigid energy shift of the sample LDOS by eU relative to the tip. Additionally, the tip and sample wave functions Ψ_μ and Ψ_ν, respectively, are assumed to be not perturbed. As a result, the expression for the tunneling current derived in Equation 4.7 transforms to:

$$I \propto \int_0^{eU} n_t(\pm eU \pm \epsilon) \cdot n_s(\epsilon, \boldsymbol{r}_0) d\epsilon \,, \tag{4.8}$$

where all energies ϵ are given with respect to the Fermi level. As can be seen in Equation 4.8 all states between the Fermi level and the applied bias voltage contribute to the tunneling current. Assuming the local spherical symmetry of the tip apex and applying a WKB-type approximation

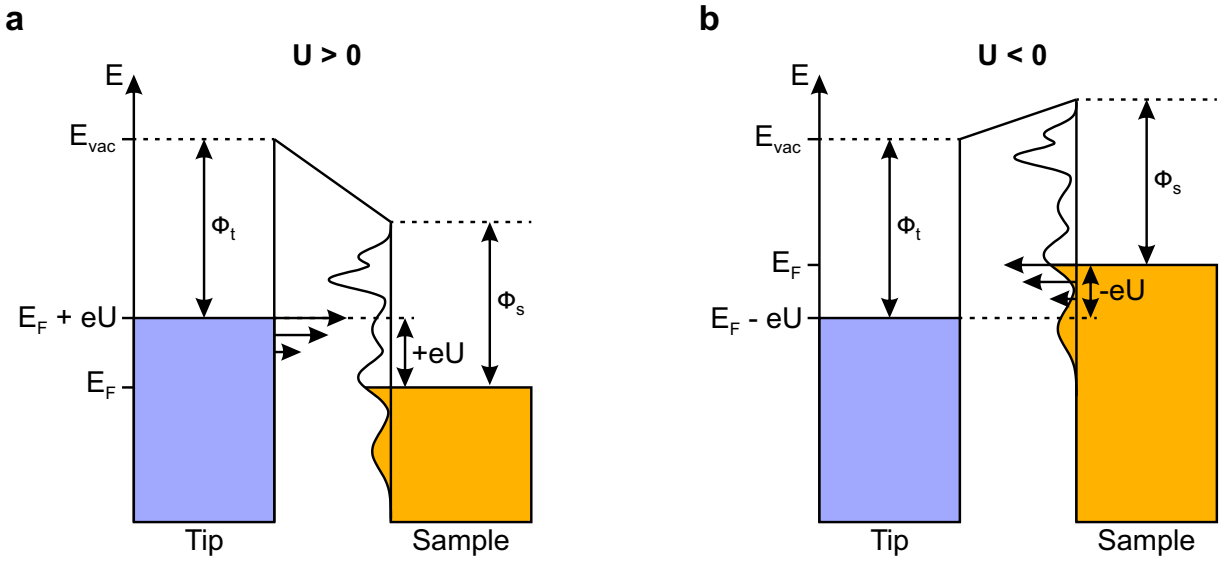

Figure 4.3: Tunneling process at different bias voltages – **a**, Schematic illustration of electrons tunneling from occupied states of the tip to unoccupied states of the sample surface after applying a positive tunneling voltage ($U > 0$). **b**, A sign change in the bias voltage ($U < 0$) reverses the tunneling process described in **a**. The length of the arrows represent the electron's transmission probability, which is highest for electrons at the highest occupied energy level but decreases towards lower energies. The work function of the tip and sample is denoted as ϕ_t and ϕ_s, respectively. Illustration after [69].

to the tunneling barrier, leads to a new expression of the tunneling current:

$$I \propto \int_0^{eU} n_t(\pm eU \mp \epsilon) \cdot n_s(\epsilon) \cdot T(\epsilon, eU) d\epsilon \,, \tag{4.9}$$

with an energy and bias-dependent transmission coefficient $T(\epsilon, eU)$:

$$T(\epsilon, eU) = \exp\left(-2(s+R)\sqrt{\frac{2m}{\hbar^2}\left(\frac{\phi_t + \phi_s}{2} + \frac{eU}{2} - \epsilon\right)}\right). \tag{4.10}$$

This coefficient determines the exponential decay of I with increasing tunneling barrier thickness and has a similar form as Equation 4.4. Electrons occupying the highest possible energy level therefore have the highest transmission probability and contribute the most to the tunneling current, whereas the probability decreases towards lower energies. This relation is schematically illustrated with black arrows in Fig. 4.3. Applying a positive bias voltage ($U > 0$) promotes electrons to tunnel from occupied states of the tip to unoccupied states of the sample (see Fig. 4.3a). In this case, the unoccupied part of the sample LDOS is probed. Reversing the bias voltage ($U < 0$) allows the occupied sample LDOS to be examined (see Fig. 4.3b).

The decay rate κ presented in Eqs. 4.4, 4.7, and 4.10 also depends on details of the electrodes' band structure involved in the tunneling process. Since elastic tunneling is assumed, the in-plane momentum of the electron is conserved, which can be approximated as follows: $\kappa^2 \propto k_\parallel^2$. This means that the strongest contribution to I comes from electrons located near the center of the 2D Brillouin zone Γ. In contrast, electrons with large in-plane momentum $k_\parallel$, for example at

the boundary of the Brillouin zone, have a smaller contribution to I. This comes into play when the Dirac-like states at K/K' of indenene are probed (see Chap. 8).

The s-orbital character of the tip wave function in the Tersoff-Hamann approximation intends to give only a rough estimation of the tunneling current. In this work, for instance, an angular dependence of the tip wave function can be expected since a tungsten tip with primarily d states at the Fermi level was used [66, 70]. However, this does not fundamentally change the tunneling process derived from the Tersoff-Hamann theory.

In this thesis, prior STM or STS related measurements, the tip was examined and conditioned on a clean Ag(111) reference crystal. The distances and height values obtained from STM scans were taken from corrugation profiles. The measurement uncertainties are primarily based on the calibration of the STM stage and the accuracy of reading. To cover all of these contributions an uncertainty of 3% was estimated.

4.2.3 Scanning tunneling spectroscopy

In general, the topography as well as the electronic structure of the sample contribute to the tunneling current in STM, as derived in the previous section. In order to extract the LDOS information of the sample, Equation 4.9 needs to be differentiated yielding the expression:

$$\frac{\mathrm{d}I}{\mathrm{d}U}(U) \propto en_t(0) \cdot n_s(eU) \cdot T(eU, eU) + \int_0^{eU} n_t(\pm eU \mp \epsilon) \cdot n_s(\epsilon) \cdot \frac{\mathrm{d}T(\epsilon, eU)}{\mathrm{d}U} d\epsilon \,. \tag{4.11}$$

Because the energy-dependent variation of the transmission coefficient is low at a fixed position, the latter term can usually be neglected. Additionally, with the assumption of a constant DOS of the tip, the detected differential conductivity $\mathrm{d}I/\mathrm{d}U$ gives a measure of the sample LDOS:

$$\frac{\mathrm{d}I}{\mathrm{d}U}(U) \propto n_s(eU) \,. \tag{4.12}$$

Experimentally, there are two different approaches to measure the LDOS of the sample, which will be presented in the following.

Current imaging tunneling spectroscopy (CITS)

In this method, the bias voltage is ramped in a predefined interval while the tunneling current is recorded at a fixed position, yielding a $I(U)$ curve. Preset tunneling setpoint parameters (I_{set} and U_{set}) stabilize the tip-sample distance, when the feedback loop is switched off during data acquisition. The LDOS is then obtained via a numerical differentiation of the $I(U)$ curve. By repeating this procedure on a virtual, predefined grid, all spectroscopic information is acquired where the electronic properties of the sample are resolved spatially and energetically. In general however the experimental noise level in a single $I(U)$ curve can be fairly high to extract adequate information on the LDOS by differentiation. Therefore, the noise contribution can be reduced by averaging over many curves.

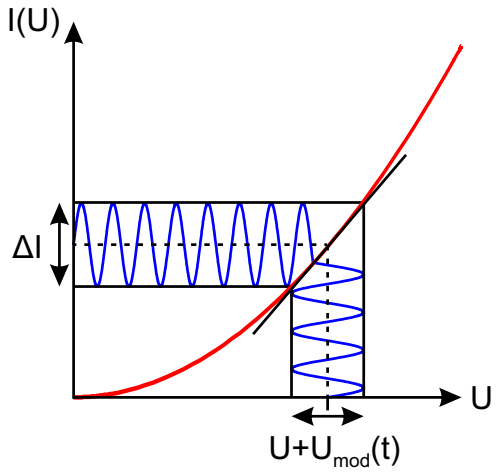

Figure 4.4: STS signal from lock-in amplifier – On top of the constant bias voltage U the lock-in amplifier modulates a sinusoidal signal $U_{mod}(t)$, which leads to the modulation of the tunneling current ΔI, which is proportional to the slope of the $I(U)$ curve (black line as tangent). With $\Delta I \propto \mathrm{d}I/\mathrm{d}U$ (cf. Equation 4.13) a direct measure of the sample's LDOS is obtained.

STS with a lock-in amplifier

The derivative can also be obtained directly from the experiment by using a lock-in amplifier. The constant tunneling bias voltage is modulated here with a small sinusoidal voltage of $U_{mod}(t) = U_{mod} \cdot \sin(\omega t)$, as schematically depicted in Figure 4.4. The frequency ω is chosen to be far from the cutoff frequency of the feedback loop to ensure a constant distance between the tip and sample. In addition, the frequency should be outside typical electrical noise frequencies (e.g., 50 Hz) and their higher orders. The first-order Taylor expansion around the bias voltage reveals:

$$I(U(t)) = I(U + U_{mod} \cdot \sin(\omega t)) \approx I(U) + \underbrace{\frac{\mathrm{d}I(U)}{\mathrm{d}U} \cdot U_{mod}}_{\Delta I} \cdot \cos(\omega t)\,, \tag{4.13}$$

of which the lock-in amplifier detects only the periodic response of the system with frequency ω, i.e., the differential conductivity in the ΔI term (cf. black tangent in Fig. 4.4). Thus, this method obtains the LDOS information of the sample directly from experiment. Due to using a lock-in amplifier, disturbing noise frequencies are filtered out. However, applying a modulation voltage decreases the energy resolution of the spectroscopic method in addition to the thermal broadening at finite temperatures of the sample.

All spectroscopy data presented in this work were acquired at approximately 4 K. At that temperature, the energy broadening is dominated by the contribution from the modulation voltage, which was in the most cases set to $eU_{mod,rms} = 10$ meV. For the In high coverage phases presented in Chapter 6 grid measurements together with a lock-in amplifier were used. The single $\mathrm{d}I/\mathrm{d}U$ curves were obtained by numerical differentiation.

LDOS mapping

Depending on the experiment, both the constant-current and constant-height LDOS maps are obtained simultaneously with the topography STM scan. The fixed energy, however, prevent the detection of the entire spectroscopic information over an energy interval, which is the main disadvantage of this approach. Despite this disadvantage, the high spatial resolution set by the STM scan is directly translated to the LDOS map. In contrast to the LDOS maps here, the tunneling setpoints in the spatially resolved CITS measurements dictate a constant tip-sample distance for the entire probed energy window. In Chapter 8 LDOS maps of a triangular In unit cell at different energies were obtained with the utilization of the lock-in technique discussed here. Identical setpoint parameters for all probed energy windows were used to make the tip-sample distances comparable.

4.3 Photoelectron spectroscopy

In general, PES allows information on the occupied electronic structure of materials to be obtained. With XPS for example, a subtype of PES, the material's chemical composition can be identified, whereas ARPES reveals the electronic band structure in reciprocal space. In this section, an overview of the basic work principle of the photoemission process is given, followed by a theoretical description of the three-step model on the basis of Refs. [61, 71]. Building on this, a brief introduction on estimating the adlayer coverage with XPS and determining the substrate-overlayer bonding distance with XSW will be provided.

4.3.1 Basic work principle

Historically, a photo-induced emission of electric charges from a solid was first discovered by H. Hertz [72] in 1887 and later theoretically described by A. Einstein in 1905 [73]. The key mechanism is based on electrons absorbing the energy and momentum[1] of incoming photons with energy $E_{ph} = \hbar\omega$. Free electrons are only generated when the photon energy exceeds both the binding energy of the electron E_b in its initial state and the work function of the material Φ, i.e., the difference between the vacuum E_{vac} and the Fermi level E_F. This relation defines the kinetic energy E_{kin} of emitted photoelectrons:

$$E_{kin} = \hbar\omega - \Phi - |E_b|\,, \tag{4.14}$$

which is usually measured by an energy analyzer as a function of kinetic energy and is illustrated in Figure 4.5a. Thus, the measured photoemission spectrum corresponds directly to the electronic

[1] In photoemission experiments with low-energy photons, e.g. at 21.2 eV, the photon momentum is negligibly small. It becomes however relevant in the high photon energy regime. For example, at $E_{ph} = 6\,\text{keV}$ the photon momentum is approximately $3\,\text{Å}^{-1}$, which covers a wide range of the Brillouin zone from common crystalline materials.

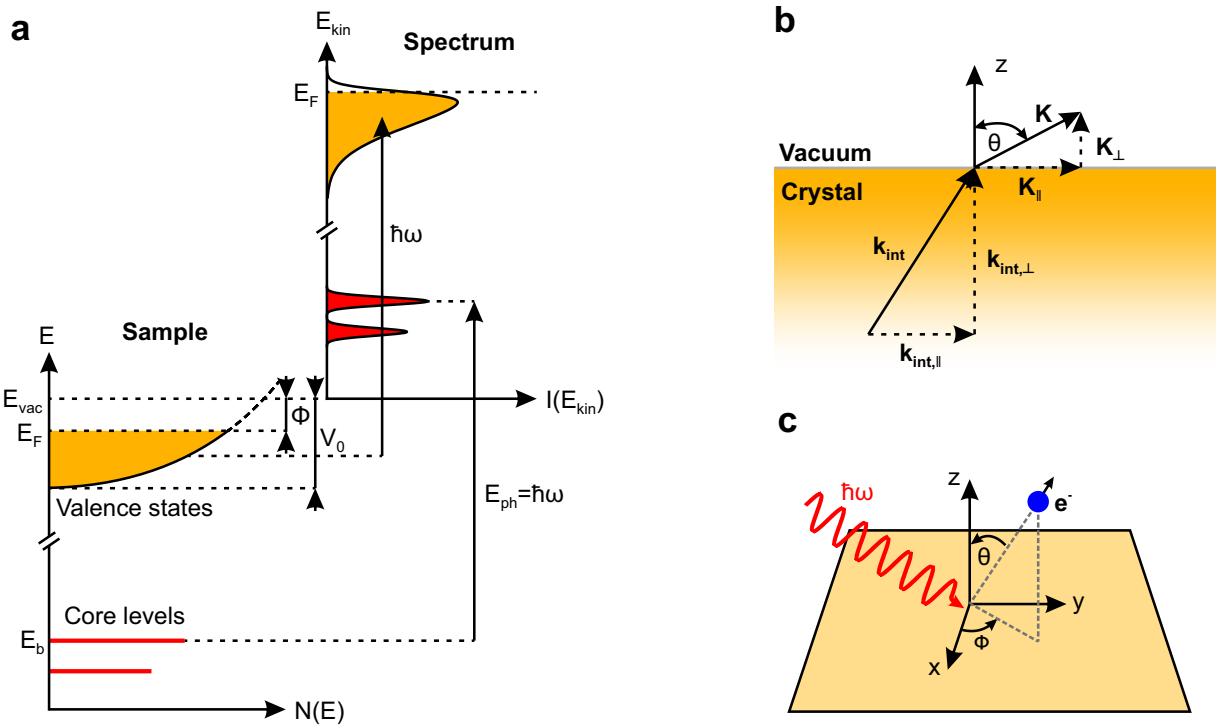

Figure 4.5: Schematic illustrations of the photoemission process – **a**, Energy relation between valence and core-level electrons with binding energy E_b in a solid and the spectrum of photo-emitted electrons measured by an energy analyzer. $N(E)$ represents the DOS and Φ and V_0 denote the work function and inner potential, respectively. **b**, Momentum relation of photoelectrons emitted at an angle of θ with respect to the surface normal at the crystal-vacuum interface. The perpendicular momentum component of the internal electron is not conserved in the photoemission process, i.e., $\mathbf{k}_{int,\perp} \neq \mathbf{K}_\perp$. **c**, Emission angles θ and ϕ together with the kinetic energy of a photoelectron define the parameter spectrum necessary to obtain a full band structure with a hemispherical analyzer (see Equation 4.18). Illustrations in **a** and **b** after [61, 71]. Schematic in **c** after [71].

structure of the sample. Depending on the photon energy, electrons from core-levels and/or valence states leave the solid and can be studied spectroscopically. A finite lifetime of the created core-hole and a restricted instrumental energy resolution lead to a Lorentzian and Gaussian broadening of the detected spectrum, respectively. Valence states of metallic samples are further cut-off at the Fermi level by the Fermi-Dirac function, whose width is defined by the sample temperature.

4.3.2 Three-step photoemission model

A simplified overview of the photoemission process is provided by the *three-step model*:

1. Electron excitation from the initial to the final state after absorption of a photon.
2. Excited electron travels through the solid towards the surface.
3. Escape of the photoelectron into the vacuum and subsequent detection.

First step – The sudden approximation is a central aspect of the photon-induced high-energy excitation. The instantaneous creation of a photohole inhibits the interaction of the photoelectron

with the remaining system. Hence, a small perturbation Δ induced by the electromagnetic field generate a transition from the initial Ψ_i to the final state Ψ_f. The transition rate w can then be described within Fermi's Golden Rule as:

$$w \propto \frac{2\pi}{\hbar} |\langle \Psi_f | \Delta | \Psi_i \rangle|^2 \delta(E_f - E_i - \hbar\omega) \,, \tag{4.15}$$

where the delta function ensures the energy conservation during the photoemission process. The final photoelectron current is proportional to w. With the vector potential of the photon field $\boldsymbol{A}$ and the momentum operator $\boldsymbol{p} = i\hbar\boldsymbol{\nabla}$ the perturbation induced by the electromagnetic wave turns into $\Delta = \frac{e}{mc}\boldsymbol{A} \cdot \boldsymbol{p}$. Here, two-photon processes were neglected, which are usually irrelevant when low-intense standard light sources in laboratories are used [74]. Surface photoemission effects were also disregarded [74]. In the vacuum ultraviolet (VUV) range the dipole approximation can be further applied, where the electromagnetic field is treated as a constant. In this regime, the photon wavelength is significantly larger than the interatomic distances in solids. It is important to note that at higher photon energies this dipole approximation does not hold anymore.

So far, no approximation of the considered wave functions for the initial and final states were made. The simplest picture provides the one-electron view where an interacting many-body system is disregarded. The detected photoemission intensity, defined by Fermi's Golden Rule in Eq. 4.15, is then directly proportional to the DOS of the sample. In strongly correlated systems however a more complex picture emerges. Depending on the strength of this interaction, satellite lines can emerge next to their main line in core-level spectroscopy [61]. ARPES can reveal for example distinct kinks in the band dispersion close to the Fermi level as a signature of materials with a strong electron-phonon coupling [75]. The thin Al and In films presented in this thesis were not investigated with regard to correlation effects.

Second step – After its creation, the photoelectron travels to the surface of the solid. The main inelastic scattering mechanism of those electrons is based on electron-electron interactions. This defines the information depth obtained by photoemission and is depicted as the inelastic mean free path in Figure 4.1a. The photon energies of 1486.6 eV (Al-K_α line) and 21.2 eV (He-I radiation) used for the XPS and ARPES experiments in this thesis, respectively, reveal a highly surface sensitive technique. In particular, ARPES probes only the first few monolayers of the sample.

Third step – The photoelectron then escapes the solid crystal and transitions into the vacuum. Only electrons with a sufficiently high kinetic energy are able to overcome the surface potential barrier or inner potential, V_0 (see Fig. 4.5a) [71]. All other electrons are reflected back into the bulk. Due to the translational symmetry at the surface this transition process conserves the in-plane electron momentum. Considering now a parabolic dispersion of the final state therefore leads to [71]:

$$|\boldsymbol{k}_{int,\parallel}| = |\boldsymbol{K}_\parallel| = |\boldsymbol{k}_\parallel| = \frac{\sqrt{2mE_{kin}}}{\hbar} \cdot \sin\theta \,, \tag{4.16}$$

which connects the internal and external in-plane components via the emission angle of the photoelectron θ (see Fig. 4.5b). The potential gradient created by a surface leaves the perpendicular momentum component $\boldsymbol{k}_{int,\perp}$ not conserved in this process ($\boldsymbol{k}_{int,\perp} \neq \boldsymbol{K}_{\perp}$) and yields [71]:

$$|\boldsymbol{k}_{int,\perp}| = \frac{\sqrt{2m(E_{kin} \cdot \cos^2\theta + V_0)}}{\hbar}\,. \tag{4.17}$$

A hemispherical analyzer with a 2D detector is then able to measure the electronic band structure dispersion $I(E_{kin}, K_x, K_y, K_z)$ based on the kinetic energy and the emission angles of the photoelectron (see Fig. 4.5c). The separate momentum components are [71]:

$$\begin{aligned} K_x &= \frac{\sqrt{2mE_{kin}}}{\hbar} \cdot \sin\theta\cos\phi \\ K_y &= \frac{\sqrt{2mE_{kin}}}{\hbar} \cdot \sin\theta\sin\phi \\ K_z &= \frac{\sqrt{2mE_{kin}}}{\hbar} \cdot \cos\theta\,. \end{aligned} \tag{4.18}$$

4.3.3 Film coverage estimation with XPS

The total integrated intensity of a photoemission line $I_{i,X}$ of core-level i and element X is given by [61, 76]:

$$I_{i,X} = K \cdot T(E_{i,X}) \cdot L_{i,X}(\gamma, \hbar\omega) \cdot \sigma_{i,X}(\hbar\omega, E_{i,X}) \cdot n_X \cdot \lambda(E_{i,X}) \cdot \cos\theta\,, \tag{4.19}$$

where K is an instrumental constant, $T(E_{i,X})$ the transmission function of the analyzer as a function of kinetic energy of the photoelectrons $E_{i,X}$, and $\sigma_{i,X}(\hbar\omega, E_{i,X})$ the total photoabsorption cross section of the core-level i, respectively. The latter strongly depends on the utilized photon wavelength and generally decreases with increasing photon energy [77]. In addition, this parameter was calculated by applying a Hartree-Fock-Slater one-electron central potential model to free isolated atoms [77]. The angular asymmetry factor $L_{i,X}(\gamma)$ in Equation 4.19 is derived to be [61, 77, 78]:

$$L_{i,X}(\gamma, \hbar\omega) = 1 + \frac{\beta_{i,X}(\hbar\omega)}{4} \cdot (1 - 3\cos^2\gamma)\,, \tag{4.20}$$

where γ is the angle between the incident photon and escaping photoelectron trajectory. The last three parameters are the density of the element n_X, the inelastic mean free path for photoelectrons as a function of kinetic energy $\lambda(E_{i,X})$, and the escape angle of the photoelectrons from the solid θ with respect to the surface normal (cf. Fig. 4.5b, c).

Figure 4.6 illustrates the scenario of a uniformly covered substrate of material B with an overlayer of material A and thickness d. Due to this overlayer, the photoemission signal from the substrate is damped according to Beer's law. In order to estimate the density of the film from XPS, and later the film thickness d, the intensity ratio of the detected photoelectrons from both materials I_A/I_B needs to be considered. This cancels the instrumental constant K from

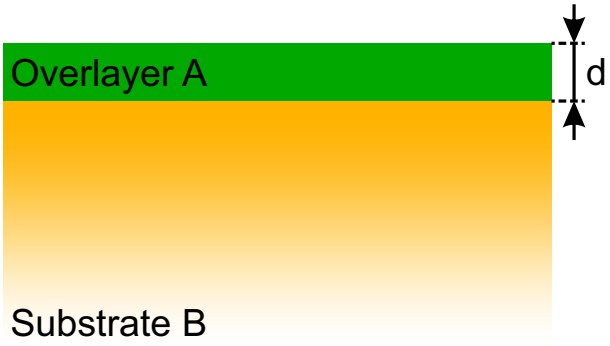

Figure 4.6: Assumed heterostructure to estimate the XPS coverage – A schematic illustration of an overlayer of material A completely covering a substrate of material B. The overlayer has a uniform thickness d.

Equation 4.19. According to Ref. [79], the ratio is derived as follows:

$$\frac{I_A}{I_B} = \frac{I_{A,\infty} \cdot [1 - \exp(-d/\lambda_A(E_A)\cos\theta)]}{I_{B,\infty} \cdot \exp(-d/\lambda_A(E_B)\cos\theta)} \,. \tag{4.21}$$

The numerator and denominator represent the photoemission intensity of the overlayer A and substrate B, respectively. Photoelectrons of kinetic energy E_B from the substrate B scatter inelastically in the overlayer A, which is described by the inelastic mean free path $\lambda_A(E_B)$. In addition, photoelectrons from the overlayer itself scatter inelastically, which yields $\lambda_A(E_A)$. Inserting the prefactors from Eqs. 4.19 and 4.20 into Eq. 4.21 yields the following:

$$\frac{I_A}{I_B} = \frac{n_A \cdot T(E_A) \cdot \sigma_A(\hbar\omega, E_A) \cdot \lambda_A(E_A)}{n_B \cdot T(E_B) \cdot \sigma_B(\hbar\omega, E_B) \cdot \lambda_B(E_B)} \cdot \tilde{L}_{A,B}(\hbar\omega) \cdot \frac{[1 - \exp(-d/\lambda_A(E_A))]}{\exp(-d/\lambda_A(E_B)} \tag{4.22}$$

with:

$$\tilde{L}_{A,B}(\hbar\omega) = \frac{1 - \frac{\beta_A(\hbar\omega)}{4} \cdot (3\cos^2\gamma - 1)}{1 - \frac{\beta_B(\hbar\omega)}{4} \cdot (3\cos^2\gamma - 1)}. \tag{4.23}$$

For $\gamma \approx 54°$, the angular asymmetry factor $\tilde{L}_{A,B}(\hbar\omega)$ in Eq. 4.23 reaches unity irrespective of the element studied. The 2D atomic density of the overlayer and substrate (n_A, n_B) can be calculated from the crystal structure of the respective bulk material. Solving Equation 4.22 for d yields the thickness of the overlayer. The coverage Θ_{ML} of the element A on substrate of material B can then be calculated from $\Theta_{ML} = d/l$, where l denotes the bulk layer spacing of material A. In general however both values should be treated with great caution as many assumptions were taken. For instance, the cross section parameters were derived in a Hartree-Fock-Slater model in the non-interacting ground state electron configuration for isolated atoms [77]. Additionally, a homogeneously covered substrate surface was assumed. All of these assumptions make the analysis easier but are not necessarily applicable to the specific problem in the experiment. Thus, an error bar of up to 30% is not uncommon in determining the coverage with XPS [61]. However, the resulting thickness and coverage values obtained with the equations above still gives an estimation and places the overlayer, for example, in the high or low coverage regime.

With the XPS analysis approach derived here, the coverage of Al and In films on SiC(0001) were characterized in this thesis.

The technical details of the photoemission setup with which the XPS and ARPES measurements were conducted and presented in this thesis are described in the following. For both techniques, a hemispherical analyzer from *Specs* (PHOIBOS 100) and a 6-axis manipulator was used. The light source in XPS was an unmonochromatized X-ray tube emitting Al-K_α radiation with 1486.6 eV photon energy. For ARPES measurements, the He-I line with a photon energy of 21.2 eV generated by an unmonochromatized He-VUV lamp (UVS 300) was utilized.

4.4 X-ray standing wave

To reveal the structure of 2D systems, LEED and STM are suitable tools, but lack element specific information. XSW, on the other hand, is a diffraction technique combined with the chemical sensitivity from PES that characterizes the structure with atomic resolution. As it will be discussed in Chapter 7, theory predicts that the vertical bonding distance of an In monolayer to the substrate has a drastic impact on its topological character. Using XSW, this bonding distance was revealed and will be presented in Chapter 8. In order to get an understanding of this technique, the principle behind XSW will be presented in the following based on the Refs. [80, 81].

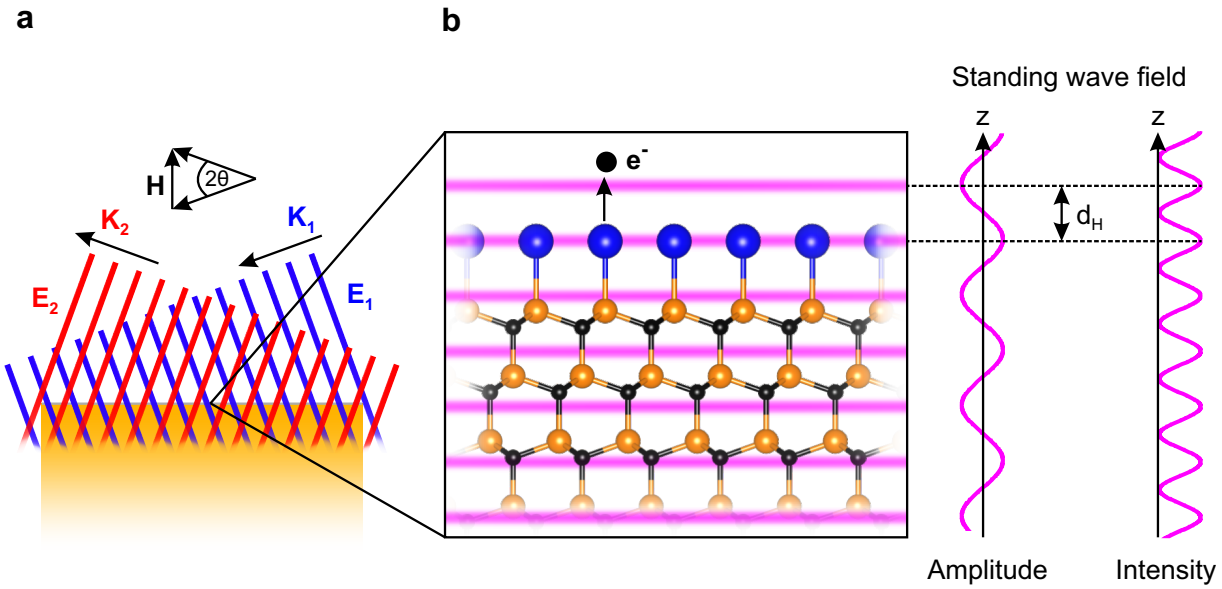

Figure 4.7: Formation and basic working principle of XSW – **a**, An incoming X-ray beam (blue) under grazing incidence of angle θ is Bragg-reflected from the crystalline sample (red). The superposition of both plane waves form an X-ray standing wave. $\boldsymbol{K}$ and $\boldsymbol{E}$ represent the propagation and electric field vectors of the photon beams, respectively. The diffraction vector $\boldsymbol{H}$ fulfills the Laue condition of $\boldsymbol{H} = \boldsymbol{K}_2 - \boldsymbol{K}_1$ with $|\boldsymbol{H}| = H = 1/d_H$, where d_H denotes the diffraction plane spacing illustrated in **b**. **b**, Close-up of the planar standing wavefield (pink) at the surface of a substrate (black and orange spheres) accommodating a covalently bonded overlayer (blue spheres). The periodic intensity profile of the XSW peaks locally at the overlayer and triggers the emission of a photoelectron that contributes to the total photoelectron yield measured by a hemispherical analyzer. Panels **a** and **b** after [80, 81].

A schematic illustration of the formation and utilization of the XSW technique is given in Figure 4.7. The actual XSW (pink lines) is generated by the superposition of incoming (blue) and Bragg-reflected (red) X-ray plane waves. The Bragg equation relates the scattering angle θ of the incident X-ray wave on a given diffraction plane (hkl) to the photon wavelength λ_{ph} and energy E_{ph}:

$$2\frac{d_{hkl}}{m}\sin\theta_B = \frac{\lambda_{ph}}{m} = \frac{hc}{E_{ph}}\,. \tag{4.24}$$

In Equation 4.24 m and θ_B denote diffraction at higher order planes and the Bragg angle, respectively. Note that diffraction planes do not generally correspond to lattice planes in a crystalline solid. When the Bragg condition is met, the vertical periodicity of the standing wavefield coincides with the spacing of the scattering planes d_{hkl} of the substrate crystal lattice (see Fig. 4.7b). The standing wavefield extends over a considerable volume even outside the crystal, since the incident X-rays penetrate deep into the sample. Adatoms or an overlayer on a sample surface are thus fully contained in this standing wavefield.

Varying the grazing angle θ or the photon energy around the Bragg condition changes the phase difference between the incoming and reflected X-ray beam by π. At the same time, the high reflection range of the solid's reflectivity curve is traversed. This essentially moves the planar standing wavefield along the z-axis of the sample lattice. When the maximum intensity is located in the vertical center of the overlayer, as depicted in Fig. 4.7b, the X-ray photons are absorbed and trigger a photoemission process. A hemispherical analyzer subsequently detects the photoelectrons and, thus, one is able to gain element specific information in combination with the overlayer location relative to the substrate diffraction planes.

In general a characteristic photoelectron yield $Y_A(\theta, E_{ph})$ of an element A is recorded as function of scattering angle or photon energy. With neglected multipole contributions the photoelectron yield can be expressed as:

$$Y_A(\theta, E_{ph}) \sim \int \rho(\boldsymbol{r}) I(\theta, E_{ph}, \boldsymbol{r}) d\boldsymbol{r}\,, \tag{4.25}$$

where $\rho(\boldsymbol{r})$ and $I(\theta, E_{ph}, \boldsymbol{r})$ are the spatial distribution of the photoemitter of element A and the standing wavefield intensity at position $\boldsymbol{r}$, respectively. This intensity results from the sum of the incident and scattered X-ray waves with amplitudes E_1 and E_2, respectively:

$$I = |1 + (E_2/E_1) \cdot \exp(-2\pi i \boldsymbol{H} \cdot \boldsymbol{r})|^2\,, \tag{4.26}$$

where $\boldsymbol{H} \cdot \boldsymbol{r} = z/d_H$ and z is the perpendicular distance of the photoemitter with respect to the diffraction planes separated by d_H. The reflectivity $R = |E_2/E_1|^2$ and the phase difference between incoming and reflected X-rays, Φ, simplifies Equation 4.26 to:

$$I = 1 + R + 2\sqrt{R} \cdot \cos(\Phi - 2\pi z/d_H)\,. \tag{4.27}$$

Atoms of an overlayer can generally be found in different positions, for example, when affected

by lattice vibrations, statistical disorder, or simply because different lattice sites are occupied. This position distribution $f(z)$ is incorporated into Equation 4.27, which yields:

$$\begin{aligned} I &= 1 + R + 2\sqrt{R} \int_0^{d_H} f(z) \cdot \cos\left(\Phi - 2\pi z/d_H\right) dz \\ &= 1 + R + 2\sqrt{R} f_{co} \cdot \cos\left(\Phi - 2\pi D/d_H\right). \end{aligned} \tag{4.28}$$

In Equation 4.28, f_{co} and D describe the *coherent fraction* and *coherent position*, respectively. Both parameters dictate the structural dependence of the measured photoelectron yield function given in Equation 4.25 and are determined by fitting the experimental data. Assuming a singly occupied layer with no disorder and a certain distance to the sample, f_{co} becomes one and the coherent position is defined by the actual bonding distance.

For the investigation of the In monolayer presented in Chapter 8, the (0004) diffraction plane of the 4H-SiC(0001) substrate was used. The XSW experiment was conducted in normal incidence geometry at the I09 beamline at the Diamond Light Source (United Kingdom).

5 Al on SiC(0001): Growth and Characterization

In this chapter, it is shown that Al high-coverage phases form a triangular and rectangular surface reconstruction with a surprisingly large unit cell. Their distinct LEED pattern is brought into accordance with the lattice structure found in STM. After thermal treatments, quasi-1D structures emerge on the surface that are similar to the herringbone reconstruction from Au(111). With the help of the latter, a first structural model for the quasi-1D Al phase is proposed. A $(\sqrt{3}\times\sqrt{3})$ lattice, i.e., the Al buffer layer, could not be found experimentally. All phases presented here are unknown in the literature.

5.1 Experimental prearrangements and growth process

For the growth, an Al foil of 99.999% purity was used. Prior to the growth process, the Al effusion cell was ramped up to 1075 °C and kept there for approximately 2.5 to 3 hours. Due to the large temperature difference between the melting points of Al (660 °C [82]) and oxidized Al (e.g. Al_2O_3: 2054 °C [83]), this preheating step effectively clears the surface of the Al melt by moving the solid oxidized content aside. This minimizes Al oxides in the molecular beam that would impinge on the SiC surface. Also, the molten Al material is known to tend to creep out when it wets the crucible walls. The cold lip at the upper end of the crucible (see, e.g., Ref. [84]) prevents further damage of the effusion cell and the UHV system in general.

The growth process of Al on SiC comprises of a two-step approach where the sample's temperature-time profile is depicted in Fig. 5.1. In each of the steps, the hydrogen passivation of the SiC surface was removed by heating the substrate with direct current to approximately 600 °C and kept constant for $t_1 = 1$ min. This process step is kept short to prevent the generation of a Si-rich $(\sqrt{3} \times \sqrt{3})$ reconstruction of the SiC substrate, which also occurs at such elevated temperatures [56, 85]. Other studies determined that this thermal treatment effectively desorbs the hydrogen coverage from the substrate resulting in an unreconstructed SiC(0001) surface [56, 85, 86].

Only after removal of this passivation layer is it possible to have the Al adlayer covalently bonded to the substrate. Simultaneously, Al is continuously evaporated on to the sample. Due to holding the sample at such high temperatures and having the hot Al effusion cell in close distance, Al atoms are too mobile to adhere to the substrate surface, which prevents the formation of a closed film. Therefore, the substrate temperature was lowered to roughly 250 °C in an Al

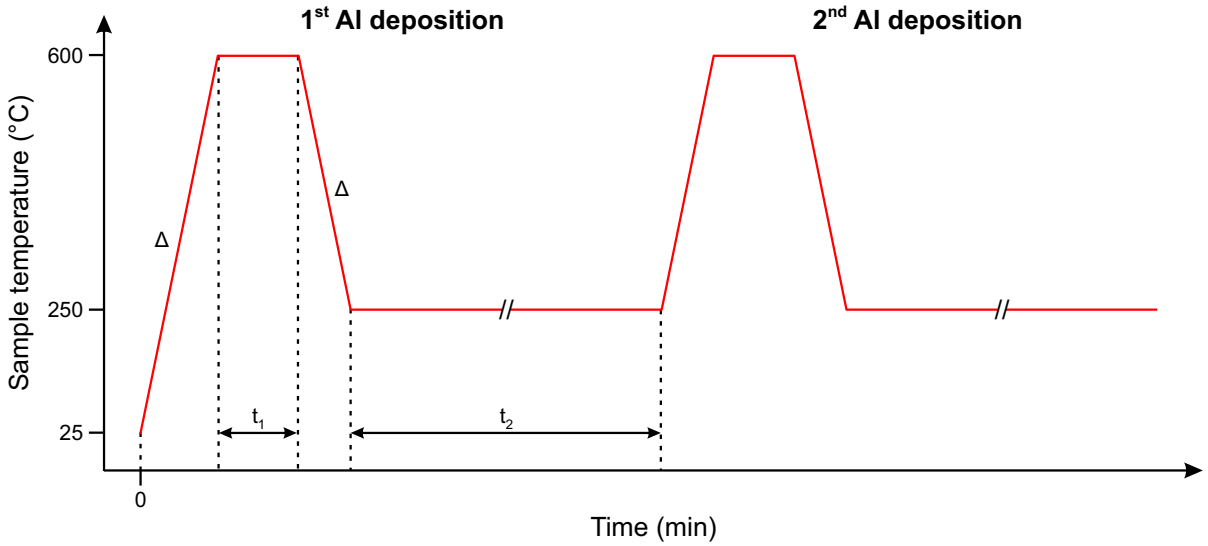

Figure 5.1: Substrate's temperature-time profile during two Al growth steps – For hydrogen desorption the sample was heated to 600 °C with a direct current ramping rate of $\Delta = 0.05\,\mathrm{A\,s^{-1}}$ and kept at that temperature for 1 min (t_1). Al accumulation took place in two subsequent process steps for 5 min and 10 min (t_2) at 250 °C. This forms uniformly closed Al films.

accumulation step. In a $t_2 = 5$ min (first growth step) and 10 min (second growth step) long process, most of the Al enrichment took place. Two enriching steps are necessary to form well-ordered Al surface lattices over long ranges, as it will be presented below. The formation of such lattices is also promoted by the temperatures used here, which sufficiently activate Al atoms on the surface.

5.2 Triangular and rectangular Al high-coverage phase

5.2.1 Analysis of Al-induced LEED pattern

After the growth procedure and an annealing step at 400 °C for two minutes to desorb loosely bound surface contaminants, the sample was characterized by LEED (see Fig. 5.2). As depicted in Fig. 5.2a, the intense but broad diffraction spots suggest a thin and insufficiently ordered Al overlayer with no characteristic surface reconstruction. The LEED pattern represents essentially the SiC(0001) substrate (cf. Fig. 5.2b) with its characteristic spots highlighted by red circles. Only after the second Al deposition additional bright spots (green circles) next to the most intense diffraction spots emerge (see Fig. 5.2b). The symmetry of the pattern follows the substrate surface and is marked by the unit cell (red dashed rhombus).

A more detailed insight can be seen in Fig. 5.2c and d, which show the LEED image of a sample rotated by approximately 15°. The substrate-induced diffraction spot is clearly surrounded by a hexagon-like spot arrangement, indicated by a black dashed hexagon. In between the substrate-induced and hexagon-like spot arrangement, another bright diffraction spot appears, which is highlighted by a white circle. In both LEED patterns the diffraction spots appear along the

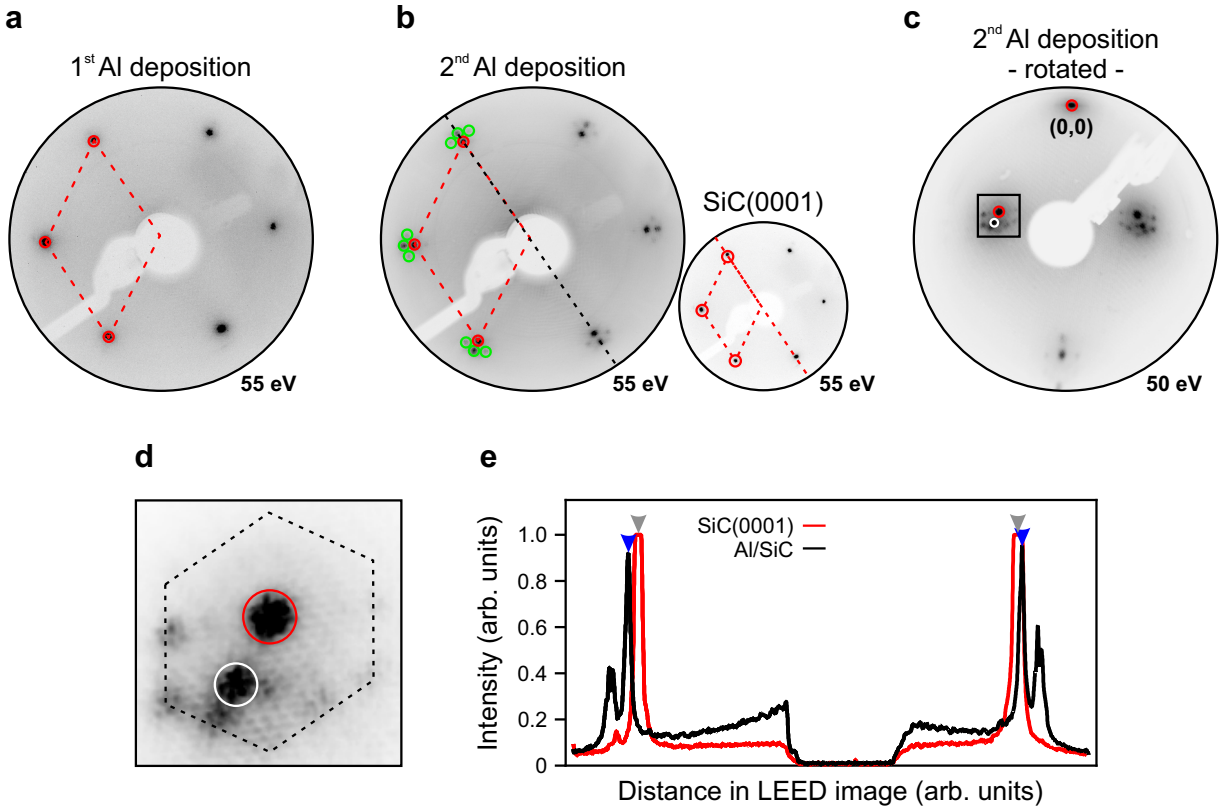

Figure 5.2: Emerging of Al-induced LEED spots – After the first Al deposition, only substrate diffraction spots are visible in LEED (**a**; highlighted by red circles). Additional diffraction spots only emerge after a second Al deposition step (**b**; highlighted by green circles). The most intense spots coincide almost completely with the characteristic substrate spots, as shown by the intensity profile (**e**) taken along the black and red dashed lines in both LEED images. This is indicative for a strained Al film. The small LEED image depicts a clean SiC(0001) surface. The (0,0) spots are hidden by the electron gun. The substrate unit cell is depicted as a red dashed rhombus in **a** and **b**. **c**, The LEED image rotated away from the (0,0) spot by approximately 15°, highlights the diffraction spots of the Al surface reconstruction. **d**, Close-up of **c** shows the hexagon-like pattern (dashed black hexagon) around the substrate-induced diffraction spots. An additional bright spot appears (white circle) close to this substrate-induced spot in the center. **e**, Intensity profile from the LEED images in **b**. A slight misalignment of the sample distance to the LEED setup is attributed to the deviation of a complete fusion of the diffraction spots.

high-symmetry directions and around the substrate-induced LEED spots more intensely than elsewhere in reciprocal space. This could be due to a structure factor that modulates the intensity distribution within the diffraction pattern [62]. Further insights could be provided by the spot-profile analysis LEED (SPA-LEED) technique. However, this was not the focus here. Overall, the sharpness and the low level of background intensity of the LEED pattern suggest an atomically well- and long-range ordered Al-induced surface reconstruction.

An XPS analysis of a representative sample also demonstrates the high growth quality, where only characteristic Al and substrate core-level peaks are found. The Al coverage is estimated by XPS to approximately $\Theta_{ML} \approx 2.2$ ML (see Sec. A.1 for full XPS analysis). Thus, the rather long Al deposition steps during the growth lead to the formation of an Al high-coverage phase on SiC(0001). The attenuated substrate-induced LEED spots shown in Fig. 5.2b also indicate a

thicker Al layer.

Taking an intensity profile along the black and red dashed line, depicted in Fig. 5.2e, shows that the most intense spots coincide almost completely with the substrate-induced spots. The deviation from complete fusion of the diffraction spots is attributed to small misalignments of the sample distance to the optical LEED setup. The present fusion is indicative of a strained Al film. A relaxed Al(111) overlayer on the other side exhibits a lattice constant of 2.85 Å (bulk value) [87]. In this case, the distance between the diffraction spots of the corresponding LEED pattern would be approximately 7.4% larger compared to the substrate. Interestingly, the characteristic bright spot next to the main substrate-induced one is also clearly visible in the black intensity profile in Fig. 5.2e. It is important to note that both LEED images in Fig. 5.2b were taken at the same electron energy.

5.2.2 Investigation of the Al surface lattices at the atomic scale

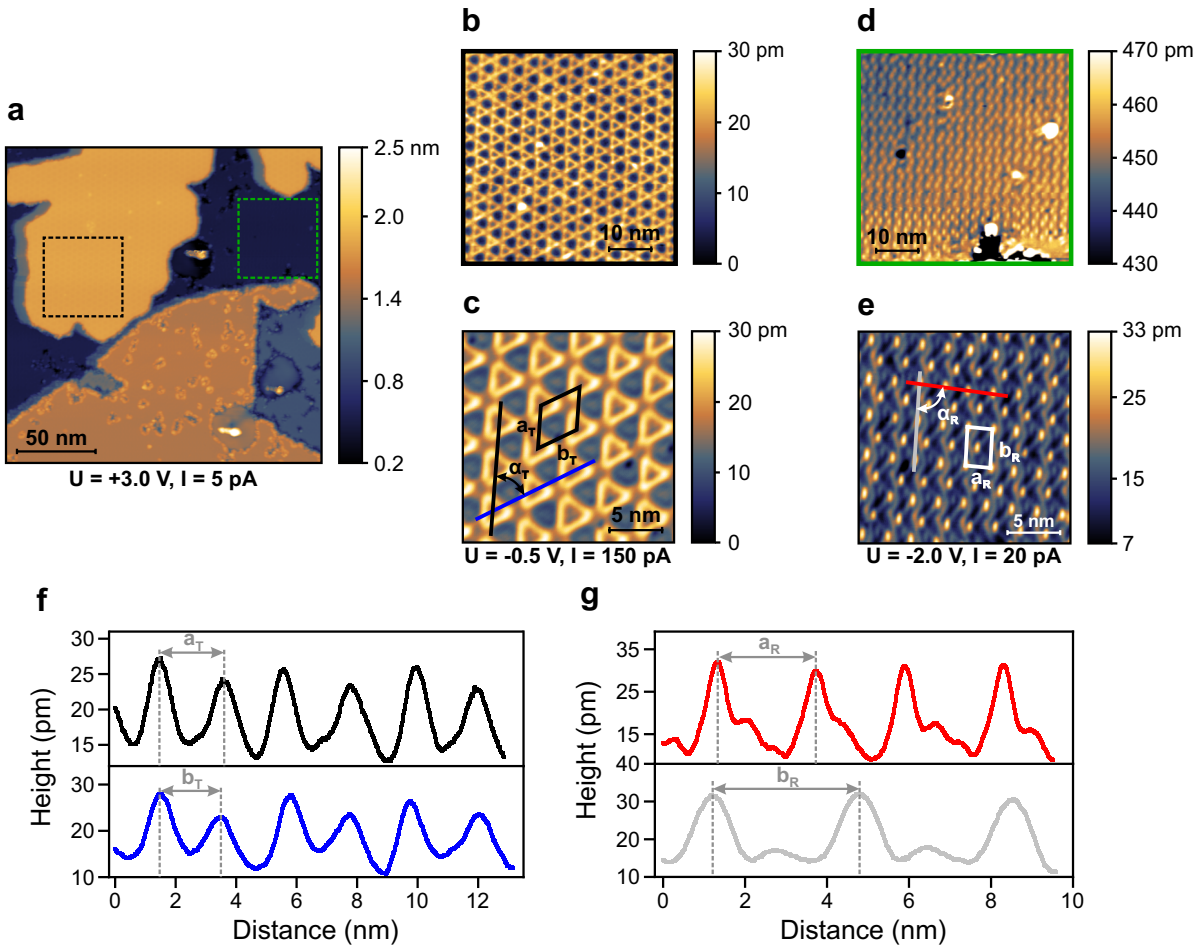

Figure 5.3: Triangular and rectangular Al phases in STM – **a**, STM overview scan displays large substrate terraces covered with the two most prominent coexisting surface reconstructions: the triangular (**b** and **c**) and rectangular Al phase (**d** and **e**). Their lattice parameters and unit cells are illustrated in **c** and **e**. The height profiles of the triangular and rectangular phases taken along the colored lines in **c** and **e** are depicted in **f** and **g**, respectively.

To get a more comprehensible picture of the Al reconstruction and to understand the resulting LEED pattern, the surface topography was investigated by STM. The overview topography image displayed in Fig. 5.3a shows large substrate terraces covered with Al. Step heights and edges are analyzed in detail in Section A.2, and referred to in the following. Characteristic for the 4H-SiC(0001) substrate unit cell, the step heights are in the range of approximately 5 to 10 Å, although a first indication of an Al film thickness is present. Additionally, the terrace edge geometry reflect the threefold symmetry imprinted by the SiC(0001) substrate.

Close-ups taken at different positions in the overview scan reveal two prominent and coexisting Al phases: the triangular phase in Fig. 5.3b and the rectangular Al phase in Fig. 5.3d. The unit cell dimensions of both phases were found to be surprisingly large (see Fig. 5.3c and e) and are presented in Table 5.1. Atomically resolved STM topography images of both phases, which would provide information about the structural configuration at the atomic level, could not be obtained. Both phases occur basically everywhere on the sample surface, irrespective of a temperature gradient of about 10 to 15 °C during growth.

Triangular Al phase			Rectangular Al phase		
a_T (Å)	b_T (Å)	α_T (deg)	a_R (Å)	b_R (Å)	α_R (deg)
41.52 ± 1.25	41.52 ± 1.25	59.1 ± 1.0	23.46 ± 0.70	36.64 ± 1.10	87.4 ± 1.0

Table 5.1: Unit cell dimensions of the triangular and rectangular Al phases from STM – All items listed here are depicted in and taken from Fig. 5.3c, e-g.

5.2.3 Emergence of the diffraction pattern

Upon determining the geometrical properties of the unit cells, it is now possible to trace the diffraction pattern observed in LEED and understand its formation. The unit cell geometries from Tab. 5.1 are utilized to simulate the respective LEED pattern with the *LEEDpat* software [88] and are illustrated in Figure 5.4. A lattice constant of 3.07 Å [42] and the hexagonal space group $P6_3mc$ [89] is assumed for the underlying substrate surface.

To confirm the simulated diffraction patterns of each Al phase, they are overlayed with Fourier-transformed and symmetrized STM data of the triangular and rectangular Al phases from Fig. 5.3c and e, respectively. Since the macroscopic electron spot averages spatially over multiple domains in the experiment (see for example Fig. 5.5c), the 2D fast Fourier transform (FFT) patterns are symmetrized by 120° to account for the threefold-symmetric substrate. Along the same line, all possible domains are included in the simulation. As can be seen in Fig. 5.4b and d, both simulated LEED pattern fit well to the 2D FFT images. A commensurate surface reconstruction of

$$\mathbf{M_T} = \begin{pmatrix} 14 & 0 \\ 14 & 14 \end{pmatrix} \quad \text{and} \quad \mathbf{M_R} = \begin{pmatrix} 5 & 9 \\ -12 & 0 \end{pmatrix} \tag{5.1}$$

for the triangular and rectangular Al phase is identified, respectively. The absolute values of the unit cell dimensions listed in Tab. 5.1 would result in decimal matrix entries in Eq. 5.1.

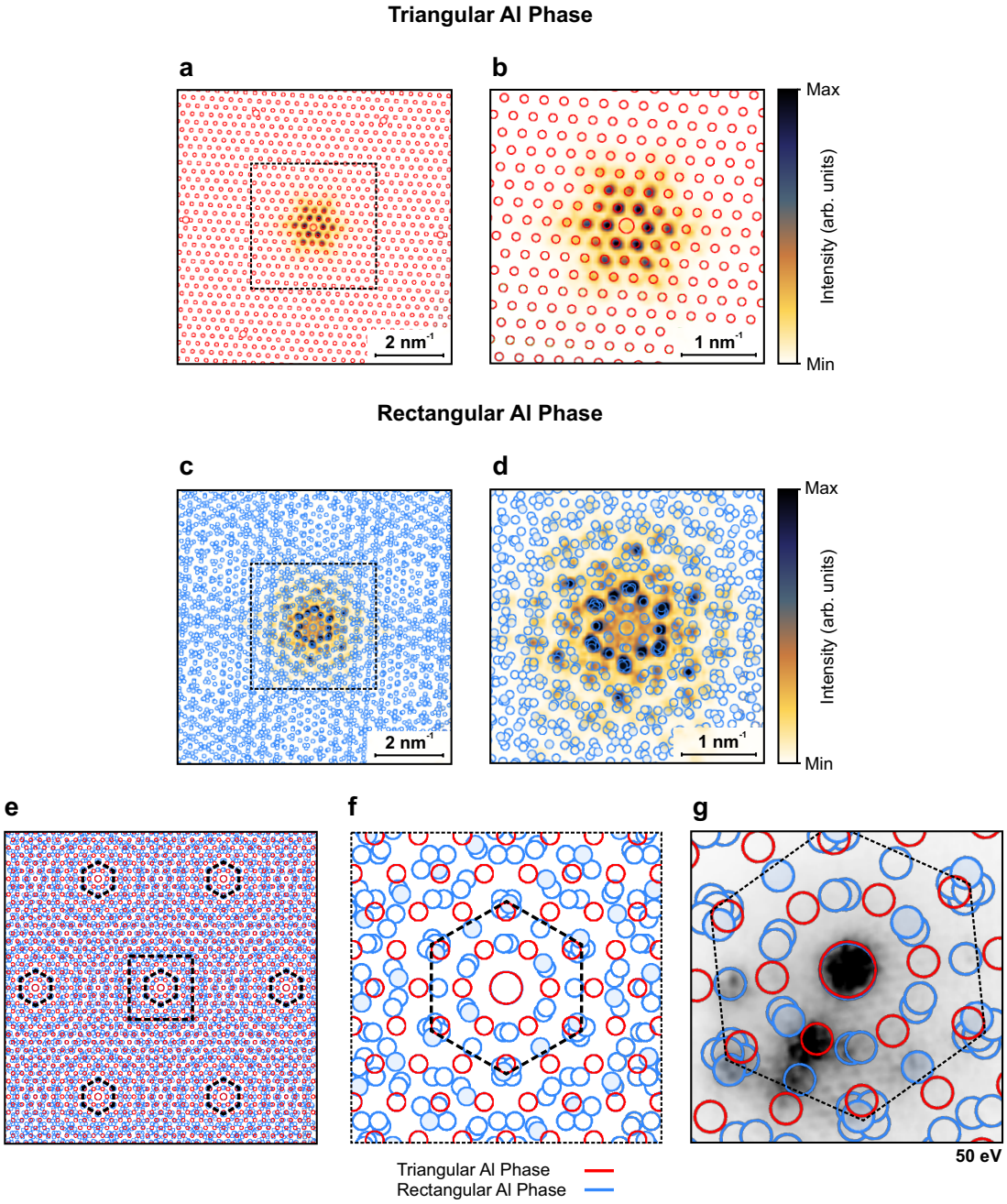

Figure 5.4: Diffraction patterns of triangular and rectangular Al phases – **a-d**, The symmetrized 2D FFT images based on Fig. 5.3c and e agree well with the respective overlayed and simulated diffraction patterns. The surface reconstruction is expressed in matrix notation in Eq. 5.1. For the simulated diffraction pattern, the underlying substrate lattice is assumed to have a lattice constant of 3.07 Å [42] and the hexagonal space group $P6_3mc$ [89]. The unit cell dimensions for the Al adlayer was taken from Tab. 5.1. **e-f**, The superposition of simulated LEED patterns derived in **a-d** yield a hexagon-like spot arrangement around substrate-induced spots (black dashed hexagon). The zoom-in (**f**) shows a concentric spot arrangement within this hexagon. **g**, The simulated LEED pattern laid on top of the experimental one from Fig. 5.2d agree well. Both coexisting Al phases therefore form the observed LEED pattern.

Measurement uncertainties from STM are therefore taken into account by rounding these entries to the nearest integers. The lattice constants of the reconstructions derived in Eq. 5.1 yield

$a_T^* = 42.98\,\text{Å}$, $a_R^* = 23.98\,\text{Å}$, and $b_R^* = 36.84\,\text{Å}$. The values are, except for a_T^*, within the error bars of the values presented in Tab. 5.1. Although, even a_T^* is still close to the upper error bar of a_T.

A superposition of both identified simulated diffraction pattern is further generated (see Fig. 5.4e, f). Around the center of the first- and higher-order Brillouin zones, a hexagonal spot arrangement emerges (black dashed hexagon) that reproduce the observed LEED pattern to a great extent. And indeed, the superposition of both simulated diffraction pattern agrees well with the LEED image from experiment, as can be seen in Fig. 5.4g. Also the concentric arrangement of spots around the substrate-induced main spot in the center, fits to the experimental data well

Hence, the LEED image is a product of both Al-induced reconstructions coexisting on the sample surface, in accordance with the STM data shown in Fig. 5.3. Interestingly, the bright spot (small red circle in Fig. 5.4g) next to the main spot in the center, originates in the triangular Al phase. Compared to the simulated diffraction pattern, many spots in the experimental LEED image are absent. As mentioned previously, this could possibly be due to a kinematic structure factor.

5.2.4 Other rarely occurring Al phases

In addition to the described triangular and rectangular reconstruction, Figure 5.5 illustrates other rarely occurring Al phases that are also observed on the surface of one sample. These phases occurred directly after Al deposition. The overview STM topography image in Fig. 5.5a shows large substrate terraces with different surface reconstructions. The least frequently occurring Al phase is the distorted triangular reconstruction depicted on the right side of Fig. 5.5b. It is directly adjacent to the triangular phase and separated by a domain wall.

On length scales of several hundred nanometers, a triangular-like Al reconstruction, shown in Fig. 5.5d, appears. This phase is called triangular-like to avoid confusion with the triangular Al phase. The lattice constant of $(44.01 \pm 1.32)\,\text{Å}$ for the triangular-like phase is of the same order of magnitude as that of the triangular and rectangular Al phase. In addition, the height distribution across the triangular and triangular-like reconstruction reveals $(1.37 \pm 0.14)\,\text{Å}$ (see Fig. 5.5e and f), which differs significantly from substrate step heights dictated by the unit cell. Hence this value indicate the film thickness of the triangular Al phase. However, corrugation values from STM generally depend on the tunneling parameters used and the local electronic structure of the surface, which prevents an unambiguous thickness determination here. No traces were found in LEED that would indicate Al phases other than the triangular and rectangular reconstructions. This is probably due to the seldom occurrence of the Al phases on the sample discussed here.

Furthermore, different domains of the rectangular phase, each rotated by a 120°, are found, which reflect the threefold symmetry imprinted by the substrate surface.

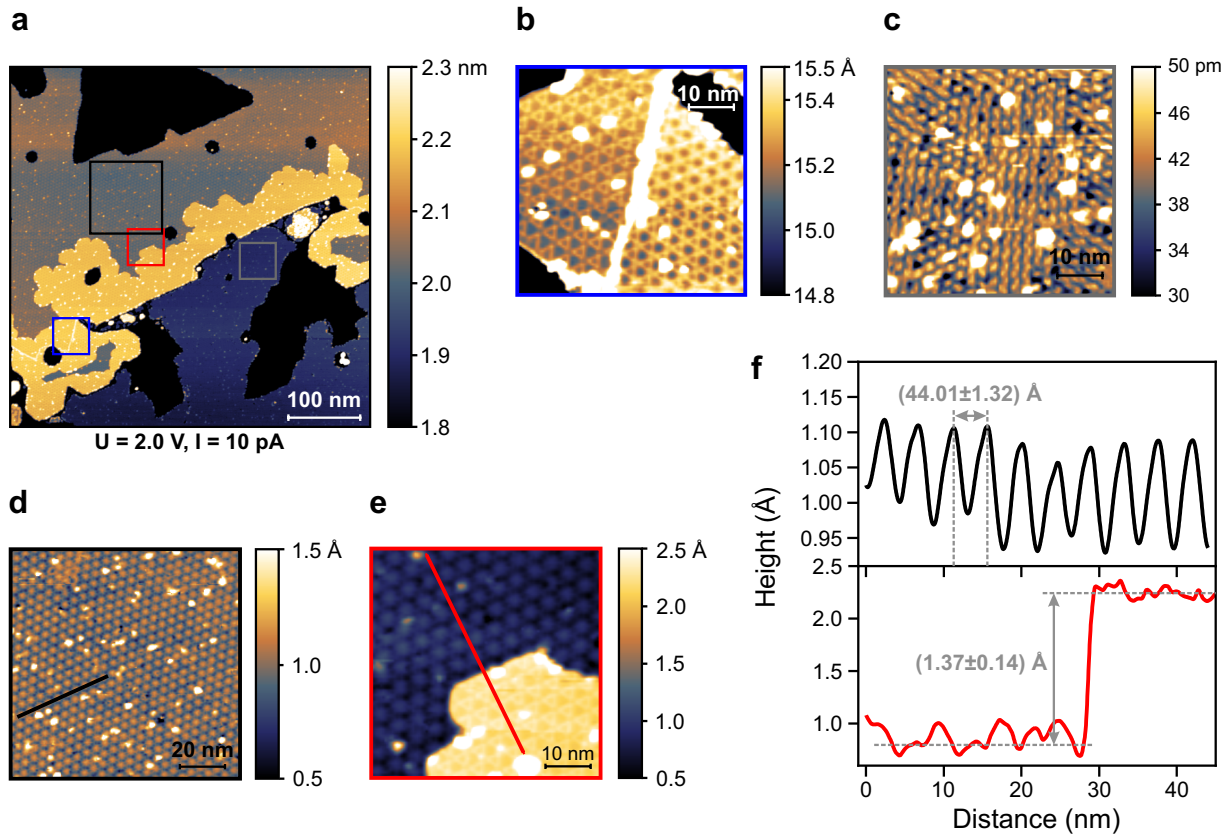

Figure 5.5: Rarely occurring Al phases in STM – **a**, The overview STM image host two rarely observed Al phases shown in **b** and **d**. Due to their seldom occurrence, a characteristic LEED pattern could not be identified. **b**, A patch of a triangular (left) and a distorted triangular Al phase (right) separated by a domain wall. **c**, A rectangular phase with different domains induced by the substrate symmetry. **d**, The triangular-like Al phase is well-ordered on a scale of hundreds of nanometers and appears significantly different than the triangular Al reconstruction. **e**, The step height between a triangular-like and triangular Al film patch indicates a layer thickness of the latter Al phase. **f**, Height profiles along the black and red line in **d** and **e**, respectively.

5.3 Quasi one-dimensional Al phase

5.3.1 The striped Al-$(7 \times \sqrt{3})$ reconstruction in STM

After annealing at 500 °C for approximately 30 min, the Al coverage start to reduce and larger patches of less covered SiC appear, as indicated by black arrows in Fig. 5.6a. However, on some terraces the triangular and rectangular Al high coverage phases seem to be present (see Fig. 5.6b and g).

Upon closer inspection, however, the rectangular phase is now interrupted over a large area, as can be seen particularly well in Fig. 5.6b. Changing to the occupied states uncovers linear, quasi-1D stripes that separate domains of the rectangular phase (see Fig. 5.6c). When extrapolated diagonally through the rectangular unit cell (white dashed line), the quasi-1D stripes appear to connect directly to another domain of the rectangular phase. In a small section, the rectangular phase also seem to wind around a defect and form a vortex-like feature, which is highlighted by a dashed white circle in Fig. 5.6c and d.

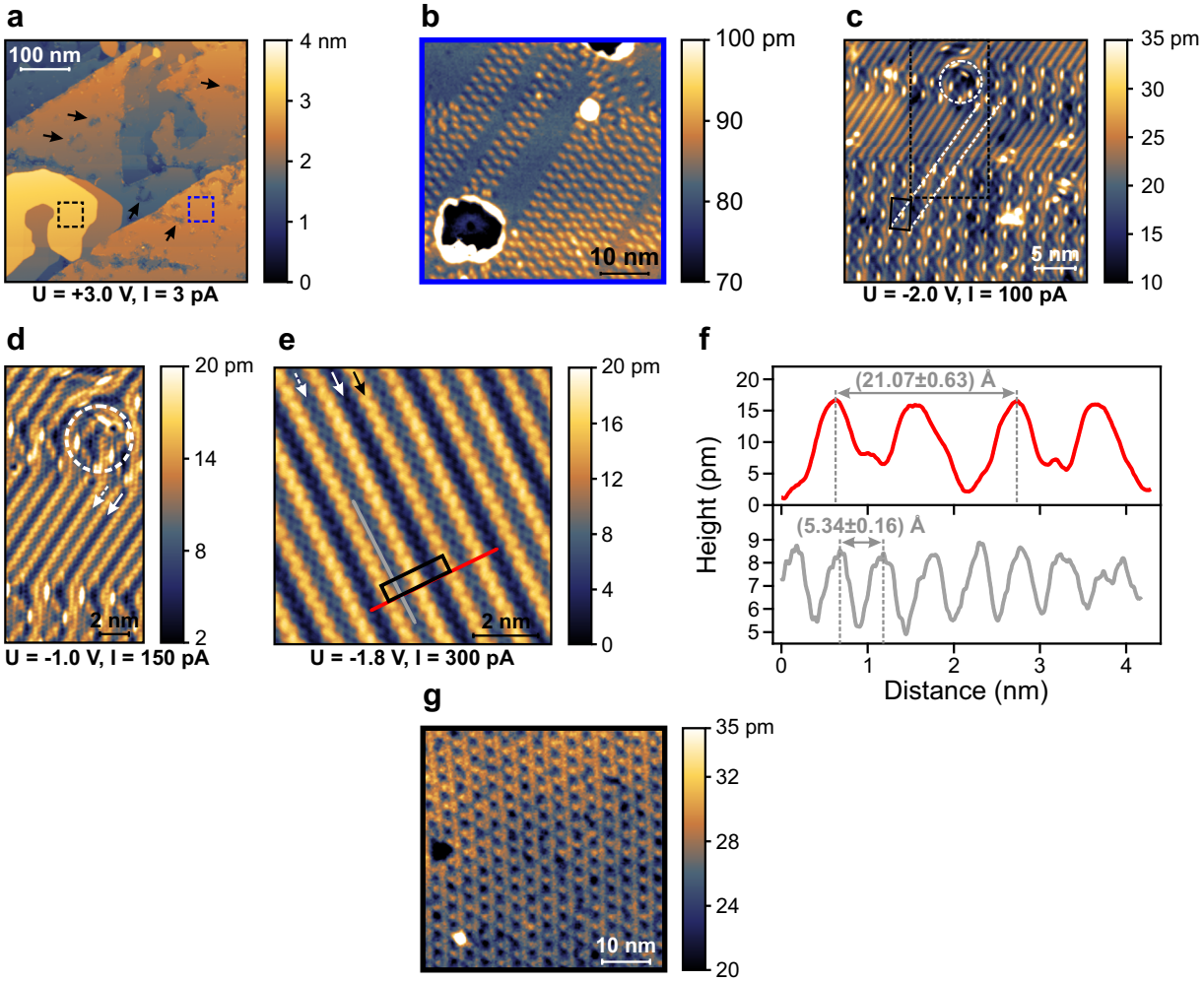

Figure 5.6: $(7 \times \sqrt{3})$ quasi-1D Al phase at the atomic scale – **a**, Annealing at 500 °C for approximately 30 min led to Al desorption and the creation of larger patches of less Al coverage (black arrows). The triangular (**g**) and rectangular Al phase are still present, although the latter exhibits disconnected domains that are well visible in **b**. **c**, Changing the bias voltage reveals a quasi-1D Al phase within those separated areas, that extends diagonally (dashed white lines) through the rectangular unit cell (black rectangle) to another domain. **d**, The dashed and solid white arrows mark two areas of different heights within the pairwise feature. In addition, a vortex-like winding of the rectangular phase around a defect (dashed white circle) is present. **e**, High-resolution close-up of the quasi-1D phase. The red and gray line profiles (depicted in **f**) determine the $(7 \times \sqrt{3})$ unit cell (black rectangle) of this quasi-1D Al phase. The black arrow indicates a zigzag-like corrugation on either side of the double-row.

Interestingly, the areas in between the pairwise stripes are on two different height levels. Here, a deep trench clearly separates a double-row of the quasi-1D phase, as indicated by the solid and dashed white arrow in Fig. 5.6d and e, respectively. At other bias voltages, a zigzag-like formed corrugation on either side of the double-row marked by a black arrow can be identified (see Fig. 5.6e). The lower-lying trench in between however reveals a zipper-like structure (solid white arrow in Fig. 5.6e). With the height profile in red and gray shown in Fig. 5.6f the dimensions of the unit cell are determined to be (21.07 ± 0.63) Å and (5.34 ± 0.16) Å. Along with the other found Al phases on SiC, the quasi-1D phase also exhibits a surprisingly large surface lattice

constant perpendicular to the pairwise features. With respect to the SiC(0001) surface lattice constant, this periodicity represents a factor of 7, whereas a factor of $\sqrt{3}$ is found in between the double-row parallel to the stripes. Thus a commensurate surface reconstruction of $(7 \times \sqrt{3})$ on SiC(0001), depicted as a black rectangle in Fig. 5.6e, is identified.

5.3.2 Similarities with the Au(111) herringbone structure

In the following, the focus lies on understanding the occurrence of this new Al phase. These pairwise, quasi-1D structures have some striking similarities with the well-known herringbone reconstruction on the Au(111) surface [90–93]. The most obvious similarity is the pairwise, atomically corrugated structure separated by a deep trench, as observed in STM. But also the height of the double-row marked by the black arrow in Fig. 5.6e is with roughly 15 pm (see red height profile in Fig. 5.6f) close to the (20 ± 5) pm observed for Au(111) [91].

Due to these striking similarities, the key mechanism that forms the herringbone reconstruction will be transferred and adapted to the Al lattice of the quasi-1D phase in the following. In doing so, a first structural model can be proposed.

The driving force behind the formation of the herringbone reconstruction is that 23 Au atoms on the surface are sitting on top of 22 atoms of the second layer [91, 94]. Due to the resulting uniaxial compression along one direction, Au atoms occupy on the surface both hexagonal close-packed (hcp) and face-centered cubic (fcc) sites and, thus, forming a $(22 \times \sqrt{3})$ surface reconstruction [92–94]. Au atoms in transition regions between a fcc and hcp stacking domain are arranged fairly compact, which forces them to occupy a vertically elevated position with respect to the surface plane [93]. The sequence of fcc and hcp regions lead then to the characteristic pairwise structures, i.e., the herringbone reconstruction [94].

5.3.3 Proposing a first structural model for the quasi-1D Al phase

Adapting this principle on a commensurate Al overlayer on SiC(0001) is schematically illustrated in Figure 5.7. Here, Al atoms on the surface are either located on the hcp (left, blue spheres) or fcc sites (right, red spheres). The underlying strained Al lattice (gray spheres) adapts the SiC(0001) registry. In the transition regions, highlighted by the overlapping backgrounds, both domains coalesce leading to densely packed Al atoms. In regions marked by yellow boxes, this dense packing generates a corrugated topography, i.e., the striped features observed in the quasi-1D structure, which bears a resemblance to the herringbone structure. The white arrows mark Al atoms occupying the characteristic edges of the transition regions. Furthermore, the distance between the center of these close-packed regions represent exactly the $\sqrt{3}$ factor of the substrate surface lattice constant, which was determined in Fig. 5.6f (gray height profile).

The transition regions occur pairwise within the $(7 \times \sqrt{3})$ unit cell that spans perpendicular across a hcp and fcc stacking domain, respectively (see Fig. 5.6e). However, there are essentially two different ways of forming the identified pairwise quasi-1D features. Either both stacking domains share the total unit cell length equivalently, i.e., 3.5 unit cell lengths for both a hcp

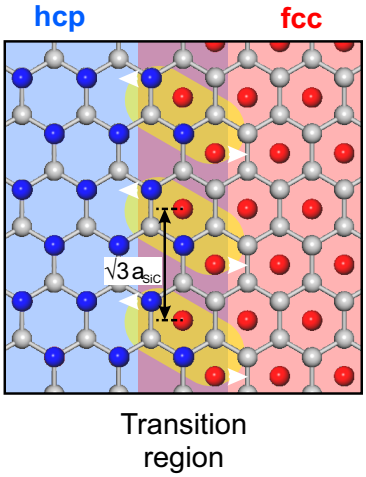

Figure 5.7: Design principle behind the proposed structural model for the quasi-1D Al phase – Schematic illustration of the transition from Al atoms occupying hcp (left side, blue spheres) to fcc sites (right side, red spheres) on the surface of a Al lattice (gray spheres) commensurable with SiC(0001). Yellow boxes mark the particularly densely packed Al atoms in the transition region, which form the striped features of the quasi-1D phase. They are periodically separated by $\sqrt{3} \cdot a_{SiC}$ (cf. gray height profile in Fig. 5.6f). White arrows highlight Al atoms at the edge of the transition region. This design principle depicted here is inspired by the herringbone structure from Au(111) and serves as basis for the proposed structural model. After [95].

and fcc region or as the herringbone structure on Au(111) favors [91], a slightly smaller hcp region compared to its fcc counterpart. Both scenarios are illustrated in Fig. 5.8b and e with the $(7 \times \sqrt{3})$ unit cell indicated as dashed black box.

After the design principle of both structural models is understood, they will be overlayed with high-resolution topographic STM images from two different regions, as depicted in Fig. 5.8c-g. The shape of the close-packed parts in the transition regions agree well with the STM data. In addition, the lattice periodicity in between the quasi-1D features correspond particularly well with the experimental observation. The two regions depicted in the STM data are only a few nanometers apart (see Fig. 5.8h). Therefore, it seems that both models occur simultaneously and are equally present on the surface.

The sharp diffraction spots of the symmetrized 2D FFT from Fig. 5.8h coincide well with the simulated diffraction pattern of the $(7 \times \sqrt{3})$ unit cell, as can be seen in Fig. 5.8i. For the simulation, the unit cell dimensions derived in Fig. 5.6e, f are used. The well-matching diffraction patterns further support the characterized geometry and dimensions of this unit cell. However some spots, in particular close to the center, are missing in the 2D FFT image. A possible explanation could be the local electronic contribution that alters the tunneling signal in STM, since Figure 5.8h does not necessarily represent the atomically resolved structure. Thus, the corresponding 2D FFT pattern in Fig. 5.8i lack structural information. Atomic force microscopy, for example, would provide here a much better insight of the topography at the atomic level. The unit cell can then be mapped more accurately, allowing for more detailed structural analysis, for example. This could uncover internal symmetry operations, such as glide reflections that would also affect the simulated diffraction pattern.

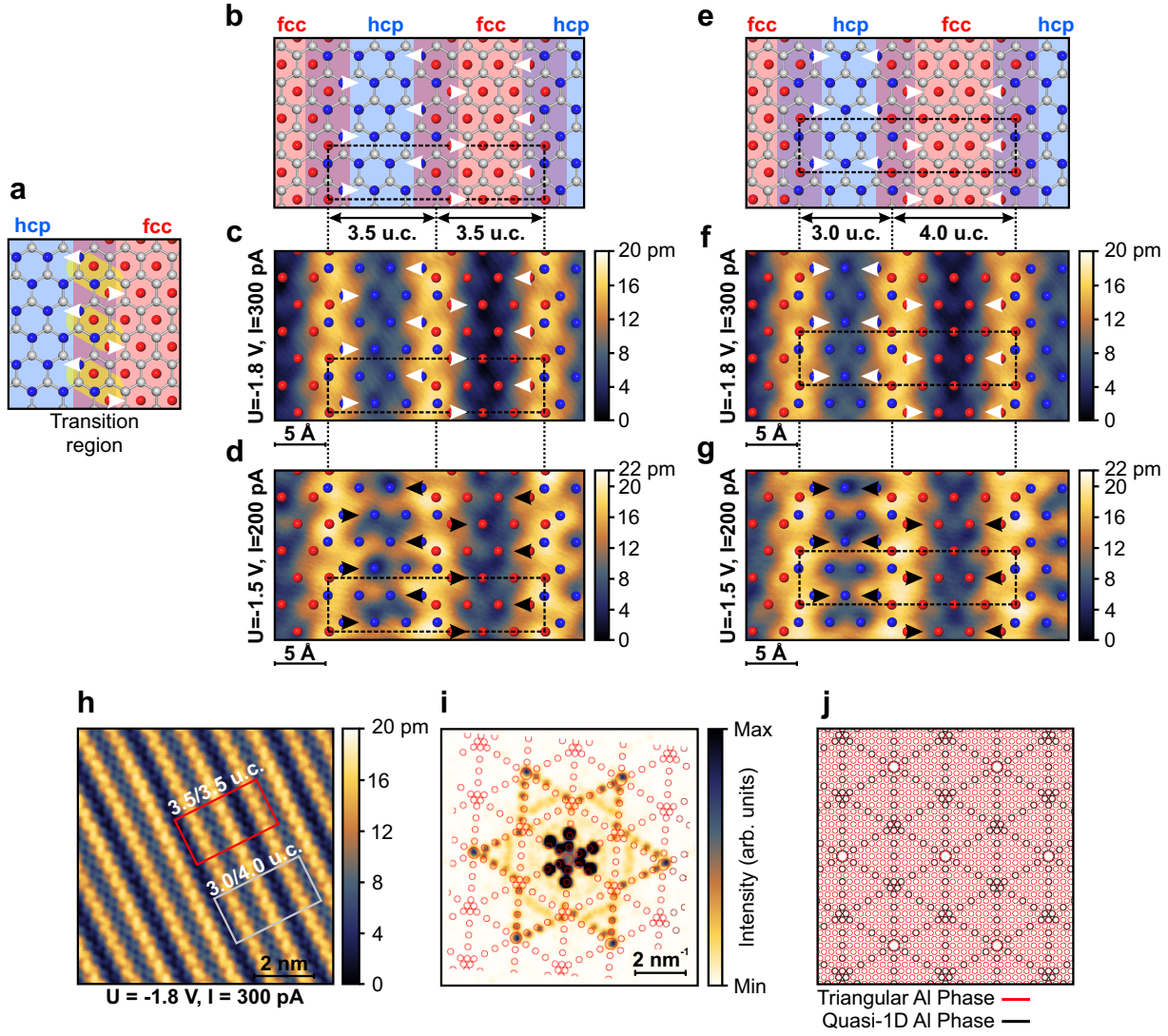

Figure 5.8: Proposed structural models for the quasi-1D Al phase – **a**, Schematic illustration from Fig. 5.7. **b**, Equally large hcp and fcc regions form the 3.5/3.5 unit cell structural model. **c-d**, Overlay of the structural model from **b** and constant current STM topography scans. **e**, Slightly larger fcc region compared to hcp lead to the 3.0/4.0 unit cell structural model. **f-g**, Overlay of the structural model from **e** with constant current STM topography scans. The $(7 \times \sqrt{3})$ unit cell is depicted as a dashed black rectangle in **b-g**. **h**, STM image from Fig. 5.6e highlights two regions in which the structural models occur. **i**, Symmetrized 2D FFT data of **h** overlayed with the simulated diffraction pattern of the $(7 \times \sqrt{3})$ reconstruction (red circles) underpin the correctly identified geometry and dimensions of this unit cell. For the simulation, the substrate surface lattice constant was assumed to be 3.07 Å [42] with a hexagonal space group symmetry of $P6_3mc$ [89]. **j**, Simulated LEED pattern of the triangular Al phase entirely mask the pattern of the quasi-1D phase. The coexistence of both phases leads to the indistinguishability of both patterns in LEED. Figure in **a**, **b**, and **e** after [95].

Nevertheless, a clear indication of this Al phase could not be found in LEED. One possible explanation is that all diffraction spots of the quasi-1D phase coincide with those from the triangular Al phase (see Fig. 5.8j). Since both phases coexist on the sample surface, the diffraction pattern of both phases can not be distinguished after LEED spatially averages the sample surface on a macroscopic scale. Another possibility is that this phase occupies only a small fraction on the sample surface, which results in low-intense diffraction spots in LEED. Overall, a first potential

structural model of the quasi-1D Al phase is proposed, which fits well to the obtained STM data.

5.3.4 Quasi-1D structures of metal adlayers – A literature overview and comparison

Interestingly, heteroepitaxial growth of metal films in the (multi-) monolayer regime on metallic as well as semiconducting substrates form similar striped corrugations on the surface. Famous examples are Cu on Ru(0001) [96–98], Fe, Co, and Cr on Re(0001) [99], and Pb on Ge(111) and Si(111) [100]. In the case of, e.g., Cu/Ru(0001) the strain induced by the lattice mismatch is reduced in the second layer by forming periodic unidirectional misfit dislocations similar to the herringbone structure on Au(111) [96, 98]. The free energy of such a surface system depends on the adsorbate-substrate coupling strength and the strain induced by their respective lattice mismatch [101, 102]. By minimizing this free energy a self-organization of the heteroepitaxial grown films can occur in theory with the formation of a striped, honeycomb, and triangular structure on length scales of up to a micrometer [101, 102]. The periodic length scale of the striped superstructure crucially depends on the strain and coupling strength and increases with the latter parameter [102].

Due to a lattice constant of 2.85 Å of a bulk Al(111) layer [87], the Al film on SiC(0001) exhibits a lattice mismatch of approximately 7.4% and is, thus, tensile strained (cf. Fig. 5.2b and e). Hence, the quasi-1D Al phase is likely to result from an interplay of a yet unknown coupling strength of the Al overlayer with the SiC(0001) substrate and their lattice mismatch. In addition, the theoretical model derives a honeycomb pattern under certain conditions, where atoms occupy alternately fcc and hcp lattice sites [102]. The resulting structure resembles strongly the observed triangular Al phase.

5.4 Annealing of Al/SiC(0001)

In order to explore potential lower Al coverage phases, the Al-SiC sample was annealed in several, successive steps in a temperature range of 500 to 630 °C for 100 min in total. Similar desorption temperatures to obtain low-coverage Al phases on Si(111) are reported in literature [103, 104]. After every annealing step the surface reconstruction was characterized by LEED. The high annealing temperatures generally lead to more intense and sharper diffraction spots (cf. Fig. 5.2b-d), as shown in Fig. 5.9a. However, the characteristic bright spot of the triangular Al phase is absent, as indicated by a black circle in the close-up sections. The surface at the atomic scale indeed reveals no trace of the triangular phase and only shows the rectangular phase present on large substrate terraces (see Fig. 5.9b). Some traces of the previously described quasi-1D structure were also found. Moreover, the sizes of the patches (black arrows) increase with annealing at such high temperatures, compared to milder annealings before (cf. Fig. 5.6a). This underpins that the Al coverage reduces significantly during the thermal treatment. The triangular phase could exhibit thus a higher coverage than the rectangular phase. A stronger

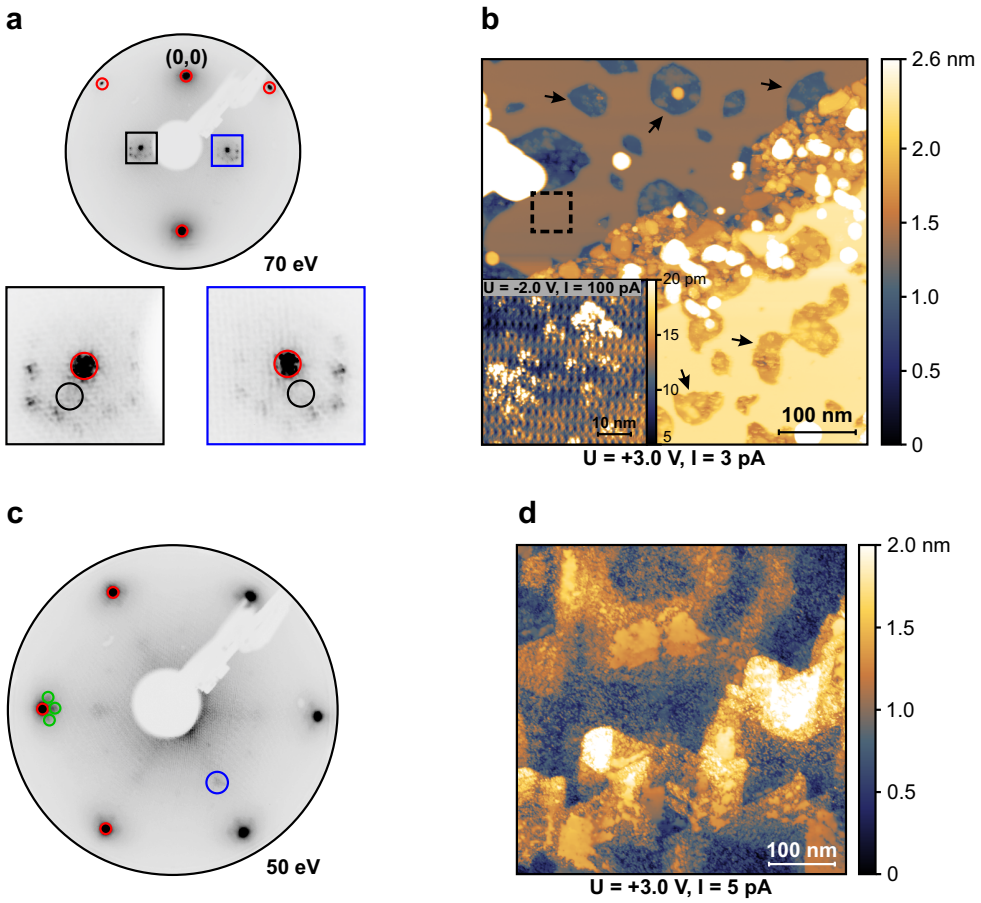

Figure 5.9: Al desorption after annealing – **a**, LEED pattern rotated by approximately 15° of a sample after several annealing steps between 500 and 630 °C. Hexagonally arranged diffraction spots appear around the substrate induced ones (red circles), whereas the characteristic bright spot of the triangular Al phase (black circles) is absent. **b**, In accordance, the STM scan exclusively reveals the rectangular phase on a large scale. The thermal treatment also forms larger holes in the Al film (black arrows) indicative of a significant Al desorption. **c**, Blurred and low in intensity, hexagonally arranged diffraction spots (green circles) after annealing between 630 and 850 °C. Strong thermal treatments result in a highly disordered surface at the atomic scale as confirmed by STM (**d**). No further Al phases in the low-coverage regime are discovered. Also additional, unassignable diffraction spots appear (blue circle).

binding of the Al atoms to the substrate could also be present in the rectangular phase.

With further, successive annealing steps at temperatures between 630 and 850 °C for 80 min, the formerly sharp and relatively intense LEED spots induced by the rectangular Al surface reconstruction drastically start to blur out and lose intensity (see green circles in Fig. 5.9c). New, unassignable diffraction spots emerge, which are marked by a blue circle. In between all these annealing steps the sample was characterized by LEED without any significant change of the diffraction pattern. As already expected from the LEED pattern, the surface at the atomic scale is highly disordered without long-range atomic order (see Fig. 5.9d). These high temperatures ultimately lead to a disintegration of the Al lattice on the SiC surface without forming further Al low-coverage phases. Therefore, the Al buffer layer, i.e., the Al-($\sqrt{3} \times \sqrt{3}$) lattice, could not be experimentally obtained. However, in general, this is not a proof of its non-realizability.

Nevertheless, the absence of any structural evidence may still indicate a thermodynamically unstable lattice in experiment. The Al buffer layer could for example represent a local but not a global energetic minimum in the DFT calculation from Ref. [27]. The LEED pattern in Ref. [27] demonstrated the successful realization of a Al buffer layer on SiC may have also originated from a Si-rich ($\sqrt{3} \times \sqrt{3}$) reconstruction of the SiC substrate [56]. This could have been created during a thermal treatment of the Al/SiC sample.

In summary, various surface reconstructions of a fairly thick and strained Al overlayer on SiC(0001) were first discovered and structurally characterized by LEED and STM. Surprisingly, in contrast to common adlayer systems, the observed surface unit cells of the triangular, rectangular, and quasi-1D Al phase are gigantic. Interestingly, the latter phase shows structural resemblance to the characteristic herringbone reconstruction from Au(111), with which two inequivalent structural models were derived. Both fit to the STM topography in two respective regions well. The formation of the quasi-1D Al phase could likely be the result of an interplay of the Al overlayer and the SiC(0001) substrate with unknown coupling strength and their lattice mismatch. Similar structures are reported for other heterostructure systems of metal adlayers on metallic and semiconductor substrates [96–100]. Therefore, the triangular, rectangular, and the other rarely occurring Al phases can also most likely be a product of the strained Al lattice on SiC(0001).

All derived Al surface unit cells or even structural models in the case of the quasi-1D phase, however, are not fully established. With all the uncertainties in the lattice parameters given by crystalline imperfections and dislocations, other potential surface reconstructions are in principle possible. Furthermore, the STM topography signal depends strongly on the electronic states close to the surface. This could also lead to incorrect interpretations of the lateral atom position within and the dimensions of the unit cells. Since the experimental realization of an Al buffer layer eventually did not match the theoretical predictions, the focus was set to In.

6 In on SiC(0001): Growth and Characterization

In this chapter the structural and spectroscopic characterization of In surface reconstructions in the high coverage regime ($\Theta_{ML} \approx 2 - 3$ ML) are presented. The In-(7×7), -$(6 \times 4\sqrt{3})$, and -$(4\sqrt{3} \times 4\sqrt{3})$ phase exhibit strong metallic character in STS and ARPES. Interestingly, the lowest observed reconstruction forms a triangular In-lattice following the substrate lattice periodicity and surprisingly exhibits linearly dispersing bands at the K points of the Brillouin zone. This eventually leads to the discovery of a novel QSHI, which will be thoroughly analyzed theoretically and experimentally in Chapters 7 and 8. An In buffer layer, however, could not be found in experiment. All data presented here were collaboratively acquired with Jonas Erhardt and are published in Ref. [105].

6.1 Experimental prearrangements and growth process

The In deposition took place in a similar fashion as the Al growth described in the previous chapter (cf. Fig. 5.1). Here, the source material was ultra-pure In droplets (99.9999 % purity), which were evaporated at 770 °C in an effusion cell. To ensure complete hydrogen desorption from the SiC substrate and thus the formation of a large, well-ordered, and defect-free In overlayer, the entire growth process was repeated seven times. During the In enriching process steps of about 5 min, the temperature was held at 250 °C to increase the mobility of In atoms on the surface. As the first goal was to investigate high-coverage phases, In was allowed to accumulate for 60 min during the last growth step.

6.2 Metallic In-(7×7) and -$(6 \times 4\sqrt{3})$ high-coverage phases

Structural characterization with LEED and STM

Subsequent to the growth procedure, the sample was characterized by LEED and STM. The results are depicted in Figure 6.1. The overview STM topography image in Fig. 6.1a reveals wide substrate terraces covered with a uniform In overlayer of high structural quality. Figure 6.1b presents a clear (7×7) surface periodicity with sharp spots and a low degree of incoherent scattering from LEED, in line with the STM image from Fig. 6.1a. The intense spots also indicate a strong atomic scattering potential at the surface. This influences the electronic structure as

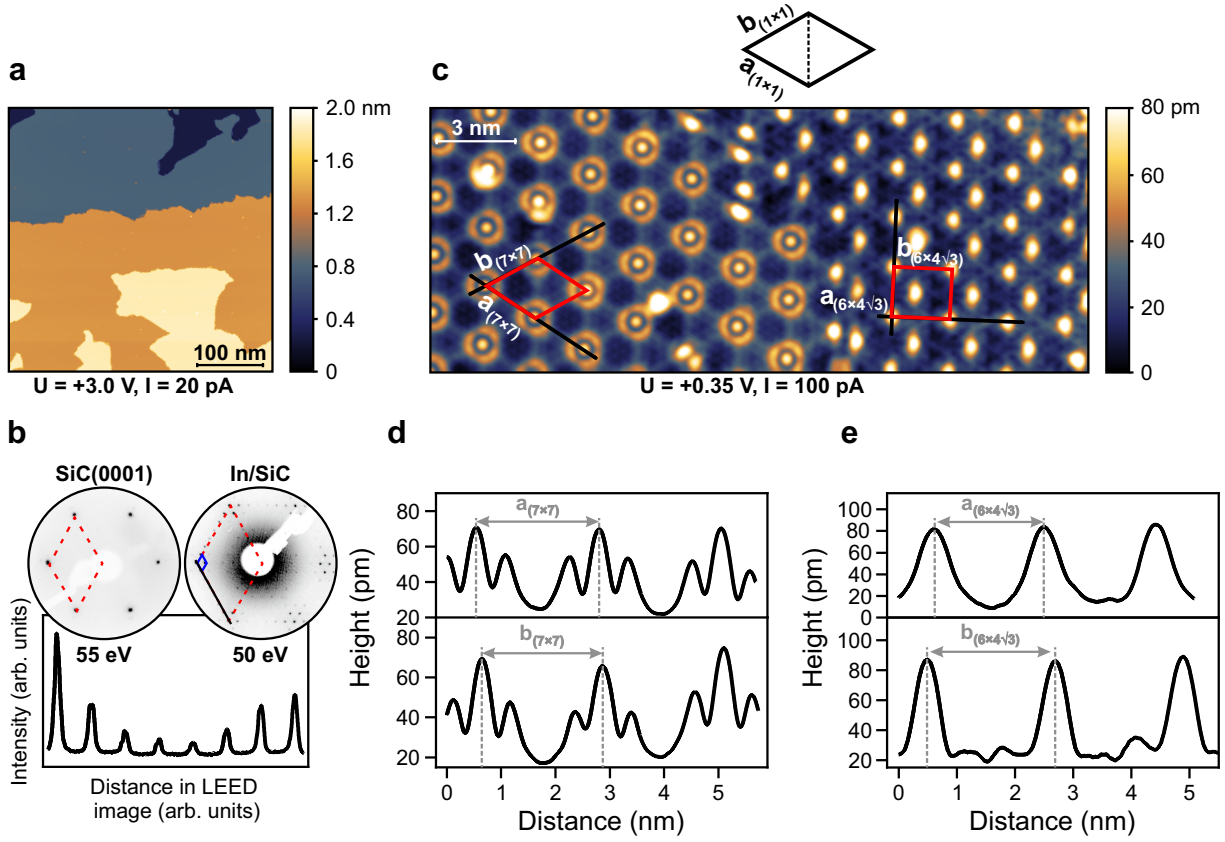

Figure 6.1: In-(7×7) and -$(6 \times 4\sqrt{3})$ lattices characterized by LEED and STM – **a**, The overview constant current STM image after the growth shows large-scale In covered substrate terraces. **b**, The LEED image and the intensity profile along the black line expose a (7×7) diffraction pattern, which is aligned to the substrate surface periodicity. A dashed red and blue rhombus indicate the substrate's and overlayer's unit cell, respectively. **c**, A close-up of the In overlayer shows the two coexisting main surface reconstructions: the (7×7) (left) and $(6 \times 4\sqrt{3})$ (right). For comparison, the substrate unit cell, not drawn to scale, is depicted in black on top of the STM image. **d, e**, Corrugation profiles from **c** demonstrate the sizes of the respective unit cells.

well, which will be demonstrated further below. Both the substrate and the (7×7) unit cell are aligned with each other, as can be seen by the red dashed and blue unit cell.

However, at closer inspection this overlayer consists of two different but coexisting surface reconstructions as depicted in Fig. 6.1c. The height profiles taken along the black lines of both the left and right side are shown in Fig. 6.1d and e, respectively. Lattice constants of $a_{(7\times7)} = (22.52 \pm 0.68)$ Å and $b_{(7\times7)} = (22.27 \pm 0.67)$ Å are found on the left side of the image, both of which are particularly close to seven times the SiC(0001) surface lattice constant. Hence, the (7×7) surface reconstruction, known from LEED, is present on the left half of Fig. 6.1c. The height profiles of the adjacent lattice uncovers lattice constants of $a_{(6\times4\sqrt{3})} = (19.02 \pm 0.57)$ Å and $b_{(6\times4\sqrt{3})} = (21.97 \pm 0.66)$ Å. Here, $a_{(6\times4\sqrt{3})}$ is roughly a factor of six larger than the substrate unit cell, which is depicted in black on top and follows the dashed line of the (1×1) periodicity. This unit cell further highlights the 30° rotation of the $b_{(6\times4\sqrt{3})}$ vector with respect to the two lattice vectors of the In-(7×7) phase. The length of $b_{(6\times4\sqrt{3})}$ must therefore be an integer multiple of $\sqrt{3}$ to be commensurable with the SiC(0001) surface lattice, and is finally determined to be $4\sqrt{3}$.

The unit cell on the right side of Fig. 6.1c therefore becomes $(6 \times 4\sqrt{3}\mathrm{R}30°)$, in the following $(6 \times 4\sqrt{3})$.

A thermal gradient of about 10 to 15 °C along the sample during growth is attributed to the formation of the different In-phases. The gradient also determines the surface ratio between both phases. Depending on the position on the substrate, only one of these surface reconstructions are present on a scale of approximately 50 to 100 nm, as can be seen in Fig. 6.2a, b. The LEED image shown in Fig. 6.1b was therefore taken in a region where predominantly a (7×7) periodicity occurs. However, when the fairly large electron spot ($\sim$ 1 mm in diameter) averages spatially over regions where both the (7×7) and $(6 \times 4\sqrt{3})$ lattices occur on large scales, both phases contribute to the resulting diffraction pattern (see Fig. 6.2c). This is particularly evident when the simulated diffraction pattern of both In surface lattices are superimposed with the LEED image, where the simulated pattern agree well with the characteristic LEED spots of both reconstructions.

Interestingly, the threefold-symmetric substrate surface offers the $(6 \times 4\sqrt{3})$ lattice three different adsorption configurations, each rotated by 120°. A domain wall emerges at the interface of these domains, which is highlighted by white arrows in Fig. 6.2b. On the contrary, the In-(7×7) lattice is not rotated with respect to the substrate leading to a single adsorption configuration and, hence, no domain wall formation. Occasionally, small regions of a (7×7) reconstruction within a $(6 \times 4\sqrt{3})$ matrix are found, marked by a red arrow in Fig. 6.2b.

XPS measurements confirm the high chemical quality of the In overlayer, in which no spectroscopic signatures other than indium and SiC were found (see detailed XPS analysis in Sec. B.1). Moreover, the In coverage was estimated to be roughly 2.9 ML. This places both the (7×7) and

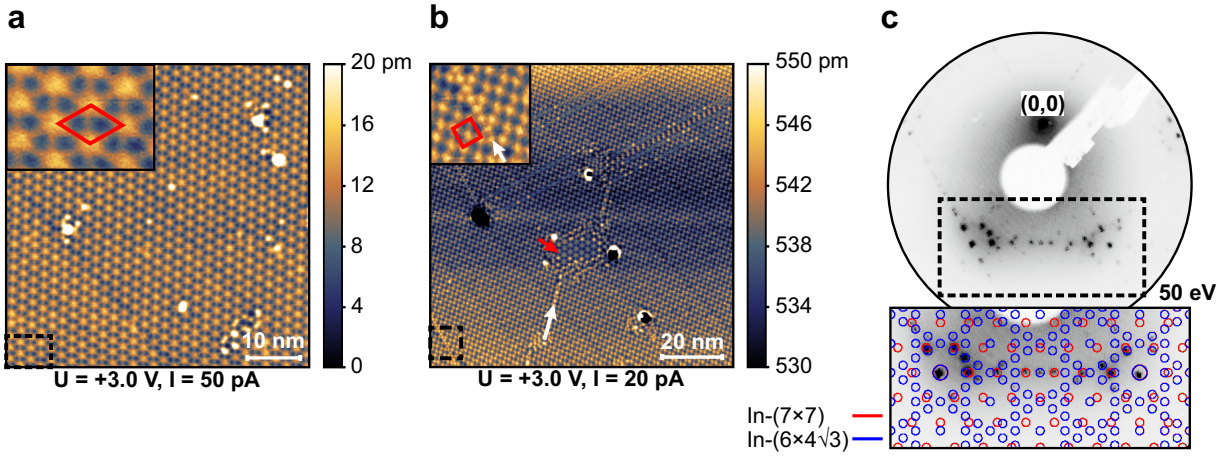

Figure 6.2: Large areas of the In-(7×7) and -$(6 \times 4\sqrt{3})$ phase in STM and LEED – STM constant current scans of In-(7×7) (**a**) and In-$(6 \times 4\sqrt{3})$ (**b**). The respective unit cells are colored in red and overlayed in the insets. White arrows highlight domain walls that form between differently oriented domains of the In-$(6 \times 4\sqrt{3})$ reconstruction. The red arrow marks a small patch of In-(7×7) lattice surrounded by the In-$(6 \times 4\sqrt{3})$ matrix. **c**, LEED image rotated away from the $(0, 0)$ spot of a sample region in which both coexisting reconstructions were present and overlayed with the simulated diffraction pattern. For the simulated pattern, the substrate surface lattice is assumed to have a lattice constant of 3.07 Å [42] and the hexagonal space group $P6_3mc$ [89].

$(6 \times 4\sqrt{3})$ reconstruction in the high-coverage regime, i.e., $\Theta_{ML} > 1$ ML.

Electronic characterization with STS and ARPES

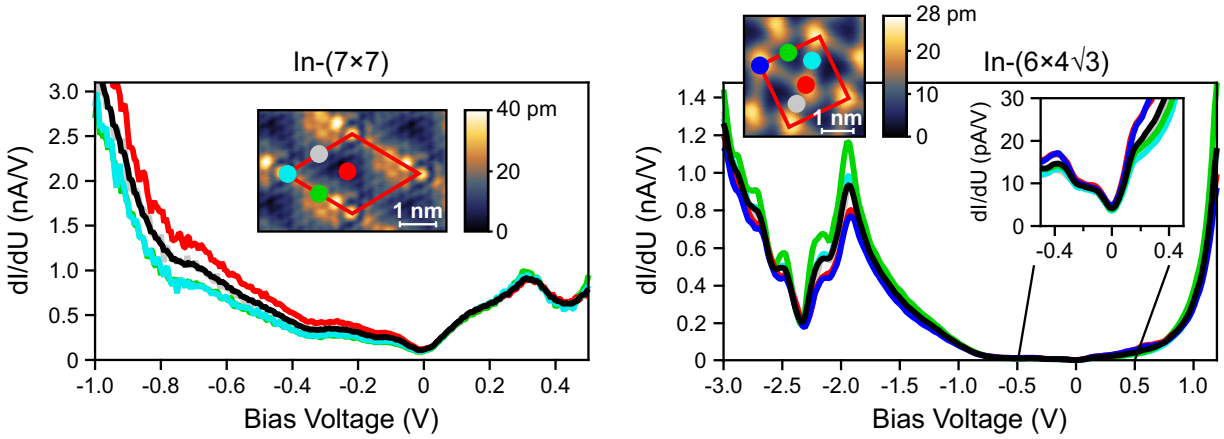

Figure 6.3: Metallic behavior of In-(7×7) and -$(6 \times 4\sqrt{3})$ phases probed by STS – STS $\mathrm{d}I/\mathrm{d}U$ spectra of the In-(7×7) (left) and In-$(6 \times 4\sqrt{3})$ reconstruction (right), respectively. All $\mathrm{d}I/\mathrm{d}U$ curves displayed here are derived numerically from $I(U)$ curves recorded over a grid depicted in the insets. During data acquisition, the feedback loop was switched off at $U = 0.5\,\mathrm{V}$, $I = 300\,\mathrm{pA}$ and $U = 3.0\,\mathrm{V}$, $I = 100\,\mathrm{pA}$, respectively. The modulation voltage of the lock-in amplifier was set to $U_{rms} = 20\,\mathrm{mV}$. Spatially resolved spectra within the unit cells (depicted in red) were averaged over several equivalent positions. The black $\mathrm{d}I/\mathrm{d}U$ curves were averaged over several unit cells.

To get a better understanding of the electronic properties of both In high-coverage phases, STS measurements were conducted with the results illustrated in Figure 6.3. Both phases show strong metallic behavior since close to the Fermi level, i.e., at zero bias voltage, the differential conductance and thus the LDOS is finite, which is characteristic for metallic systems. Interestingly, all STS spectra taken at different positions within the (7×7) and $(6 \times 4\sqrt{3})$ unit cell differ slightly quantitatively but follow the same curve qualitatively. Discrepancies might be due to a spatially varying tunneling transmission coefficient. The STS signal colored in black was averaged over several unit cells and serves here as a guide to the eye.

Since both In high-coverage phases were present on large scales with high structural quality (cf. Fig. 6.1a and Fig. 6.2a,b), the sample was qualified to be investigated further by ARPES, with the results illustrated in Figure 6.4. Several bands cutting through the Fermi level are clearly evident, which render those In phases metallic, in agreement with the results from STS. Other In high-coverage phases on Si(111) also show strong metallic character in STS and ARPES [107–109]. The characteristic substrate valence bands of SiC(0001) are present at approximately 2 eV below the Fermi energy at and around the Γ-point as shown in Fig. 6.4a [50, 106, 110]. Interestingly, all bands primarily follow the SiC(0001)-(1×1) substrate periodicity (see path in reciprocal space in Fig. 6.4c). From this observation, however, a slight deviation occurs that is described further below.

Ultra-thin layers of gallium (Ga) (2 to 3 ML thick) and In (2 ML thick) intercalated to the graphene/SiC(0001) interface reveal a similar band situation that upon first inspection closely

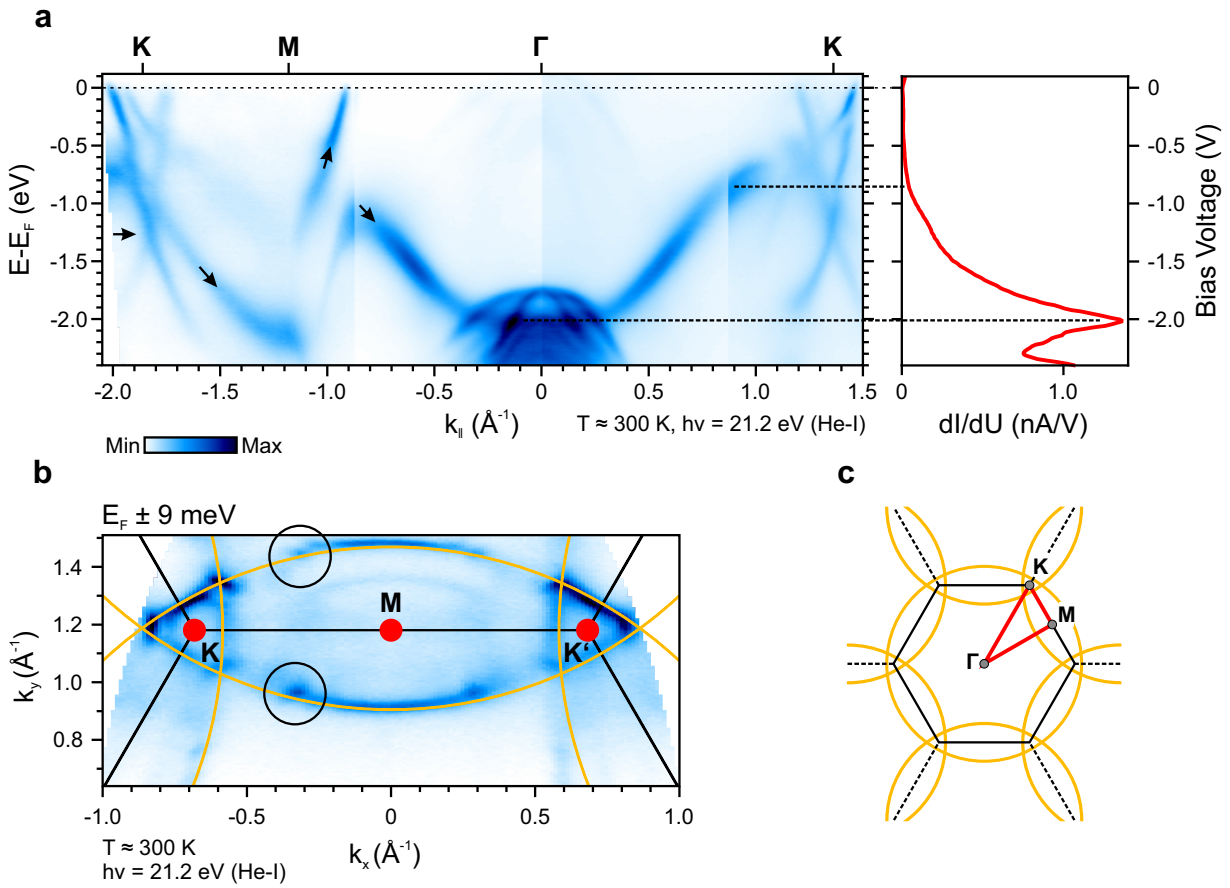

Figure 6.4: Metallic band structure of the In-(7 × 7) and -(6 × 4√3) phases characterized by ARPES and STS – **a**, Comparison between the ARPES band map along $\overline{KM\Gamma K}$ (path in reciprocal space illustrated in **c**) and the spatially averaged $\mathrm{d}I/\mathrm{d}U$ signal from the In-(7 × 7) phase. The black arrows highlight pronounced band features to compare the ARPES outcome with the literature results in Ref. [106]. **b**, Constant energy contour (CEC) at the Fermi level. The electron pockets from the first and higher Brillouin zones, overlapping at the K/K' points, are traced in orange and are further schematically illustrated in **c**. Discrepancies between the data and the orange lines are attributed to a small misalignment during tilt scans. Black circles in **b** highlight discontinuities in the band arcs between K and K' and originate in electron Umklapp processes at the In-(7 × 7) surface periodicity. Faint satellite bands close to the Fermi level around Γ originate from the unmonochromatized He lamp. The STS spectrum was recorded with the feedback loop switched off and stabilized at $U = 3.0\,\mathrm{V}$ and $I = 100\,\mathrm{pA}$ and is averaged over several (7 × 7) unit cells.

resembles qualitatively the one in Figure 6.4a and b [106]. In particular, pronounced band characteristics of the 2D-Ga and -In layer can also be found in the ARPES data of the high-coverage In phases (highlighted with black arrows) discussed here. Among others, the intense band dispersing across the entire Brillouin zone from the M-point over Γ to K agrees well with the literature. Also, a steep dispersing band crossing the Fermi level close the M points can be clearly identified. It can therefore be concluded that all additional bands, in particular the ones close to the Fermi level, must be In-induced. Additionally, the XPS analysis for the In-(7 × 7) and -(6 × 4√3) reconstruction suggests a coverage that is close to the ultra-thin In and Ga films (see Sec. B.1 for more information). On the example of graphene intercalated with a 2D Ga film, Briggs *et al.* attributed the large s-orbital band Fermi velocity to the small lateral distance

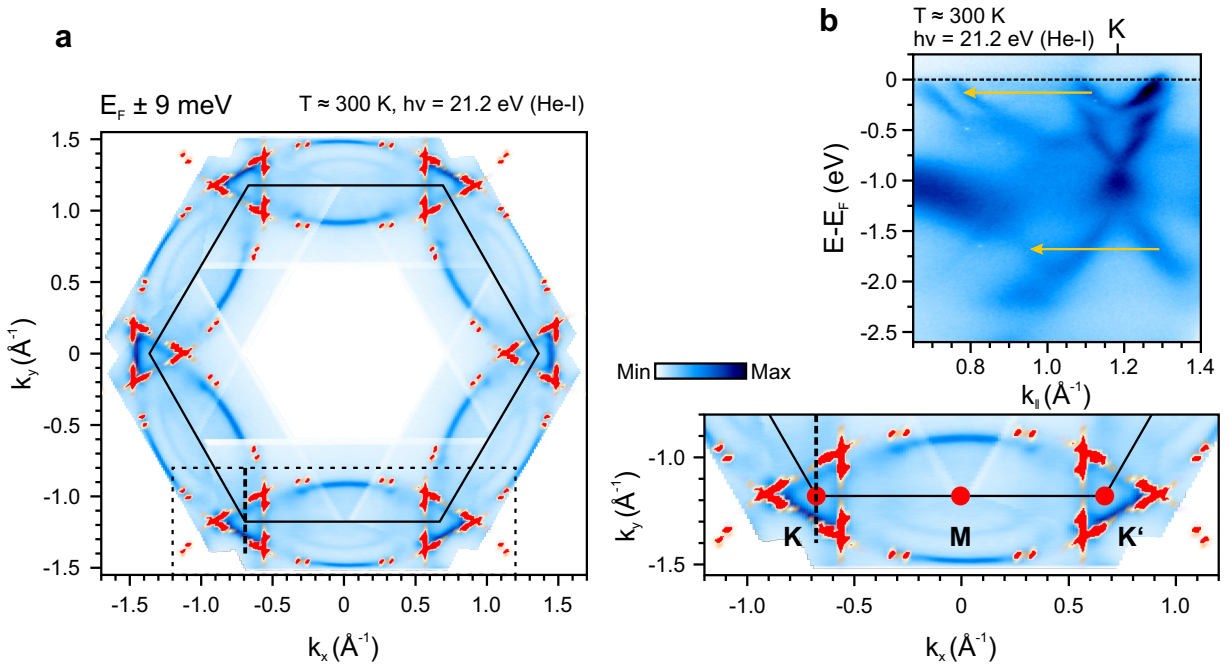

Figure 6.5: Scattering of electrons on the In-(7×7) unit cell – **a**, Sixfold rotated CEC at the Fermi level from Fig. 6.4b defines the SiC(0001)-(1×1) Brillouin zone (black line). A simulated Fermi surface map in red is overlayed and agrees well with the experimental data set (see text for simulation details). **b**, Band map taken along the black dashed line in **a** demonstrates replicated bands shifted by a (7×7) unit cell vector in reciprocal space (orange arrows).

between the Ga atoms with a considerably high valence electron filling in the p-shell [106]. A Fermi velocity of almost as high as in bulk Al or Ga arises [106]. Electronic states in the low-energy sector can therefore essentially be described within the nearly free-electron model [106]. Due to the strong resemblance with these films, it is plausible that the In-(7×7) and -$(6 \times 4\sqrt{3})$ reconstructions also follow this model. Similar cases are known to occur from Pb adlayers on Si(111) [111].

The intense In-band cutting through the Fermi level in $\overline{\Gamma M}$ direction in Fig. 6.4a translates in the Fermi surface map to an electron pocket originating in the next higher Brillouin zone (see orange highlighted Fermi arcs in Fig. 6.4b). The same applies to the next higher Brillouin zones, which are partially occupied by electron pockets from the first Brillouin zone. The overall band situation close to the boundary of the first Brillouin zone is schematically illustrated in Fig. 6.4c.

Upon further inspection, the Fermi surface of the electron pockets reveal some discontinuities. In particular, between K and K', the arcs seem to be interrupted as highlighted by black circles in Fig. 6.4b. This indicates electron scattering on the strong (7×7) surface potential, which also affects the LEED pattern (see Fig. 6.1b). In order to reveal and highlight this scattering effect, a CEC was simulated and overlayed. The simulation features non-shifted electron pockets from the first and adjacent Brillouin zones that are convoluted with pockets shifted by a (7×7) reciprocal unit cell vector. This accounts for a first order scattering process of electrons on the In-(7×7) reconstruction. All points of intersection between those shifted electron pockets and

the initial electron pockets are represented in red. The CEC was then defined as a cut at a specific energy through a parabolically dispersing band. As depicted in Fig. 6.5a, the simulated CEC agrees well with the one from ARPES. Furthermore, the energy cut along the black dashed line clearly reveals replicated bands from the K-point that are shifted by a (7×7) unit cell vector (orange arrows) in reciprocal space. Hence the strong periodic atomic potential of the (7×7) reconstruction promotes a scattering of electrons. However, signatures of an Umklapp process induced by the In-$(6 \times 4\sqrt{3})$ reconstruction are not resolved. Either, the atomic potential on which electrons scatter is too weak or the amount of the In-$(6 \times 4\sqrt{3})$ phase on the surface is negligible compared to the In-(7×7) lattice.

Comparing the spatially averaged $\mathrm{d}I/\mathrm{d}U$ signal of the (7×7) reconstruction with the ARPES band structure yields a good agreement. In particular, the LDOS onset at approximately $-0.8\,\mathrm{V}$ and the distinct peak at roughly $-2\,\mathrm{V}$ correspond clearly to In-induced bands, as indicated by black dashed lines in Fig. 6.4a. Both features represent key signatures for In high-coverage phases in ARPES and STS and are also reported for other In phases presented below. The intense STS peak can be attributed to the high tunneling probability of electrons occupying the fairly low dispersing In-band close to Γ. Additionally, the In-induced band along $\overline{KM}$ and the band crossing at a binding energy of approximately 1.3 eV at K/K' are characteristic components of the ARPES signal as well (see black arrows in Fig. 6.4a). The key properties identified here are also reported for graphene intercalated with 2D-Ga and -In layers [106].

6.3 Metallic In-$(4\sqrt{3} \times 4\sqrt{3})$ surface reconstruction

Structural characterization with LEED and STM

Motivated by the search of low coverage phases, i.e., the buffer layer, the sample was successively annealed at a temperature of 480 °C for 5 min each. After several cycles, a new In-induced surface reconstruction of high structural quality emerged as illustrated in Figure 6.6a, b. Similar desorption temperatures are known from high-coverage In films on Si(111) [107–109]. The lattice parameters are $a_{(4\sqrt{3}\times4\sqrt{3})} = (20.35 \pm 0.61)\,\text{Å}$ and $b_{(4\sqrt{3}\times4\sqrt{3})} = (19.63 \pm 0.59)\,\text{Å}$, respectively and are derived from the STM height profiles shown in Fig. 6.6c. The discrepancy between $a_{(4\sqrt{3}\times4\sqrt{3})}$ and $b_{(4\sqrt{3}\times4\sqrt{3})}$ might originate from the fast and low scanning speed direction of the STM tip. Since both values are close to a factor of $4\sqrt{3}$ of the SiC(0001) surface lattice constant, this phase is a commensurable In-$(4\sqrt{3} \times 4\sqrt{3})$ surface reconstruction. Like for the $(6 \times 4\sqrt{3}\mathrm{R}30°)$ lattice described above, the unit cell here is also rotated by 30° with respect to the underlying substrate, which is visible particularly well in Fig. 6.8a. This characterizes an In-$(4\sqrt{3} \times 4\sqrt{3}\mathrm{R}30°)$ reconstruction.

Interestingly, the STM topography results shown in Fig. 6.6a and b reveal a kagome-like lattice structure. In general, kagome lattices are *per se* rich on exotic physical phenomena based on topology and correlations [112–115]. However, a characteristic spectroscopic signature, i.e., a flat band state, was found neither in ARPES nor in STS (see Fig. 6.7a, b). Based on these results,

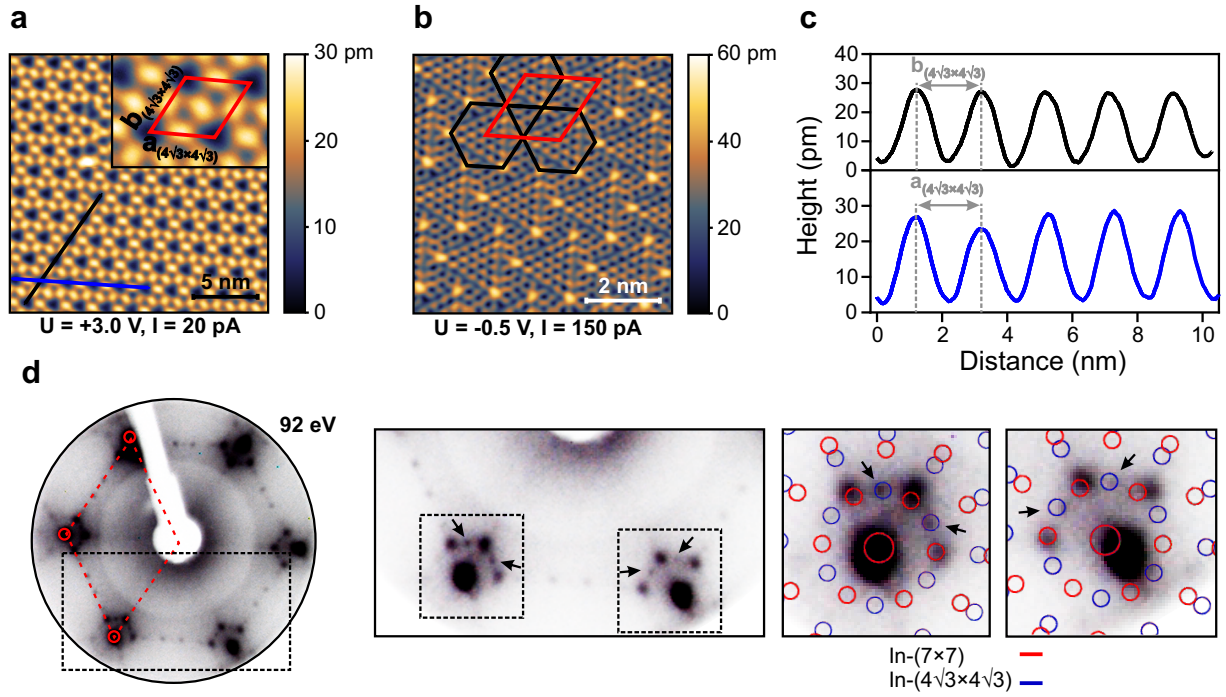

Figure 6.6: In-$(4\sqrt{3}\times 4\sqrt{3})$ surface lattice characterized by STM and LEED – **a**, STM constant current image of an In-induced $(4\sqrt{3}\times 4\sqrt{3})$ lattice. The height profiles are taken along the black and blue line, respectively and are depicted in **c**. The unit cell with its side lengths is illustrated in red in the inset. **b**, STM constant current image clearly shows the kagome-like appearance of this In-lattice, which is highlighted exemplarily by a black kagome lattice. The $(4\sqrt{3}\times 4\sqrt{3})$ unit cell in red is overlayed. **d**, The experimental LEED pattern comprises of a superposition of the In-(7×7) and -$(4\sqrt{3}\times 4\sqrt{3})$ reconstruction. Additional diffraction spots are highlighted by black arrows and are characteristic for the $(4\sqrt{3}\times 4\sqrt{3})$ lattice, which can be confirmed after the simulated diffraction patterns of both In phases are overlayed. For the simulated pattern, the substrate surface lattice is assumed to have a lattice constant of 3.07 Å [42] and the hexagonal space group $P6_3mc$ [89]. The LEED image was recorded by Judith Gabel, Pardeep K. Thakur, and Tien-Lin Lee [I09, Diamond Light Source (UK)].

the realization of true kagome physics in the In-$(4\sqrt{3}\times 4\sqrt{3})$ lattice can be excluded.

A temperature gradient during annealing also defines the occupation ratio of different In phases on the surface. The large electron spot allows for spatial averaging over a macroscopic sample area. Figure 6.6d reveals therefore a superposition of the In-(7×7) and -$(4\sqrt{3}\times 4\sqrt{3})$ lattice diffraction. However, the characteristic but low-intense spots of the $(4\sqrt{3}\times 4\sqrt{3})$ phase (see black arrows in Fig. 6.6d) suggest a rather low surface occupation in this case.

Figure 6.8a shows the In-$(4\sqrt{3}\times 4\sqrt{3})$ reconstruction bordering a low In coverage phase in STM. Here, the corrugation profile across both of the In-phases depicts a height difference of approximately (56.3 ± 5.6) pm (see Fig. 6.8b). In addition, the coverage was estimated from XPS to be roughly 1.9 ML, which places this phase in the high-coverage regime as well (see Sec. B.1 for a detailed coverage analysis). With these facts at hand, a second In layer on top of the low In coverage phase, seen in the left part of Fig. 6.8a, can be hypothesized. However, the exact adsorption configuration and arrangement of the In-atoms within this second layer remains elusive. A trimer-like arrangement of In atoms could be in the realm of possibility as, for instance, was predicted in the case of In on Si(111) [116].

Electronic characterization with STS and ARPES

To obtain a complementary picture of the electronic properties in real and reciprocal space, the In-$(4\sqrt{3} \times 4\sqrt{3})$ structure was investigated by STS and ARPES. The results are combined in Figure 6.7. Like the previously discussed In high-coverage phases, the In-$(4\sqrt{3}\times4\sqrt{3})$ reconstruc-

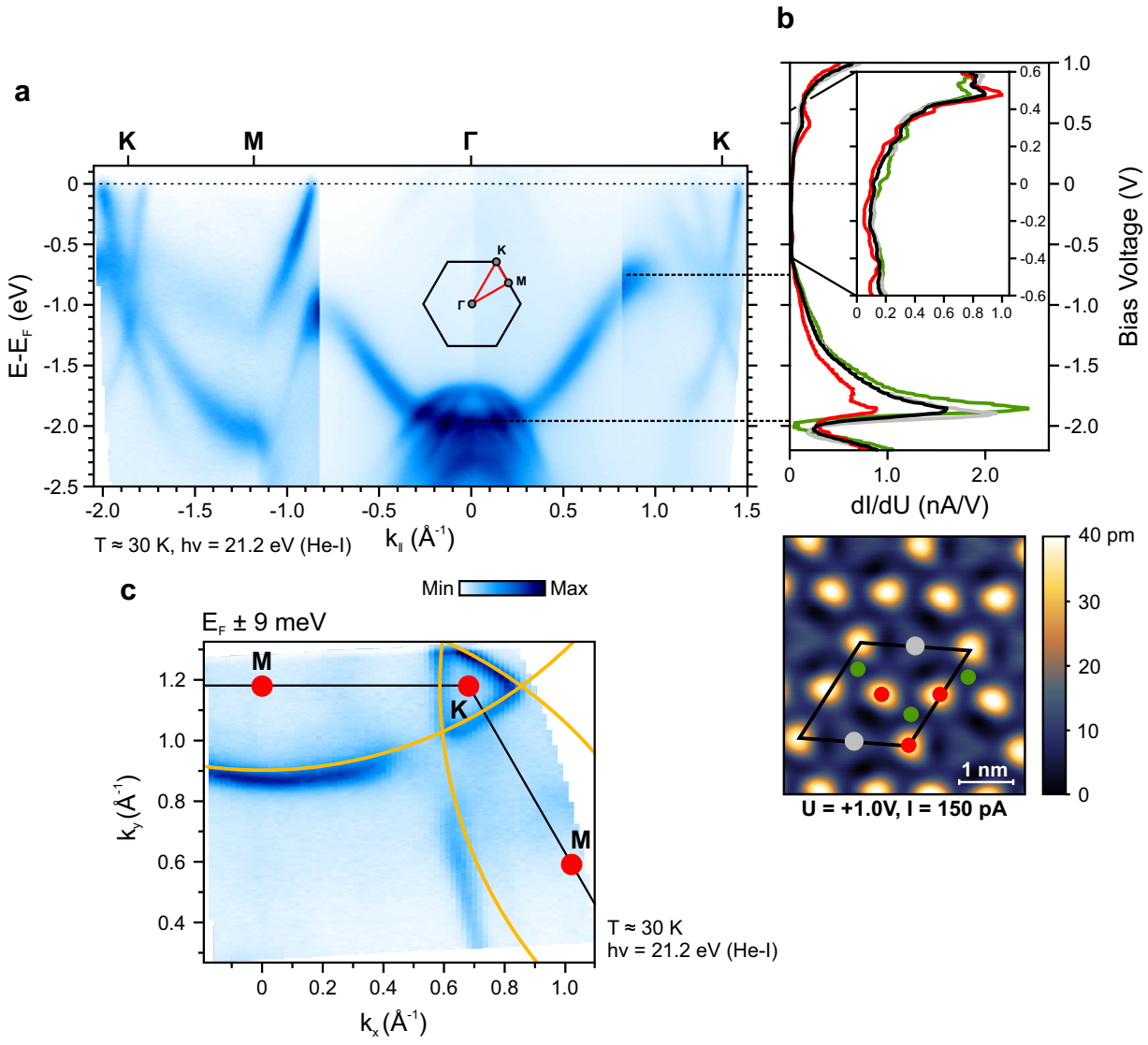

Figure 6.7: Metallic band structure of the In-$(4\sqrt{3} \times 4\sqrt{3})$ phase probed by ARPES and STS – **a**, ARPES band structure along $\overline{KM\Gamma K}$ compared with STS spectra (**b**). The STS spectra was taken from a grid shown in the underlying constant current STM image. The faint bands around Γ close to the Fermi level are due to satellites of the unmonochromatized He-lamp. **b**, $\mathrm{d}I/\mathrm{d}U$ curves displayed here were averaged over the positions schematically shown in the STM image and were differentiated numerically from $I(U)$ curves recorded with an lock-in amplifier. During STS data acquisition the feedback loop was switched off and the tunneling tip was stabilized at $U = 1.0\,\mathrm{V}$, $I = 150\,\mathrm{pA}$ and $U = 0.6\,\mathrm{V}$, $I = 250\,\mathrm{pA}$ (inset), respectively. The modulation voltage of the lock-in amplifier was set to $U_{rms} = 10\,\mathrm{mV}$ and $U_{rms} = 7\,\mathrm{mV}$ (inset), respectively. Due to electronic noise a binning procedure over three adjacent data points was applied to all $\mathrm{d}I/\mathrm{d}U$ curves displayed in the inset. **c**, CEC at the Fermi energy shows electron pockets (orange lines) from different Brillouin zones overlapping at K. Discrepancies between the data and the orange lines are attributed to a small misalignment during tilt scans.

tion also shows electronic states at the Fermi level in STS and ARPES, which proves its metallic behavior (see Fig. 6.7a-c). In addition, the STS spectra taken at different positions within the unit cell vary only slightly quantitatively but qualitatively follow the same signal curve, as can be seen in Fig. 6.7b. The black line represents $\mathrm{d}I/\mathrm{d}U$ curves averaged over several unit cells and serves as a guide to the eye.

The ARPES band structure and Fermi surface in Fig. 6.7a, c resembles to a great extent the one from the In-(7×7) and In-$(6 \times 4\sqrt{3})$ reconstruction described above. Electron pockets of the first and second Brillouin zones meet here at the K/K' points and form a triangular-like contour in addition to the pronounced band arcs around the M points (cf. Fig. 6.4b, c). In general, all hallmark features of the other In high-coverage phases in ARPES can be found here as well. Even the characteristic peak in the $\mathrm{d}I/\mathrm{d}U$ signal closely located to $-2\,\mathrm{V}$ corresponds to the weakly dispersing In-band near Γ in ARPES that overlaps with the valence bands of the substrate (see black dashed line in Fig. 6.7a, b). Another kink in the $\mathrm{d}I/\mathrm{d}U$ curve can be further associated with the distinct In-band maximum in $\overline{\Gamma K}$ direction.

In contrast to the previously described In high-coverage phases, no discontinuities due to Umklapp processes were observed in the Fermi surface and band map from ARPES (see Fig. 6.7a, c). This suggests that the atomic potential of the In-$(4\sqrt{3} \times 4\sqrt{3})$ reconstruction is too weak to enable electron scattering on it. The bands, therefore, only follow the SiC(0001)-(1×1) periodicity.

6.4 The In-(1×1) low coverage phase – In atoms in a triangular lattice

Upon further annealings, another new In reconstruction emerged. The characterization results from STM and ARPES are presented in Figure 6.8. Interestingly, the In atoms are arranged here in a triangular lattice with an in-plane distance identical to the SiC(0001) substrate, which renders this phase an In-(1×1) reconstruction (see Fig. 6.8a, b).

Such a sample with a mixture of the In-$(4\sqrt{3} \times 4\sqrt{3})$ and In-(1×1) phases was investigated by ARPES. On top of the reproduced In-$(4\sqrt{3} \times 4\sqrt{3})$ bands, a faint but distinct band structure is clearly visible (see red arrow in Fig. 6.8c), which is significantly different from the well-known insulating SiC band structure [48, 50]. Therefore, this band structure must originate from the In-(1×1) reconstruction. Surprisingly, quasi-linearly dispersing bands appear near the Fermi level at K/K' (see red circles in Fig. 6.8c, d). Because of its similarity to the graphene band structure, this In phase is interesting for exhibiting Dirac fermions. Also, the small height difference of $(56.3 \pm 5.6)\,\mathrm{pm}$ depicted in Fig. 6.8b suggests a thinner In film with a coverage close to 1 ML.

Further annealing showed that this In phase has the lowest coverage observed. Most of the lattice order deteriorate drastically and leave only small patches where an In-(1×1) reconstruction was present (see Fig. 6.8e). Therefore, like the previously investigated Al phases, an In-buffer layer could not be observed experimentally. Also in this case, generally speaking, this does

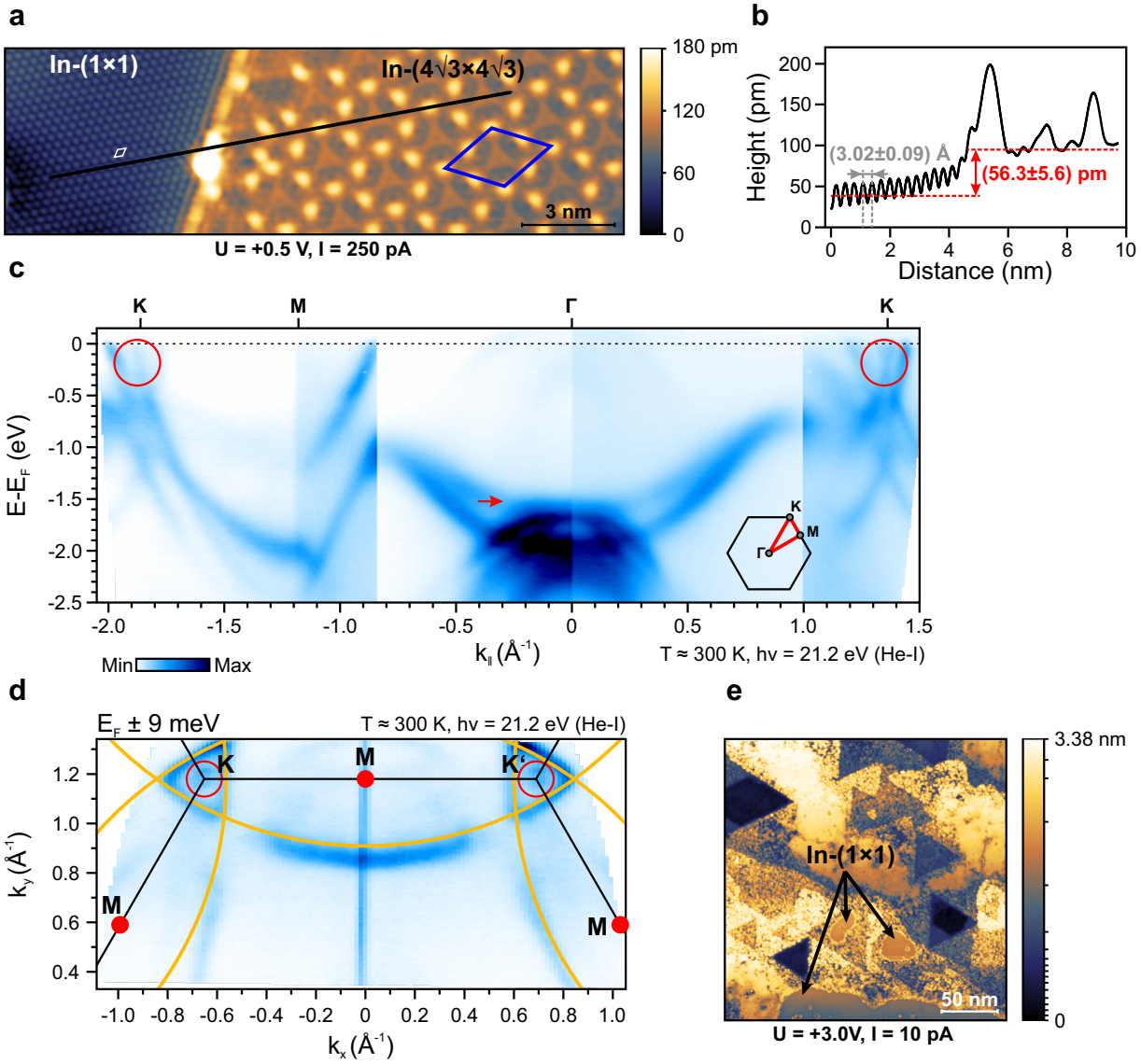

Figure 6.8: Characterization of the lowest In coverage phase by STM and ARPES – **a**, Interface of a In-(1×1) and In-$(4\sqrt{3} \times 4\sqrt{3})$ phase in STM topography with a height profile presented in **b**. The (1×1) and $(4\sqrt{3} \times 4\sqrt{3})$ unit cells are depicted in white and blue, respectively. A rotation angle of 30° between both unit cells is evident. **b**, The in-plane lattice distance underpins the (1×1) periodicity. **c, d**, ARPES band map along $\overline{KM\Gamma K}$ (path in reciprocal space illustrated in the small schematic) and CEC at the Fermi level, respectively. The unmonochromatized He-lamp produces faint satellite bands close to the Fermi level around Γ. The red arrow and circles in **c** and **d** indicate ARPES signatures of the In-(1×1) reconstruction. Orange lines in **d** mark the electron pockets of the first and higher Brillouin zones. Discrepancies between the data and the orange lines are attributed to a small misalignment during tilt scans. **e**, Long annealing steps lead to small patches of the In-(1×1) phase being surrounded by a disordered surface that renders it the phase with the lowest observed In coverage.

not prove the non-realizability of an In-buffer layer on SiC(0001). Nevertheless, the absence of any structural evidence may still indicate a thermodynamically unstable structure in experiment.

In summary, for the In films presented here, a passivation layer as predicted by theory (see Sec. 2.3) could also not be realized. Thicker In films ($\Theta_{ML} \approx 2.9$ and ≈ 1.9 ML) with a surface

reconstruction of (7×7), $(6 \times 4\sqrt{3})$, and $(4\sqrt{3} \times 4\sqrt{3})$ exhibit strong metallic behavior, in which electrons can be described within the nearly-free electron model. The lowest observed coverage reveals a triangular In lattice following the substrate's periodicity. Surprisingly, this reconstruction features a quasi-linear band dispersion at K/K', well-known from 2D hexagonal lattices, such as graphene (cf. Chap. 2). This eventually will lead to the discovery of a novel QSHI, which will be thoroughly analyzed theoretically and experimentally in Chapters 7 and 8.

7 Emergent Dirac fermions in a two-dimensional triangular lattice

The quasi-linear bands at K/K' observed for the lowest In coverage phase in the previous chapter sparks an in-depth theoretical examination of this triangular lattice, which is the scope of this chapter. The emergence of a hidden electronic honeycomb network within a triangular lattice after chiral orbitals are placed on the triangular lattice sites is a key result. In the SOC-dominating case, massive Dirac fermions at K/K' emerge, which characterizes a QSHI. All discussed effects condense in an indium monolayer on SiC(0001) – *indenene*, for which a theoretical low-energy model based on DFT is provided. Importantly, a novel approach to identify the non-trivial character in indenene by a distinct charge localization sequence will be presented. The theoretical elaboration presented here was conducted in a collaborative work by Eck *et al.* and is published in Ref. [117].

7.1 From honeycomb to triangular lattices

Hexagonal lattice systems are well-known for exhibiting non-trivial Dirac properties (see Chapter 2). Aside from graphene, a prominent candidate is bismuthene on SiC(0001). Honeycombs made of the high-Z element bismuth (Bi) are covalently bound to the substrate, which promotes large on-site SOC and renders it a high-temperature QSHI candidate [118]. In general, however, heavy elements tend to form triangular instead of hexagonal surface lattices when deposited on hexagonal substrates (see Sec. C.1 for a literature overview). Those surface lattices are known for their astonishing physical properties that range, for instance, from topological and unconventional superconductivity to spin liquids [119–123]. An interesting question that now arises is: Can triangular lattices also host a quantum spin Hall insulating phase [124]?

In a joint study, Eck *et al.* theoretically derived an emergent electronic honeycomb connectivity when in-plane chiral orbitals are arranged in a 2D triangular lattice [117]. Hence, Dirac physics, known from 2D hexagonal lattices, occur within a triangular network, which potentially opens a new route to realize novel QSHIs.

7.1.1 Hidden honeycomb network within a triangular lattice

Structurally, both the honeycomb as well as the triangular lattice are closely related and share the same space group. But, as illustrated in Figure 7.1a, the main structural difference is the

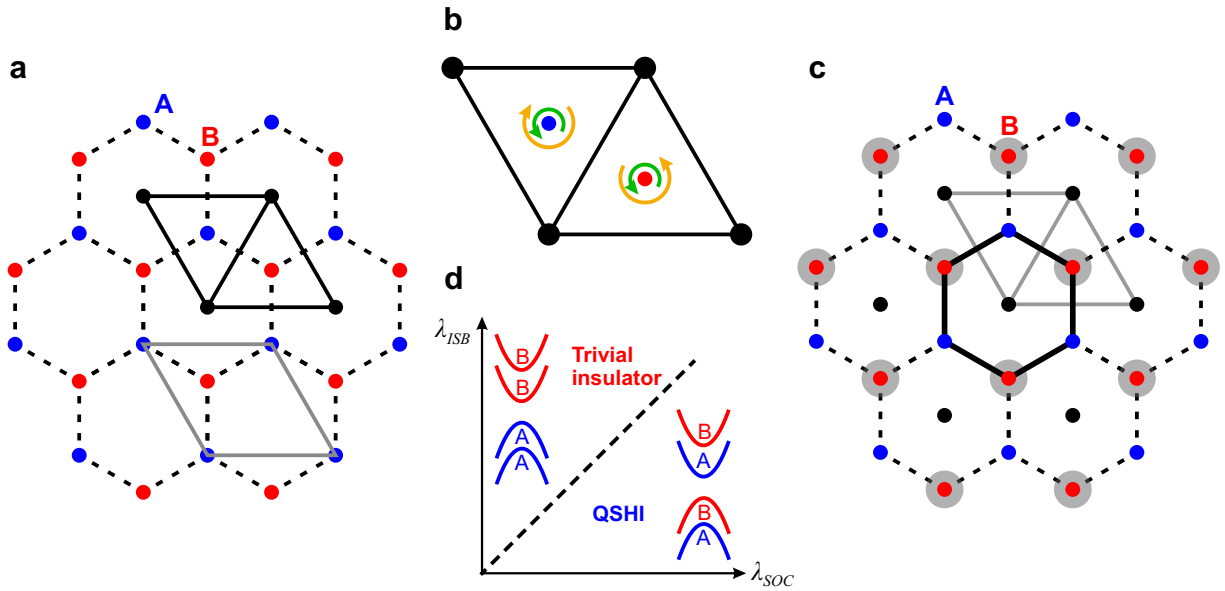

Figure 7.1: Emergent honeycomb connectivity in a triangular lattice – **a**, Hexagonal lattice (black dashed hexagon) with a bipartite atomic basis (blue (A) and red circles (B)) including the unit cell in gray. The triangular lattice unit cell (black solid line) with monopartite basis (black circles) is overlayed. **b**, Lattice (orange arrow) and orbital Bloch phase (green arrow) accumulated by electrons in this triangular network. This leads to a charge localization at A/B, i.e., the center of the voids in the triangular unit cell (**c**), yielding an effective honeycomb configuration (thick solid black line in **c**). The triangular lattice sites with the unit cell (gray line) are overlayed. An in-plane inversion symmetry breaking (ISB) render the sublattices inequivalent (large gray circles). **d**, Schematic low-energy band structure situation at K/K' in the trivial and non-trivial case with a distinct energy-dependent charge localization sequence. λ_{ISB} and λ_{SOC} represent the strength of the ISB and on-site SOC. Figure in **a** after [117]. Figure in **b** and **d** were adapted from [117] and [110], respectively.

bipartite hexagonal lattice, where atoms reside on the A and B positions (see blue and red circles, respectively). This is directly evident from the additional atomic position within the gray unit cell (red circle) that span the hexagonal lattice depicted by dashed black honeycombs. In contrast to that, atoms in a triangular lattice are located on one site only (see black circles), which renders it monopartite. The triangular unit cell is depicted as a black line and overlayed with the honeycomb lattice. Note, the two sublattice sites of the honeycomb coincide with the voids in both halves of the triangular unit cell. The band structures in both lattice types differ substantially. In the 2D Brillouin zone at K and K', however, the Bloch eigenvalues of both lattices are identical based on their shared symmetry. In the following, a more precise understanding of how an electronic honeycomb network within a triangular lattice emerges is given by a single Bloch wave function of momentum $\boldsymbol{k}$:

$$\Psi_{\boldsymbol{k}}(\boldsymbol{r}) = \langle \boldsymbol{r}|\Psi_{\boldsymbol{k}}\rangle = \sum_{\boldsymbol{R}} e^{i\boldsymbol{k}\boldsymbol{R}} \langle \boldsymbol{r}|w_{\boldsymbol{R}}\rangle \,. \tag{7.1}$$

In Equation 7.1 $w_{\boldsymbol{R}}$ represents a local chiral orbital situated on a triangular lattice site in the unit cell defined by the corresponding lattice vector $\boldsymbol{R}$. Special interest is now given to the phases that this Bloch wave function accumulates within this network, as illustrated in the unit cell in Fig. 7.1b. Upon hopping between nearest-neighboring sites, the electronic wave function collects

a *lattice phase factor* of $\omega = e^{\pm i\frac{2\pi}{3}}$ at K/K', which reflects the threefold symmetric lattice and is depicted as an orange arrow. Additionally, while doing that, electrons gain an *orbital phase factor* indicated by a green arrow. The lattice phase factor here leads to a valley-dependent Bloch orbital angular momentum characterized by an eigenstate $Y^{latt}_{K/K'}$ with a magnetic quantum number of $m^{latt} = \pm 1$. As the chiral orbitals themselves are eigenstates of the angular momentum operator $\hat{L}$, their angular contribution to the total Bloch phase is described by a spherical harmonic $Y^{orb}(\boldsymbol{R})$ with a magnetic quantum number m^{orb}. Both phases discussed here contribute to the total valley-dependent Bloch wave function $\Psi_{K/K'}$ (cf. Eq. 7.1) at the triangular lattice sites, which at the void positions becomes, i.e. at $\boldsymbol{r} = \{A, B\}$ (blue and red circles in Fig. 7.1a-c, respectively):

$$\begin{aligned}\langle \boldsymbol{r} = \{A,B\}|\Psi_{K/K'}\rangle &\propto \sum_{\boldsymbol{R}} \langle \boldsymbol{r}|Y^{latt}_{K/K'}(\boldsymbol{R})\cdot Y^{orb}(\boldsymbol{R})\rangle \\ &\propto \sum_{n=0}^{2} [\omega^{m^{latt}}\cdot\omega^{m^{orb}}]^n \\ &= 3\delta_{(m^{latt}+m^{orb})\bmod 3,0} = 3\delta_{m^{tot}\bmod 3,0}\,.\end{aligned} \tag{7.2}$$

The total angular momentum m^{tot} described in Equation 7.2 imposes electronic charges from K/K' to localize in real space at A/B. However, localization can only occur in the case of a constructive interference between the participating local wave functions weighted by the Bloch phase. This takes place, in particular, only when the total angular momentum follows the C_3 symmetry of the K/K' points in reciprocal space, or in other words, when m^{tot} is a multiple of three. The square of the total valley-dependent wave function at the void positions define the real-space localization and with the given argument renders to:

$$|\Psi_{K/K'}(\boldsymbol{r} = \{A,B\})|^2 \begin{cases} > 0, \text{ if } m^{tot} \bmod 3 = 0 \\ = 0, \text{ if } m^{tot} \bmod 3 \neq 0\,. \end{cases} \tag{7.3}$$

In conclusion, chiral orbitals with a suitable set of Bloch phases satisfying the formal conditions derived in Eqs. 7.2 and 7.3 and placed on triangular lattice sites induce a real space charge localization in the center of both unit cell halves. These positions simultaneously coincide with the atomic positions of a honeycomb lattice (see Fig. 7.1a-c). Thus, a *hidden honeycomb connectivity* defined by an electronic charge localization emerges, as highlighted with a black hexagon in Fig. 7.1c. Interestingly, this effective honeycomb network is completely decoupled from a physical honeycomb lattice arranged by atoms. A specific example is given with the chiral orbitals of $p_\pm = (p_x \pm ip_y)/\sqrt{2}$ that results in a localization of p_+ (p_-) at B (A) and A (B) at K and K', respectively. In the following, the competing impacts of on-site SOC and in-plane ISB on the low-energy spectrum is elaborated.

7.1.2 Local spin-orbit interaction and in-plane inversion symmetry breaking

Again, by restricting the investigation to K/K', group theory identifies the symmetry at both valley momenta as D_{3h} [117, 125]. Assuming a $p_\pm$ basis, this implies two doubly degenerate states at this momenta, i.e., at the Dirac points. The on-site SOC introduced with the Hamiltonian:

$$\hat{H}^{SOC} = \lambda_{SOC} \vec{\hat{L}} \cdot \vec{\hat{S}} = \lambda_{SOC} \hat{L}_z \otimes \hat{S}_z \,, \tag{7.4}$$

lifts this degeneracy and creates a twofold degenerate valence and conduction band. In Equation 7.4 λ_{SOC}, $\hat{L}_z$, and $\hat{S}_z$ represent the strength of the SOC and the z-component of the orbital and spin angular moment operator, respectively. The opened band gap is of topologically non-trivial nature. However, by considering an in-plane ISB that renders the A and B sublattice inequivalent, as depicted by gray circles in Fig. 7.1c, the symmetry gets further reduced to C_{3h} [117, 126]. In this case, each of the former doubly degenerate valence and conduction states split up into two single, spin-polarized bands, respectively. The impact of the ISB can be expressed with its Hamiltonian as:

$$\hat{H}^{ISB}(K/K') = \pm \lambda_{ISB} \hat{L}_z \,, \tag{7.5}$$

where λ_{ISB} represents the strength of the ISB. In Equation 7.5 it is directly evident that the in-plane ISB causes orbital angular momentum (OAM) polarization along the surface normal. The chiral $p_\pm$ orbitals considered above, for example, are OAM eigenfunctions and posses opposite L_z eigenvalues. This characterizes the valence and conduction bands at K/K'. The full Hamiltonian taking both the SOC as well as the in-plane ISB effect at K/K' into account, reads as follows:

$$\begin{aligned} \hat{H}(K/K') &= \hat{H}^{SOC} + \hat{H}^{ISB}(K/K') \\ &= \hat{L}_z \otimes \left(\lambda_{SOC} \hat{S}_z \pm \lambda_{ISB} \hat{S}_0 \right) . \end{aligned} \tag{7.6}$$

As the origin of the ISB is a staggered sublattice potential (see Fig. 7.1c), the ISB-induced splitting is topologically trivial. Therefore, a competition between the relative strength of the SOC and ISB effect dictates the band gap size, its non-trivial nature, and also the charge localization in real space (see Fig. 7.1d). Generally, to determine the topology of a system robustly the analysis needs to be expanded over the entire Brillouin zone. At K/K', for example, this can result in a topologically trivial band gap in the large λ_{ISB} limit. In this case, the charge from the valence and conduction band localizes on one of the sublattices A or B only, respectively. On the other side, in the large λ_{SOC} limit the triangular lattice represents a QSHI and valence and conduction electrons localize on both sublattice sites A and B, respectively. It is important to note that in the latter case each valence and conduction band contribute to only one single sublattice, respectively (see Fig. 7.1d). This is implied by the C_3 symmetry argument from Eq. 7.3. Figure 7.1d summarizes the results in a schematic way. The charge localization sequence is strongly connected to the topology in this triangular lattice and allows for the trivial and non-trivial case to be distinguished.

In the following, it will be shown that an In monolayer hosting triangularly arranged in-plane chiral p orbitals form this hidden honeycomb network. Further, the impact of a homogeneous substrate, and later the SiC(0001) surface, on the low-energy spectrum is presented in a pedagogical way. This results in the theoretically predicted model of *indenene*. All results shown in the following are adapted from the publication by Bauernfeind *et al.* [110].

7.2 Theoretical low-energy model of *indenene* on SiC(0001)

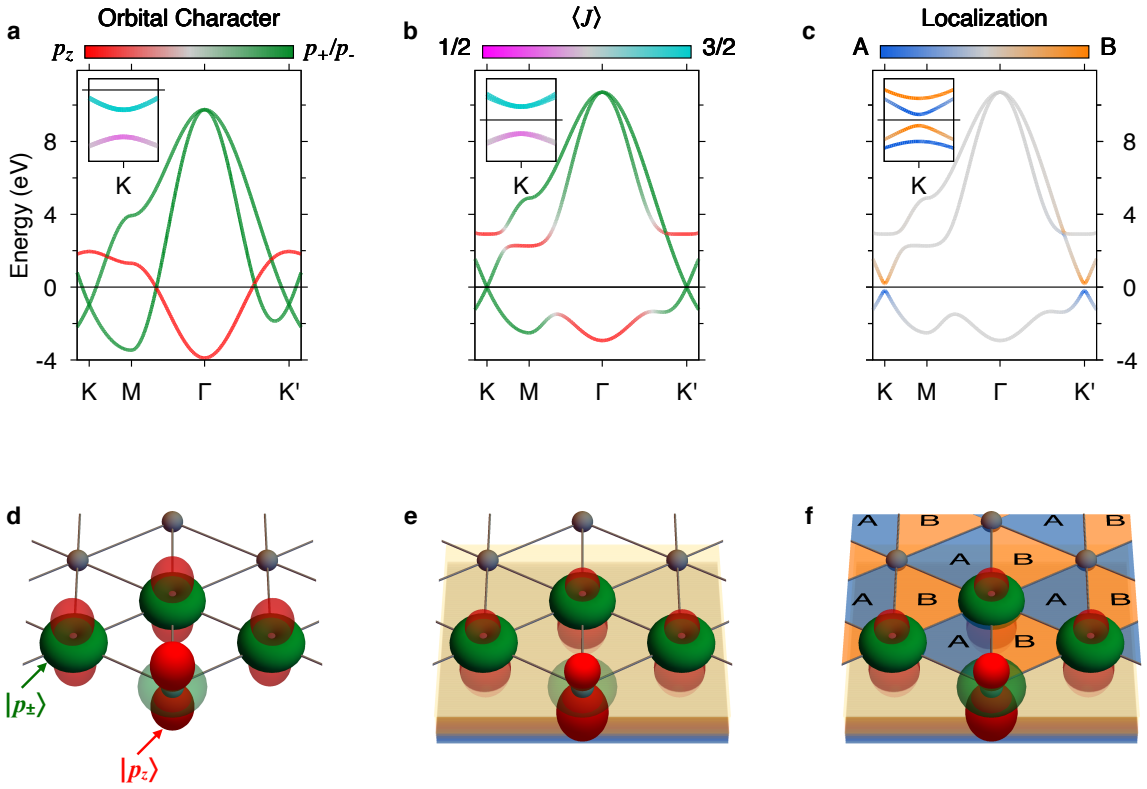

Figure 7.2: Low-energy indenene model in the tight binding picture – **a-c**, Band structures for a p_+, p_-, p_z basis arranged in a triangular network depicted without (with) considering SOC in the main panels (insets) and corresponding structural models (**d-f**). **a, d**, Metallic band structure with linearly dispersing bands at K/K' promoted by the orthogonality of p_z and in-plane p orbitals. Considering SOC results in split valence and conduction bands with $J = 1/2$ and $3/2$ character, respectively. **b, e**, The broken mirror symmetry after introducing a homogeneous substrate yields hybridization gaps between bands with in- and out-of-plane p-orbital character. A quantum spin Hall insulating ground state is realized after including SOC. **c, f**, Indenene on SiC(0001). Additionally, the substrate surface breaks the in-plane inversion symmetry (ISB) and renders the A (blue) and B (orange) side of the triangular unit cell inequivalent. Without SOC, in the topologically trivial phase, charges of the valence and conduction band at K/K' localize solely on the A and B side, respectively. Considering SOC leads to a non-trivial scenario with spin-split Dirac bands. The charges of the valence and conduction states from K/K' condense in this case on both sides of the indenene unit cell. This distinctive charge localization pattern is identical for both K points. Taken from [110].

The theoretical results are summarized and presented in Figure 7.2. The triangular lattice

model is based on three spherical harmonics of In $5p$ orbitals:

$$\left\{ p_{\pm} = \frac{1}{\sqrt{2}}(p_x \pm i p_y), p_z \right\}. \tag{7.7}$$

A linear combination of in-plane p orbitals form a torus-like structure. Both, the in- and out-of-plane p orbitals are depicted in Fig. 7.2 in green and red, respectively. In the freestanding case the triangular lattice has a symmetry of D_{6h}, which yields in the tight-binding picture a Dirac crossing of the $p_{\pm}$-induced bands at K/K'. Also, the $p_{\pm}$ and p_z orbitals are orthogonal to each other and form a metallic band structure (see Fig. 7.2a, d). Considering now local, i.e. atomic, SOC, as discussed above, opens a band gap at K/K' and split the degenerate bands into $J = 3/2$ and $1/2$ states (see inset of Fig. 7.2a).

In general, a substrate underneath the In layer must be considered if this 2D layer is to be synthesized. The presence of a homogeneous substrate here breaks the mirror symmetry along the surface normal (see Fig. 7.2e). This leads to a coupling between the in- and out-of-plane orbital components and, thus, to hybridization gaps, as can be seen in Fig. 7.2b. In addition, atomic SOC splits the spin-degeneracy and renders a quantum spin Hall insulating ground state (see inset of Fig. 7.2b). States with mixed $p_{\pm}$ and p_z orbital contributions undergo a Rashba-like splitting, whereas the low-energy states at K/K' are protected by the C_{6v} symmetry imposed by the In-atoms in the triangular lattice.

By considering now 4H-SiC(0001) as a specific substrate with an atomic surface corrugation, further reduces the symmetry to C_{3v}. Here, the C atom of the uppermost SiC bilayer breaks the in-plane inversion symmetry and renders both halves of the unit cell inequivalent, as schematically illustrated in Fig. 7.2f (see Fig. 7.4a and another schematic representation in Fig. 7.1c). The ISB effect promotes a global band gap and under the consideration of SOC splits the valence and conduction bands into two singly degenerate pairs, respectively (see inset of Fig. 7.2c). As elaborated above, at this stage the SOC and ISB term compete with each other. In the topologically non-trival case, i.e. when $\lambda_{SOC} > \lambda_{ISB}$, electrons of single valence (conduction) bands at K/K' localize either on the A or B side of the triangular unit cell, as depicted in the inset of Fig. 7.2c. Therefore, this allows for the trivial and non-trivial band configuration at K/K' to be distinguished.

Moreover, as discussed above the in-plane ISB induces a OAM polarization in the Dirac bands. This is illustrated with band structures of indenene in the topologically trivial and non-trivial case in Figure 7.3. Without SOC the valence and conduction band at K and K' exhibit opposite L_z eigenvalues, respectively (see Fig. 7.3a). By introducing weak SOC, i.e. $\lambda_{SOC} < \lambda_{ISB}$, the trivial band configuration persists. However, boosting SOC pushes indenene into the non-trivial regime and produces a OAM polarization that is distinctly different from the trivial phase. Within the split valence and conduction bands at K/K' the L_z eigenvalues change sign (see Fig. 7.3c). Probing this unique, energy-dependent OAM polarization sequence allows for the topological character to be classified. An ARPES experiment with circular polarized light is a

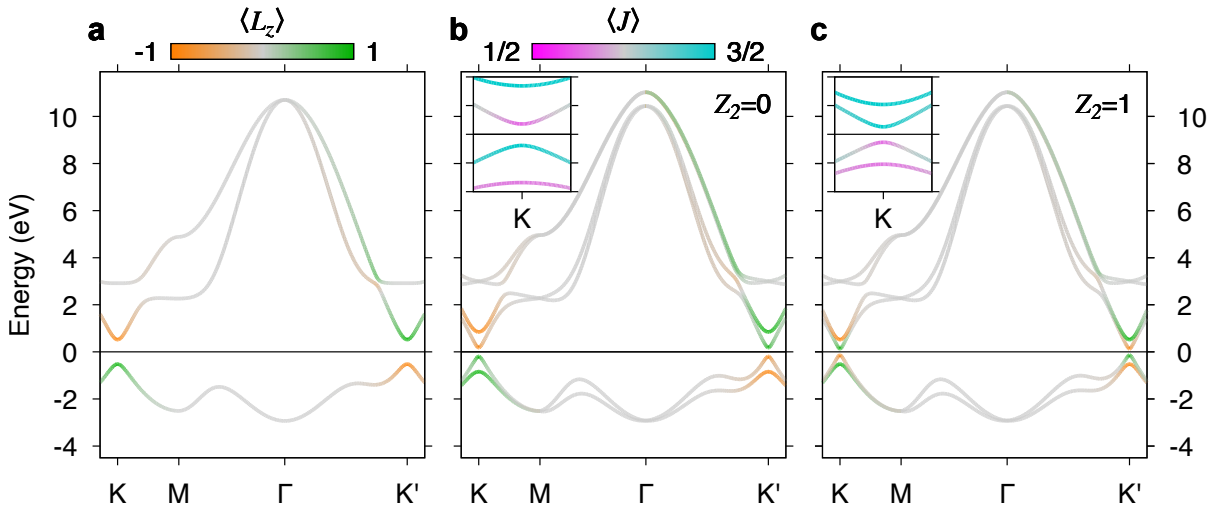

Figure 7.3: Connection between OAM and topology in indenene – Topologically trivial band structures without/with SOC (**a**/**b**) but with $\lambda_{ISB} = 0.2$. **c**, Non-trivial band structure with SOC and $\lambda_{ISB} = 0.075$. The OAM polarization in the non-trivial case differs distinctly from the trivial case, which allows a direct classification of the topology of this system. Taken from the supplemental material of [110].

potential approach to access this OAM at K/K' [127–129]. With this method a characteristic OAM texture of the Weyl semimetal TaAs was revealed and allowed the identification of its non-trivial topology [130].

In the theoretically predicted structural model of indenene, every Si atom of the uppermost SiC bilayer is covalently bonded to an In atom (T1 site), which results in a In-(1×1) reconstruction (see Fig. 7.4a, b). The T1 adsorption site is confirmed by a detailed DFT study (for more information see Sec. C.2). The full band structure including the 4H-SiC(0001) substrate with SOC calculated by DFT with a Heyd–Scuseria–Ernzerhof (HSE)06 exchange-correlation functional is presented in Fig. 7.4c. All bands in the low-energy sector are of In p character with the exception of the substrate-related bands at $-1.5\,\text{eV}$ and below around the center of the Brillouin zone. In particular, the split Dirac bands at K/K' originate from indium in-plane p orbitals. At energies of approximately $0.5\,\text{eV}$, the bands mostly possess In p_z character, which will become important later in the localization of In atoms in STM. Overall, this band structure reproduces the bands predicted in the tight-binding model presented above. In particular, DFT reveals a fundamental band gap of size $E_{gap,\,DFT} = 70\,\text{meV}$ at K/K'.

Interestingly, like in the case of stanene on a buffer layer (see Sec. 2.3) the topological nature of the indium monolayer depends strongly on the distance d to the underlying substrate (see Fig. 7.4b). The DFT results for non-relaxed, i.e. fixed, bond lengths show that the staggered potential induced by the ISB renders indenene topologically trivial at small distances ($d < d^{crit}$), whereas at large distances ($d > d^{crit}$) the non-trivial properties survive. The equilibrium distance derived from DFT is with $d^{DFT} = 2.68\,\text{Å}$ sufficiently larger than the critical distance of $d^{crit} = 2.57\,\text{Å}$. Thus, fully relaxed indenene is placed by DFT in the non-trivial regime.

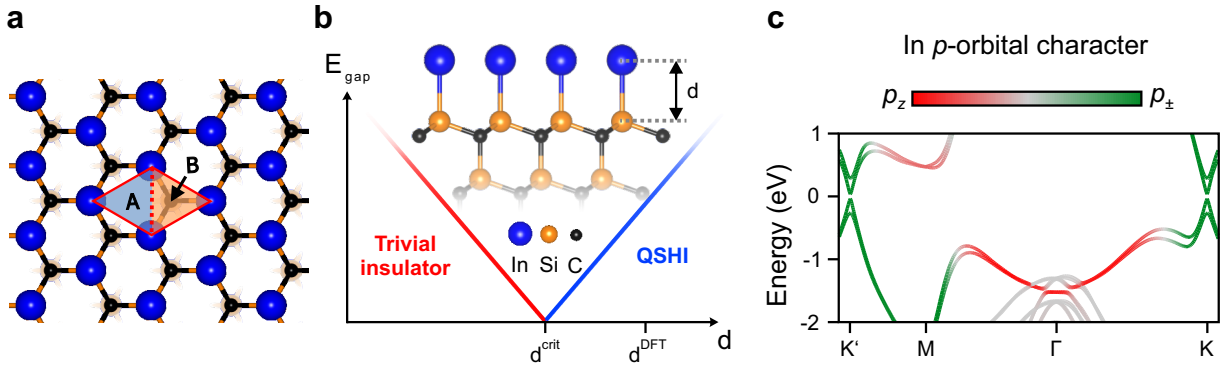

Figure 7.4: Structural model and band structure of indenene – **a, b**, Monolayer of In-atoms adsorbed to the uppermost Si-atoms (T1 position) of the SiC(0001) substrate form a (1×1) surface reconstruction. Due to the C-atom of the substrate an in-plane ISB is introduced and renders the left (A) and right (B) half of the triangular unit cell inequivalent. **b**, ISB strength influences the non-trivial character of indenene and depends on the bonding distance d between the indenene layer and SiC. A topological phase transition occurs at a critical distance of $d^{crit} = 2.57\,\text{Å}$ accompanied by a gap closure at K/K'. The equilibrium distance of the relaxed structure derived from DFT is $d^{DFT} = 2.68\,\text{Å}$ which, thus, defines indenene as a QSHI. **c**, DFT calculated band structure with HSE06 exchange correlation functional of fully relaxed indenene on 4H-SiC(0001) including SOC. The Bloch wave functions are projected on In s, p and SiC sp^3 bases. Figure in **a** and **b** were adapted from [110]. Figure in **c** was adapted from the supplemental material of [110].

In summary, an electronic honeycomb network emerges when in-plane chiral orbitals are placed on triangular lattice sites, which results in Dirac fermions at K/K'. The driving force behind the formation of the honeycomb network is the constructive interference of Bloch wave functions in the voids of the triangular lattice. In-plane ISB and atomic SOC compete with each other, form the band gap size, and dictate the topology of this system. The SOC-dominated case results in a non-trivial ground state with massive Dirac fermions. A distinct charge localization pattern within the triangular unit cell is a key signature of this system. A possible realization of this scenario would be achieved by in-plane p orbitals. Based on these results a monolayer of indium atoms adsorbed to SiC(0001) – *indenene* – is predicted to host a quantum spin Hall insulating phase. However, not only the in-plane p orbitals have a key role here, but also their substrate-induced hybridization with the out-of-plane p_z-orbital, for example, ultimately leads to a global band gap. In addition to the distinct charge localization pattern, the Dirac bands at K/K' exhibit a unique OAM polarization that also allow for a clear identification of the topological character. The theoretical prediction given here is explored experimentally in the following chapter.

8 Indenene on SiC(0001) – Dirac fermions in a triangular In lattice

The scope of this chapter is to present the experimental realization of indenene on 4H-SiC(0001), which was theoretically introduced in the previous chapter. A thorough spectroscopic analysis by ARPES confirms massive Dirac fermions at K/K'. XSW measurements further determine the bonding distance to the substrate and give a first indication of the non-trivial topology in indenene. The detection of an alternating charge localization sequence within the triangular unit cell by STS identifies indenene unambiguously as a QSHI. Apart from XSW, all data presented here were collaboratively acquired with Jonas Erhardt. The results depicted in this chapter are adapted from the publication by Bauernfeind *et al.* [110].

8.1 Structural analysis

8.1.1 Large-scale growth of indenene

In order to directly access and identify the proposed effects in indenene, the In monolayer was epitaxially grown as a single phase on the 4H-SiC(0001) substrate. A first structural characterization after growth by STM reveals In-covered substrate terraces on a length scale of several hundred nanometers, as can be seen in Fig. 8.1a. The red and black height profiles show that these terraces are vertically separated by a single (1 nm) and a half (0.5 nm) 4H-SiC(0001) unit cell, respectively (see Fig. 8.1b). Inspecting this In film on smaller length scales reveals the highly ordered triangular indenene lattice with bright defects occasionally appearing (see Fig. 8.1c, d). The impact of these defects on the local electronic structure in their vicinity will be discussed further below in Sec. 8.2.2.

8.1.2 Indenene – A In-(1×1) surface reconstruction

The structure and symmetry of indenene was further inspected by STM and LEED with the results presented in Figure 8.2. A small topography section imaged by STM with a bias voltage of $U = 1.5\,\mathrm{V}$ is shown in Fig. 8.2a. At this high bias voltage, the p_z-orbital contribution of the In atoms is primarily probed (cf. Fig. 7.4c). This allows for the bright protrusions in Fig. 8.2a to be linked directly to the atomic position of the In atoms on the surface. Moreover, the structural model from DFT (cf. Fig. 7.4a) can now be arranged correctly on the topography data yielding

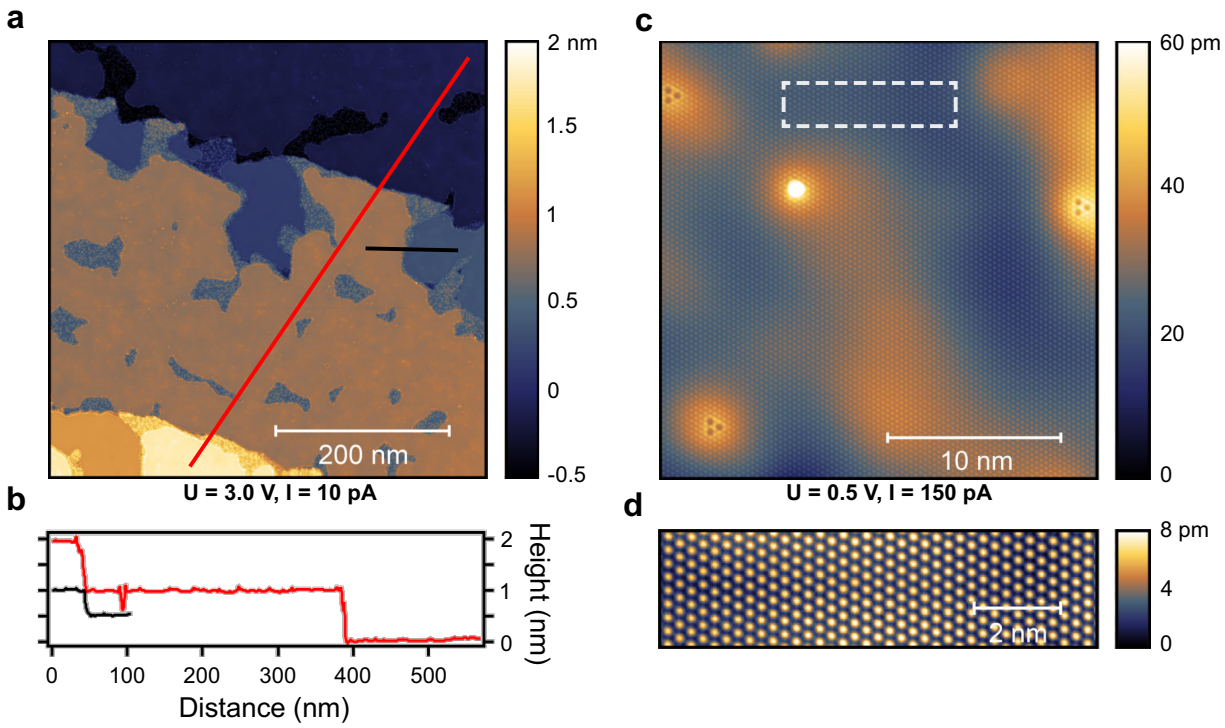

Figure 8.1: Topographic imaging of indenene on large scales in STM – **a**, Large-scale STM topography image (500 nm × 500 nm) of indenene covered SiC. The black and red corrugation profiles are depicted in **b** and reveal half (0.5 nm) and full (1 nm) 4H-SiC(0001) unit cell steps separating the indenene film. **c, d**, Both close-ups demonstrate a highly-ordered triangular indenene lattice on a scale of 10 nm interrupted by occasionally occurring defects altering the local electronic structure (see Sec. 8.2.2 for more information). Adapted from the supplemental material of [110].

a great accordance. Further STM measurements confirm the T1 adsorption position of the In atoms (see Sec. C.2 for more information). This lattice structure translates to a (1×1) surface periodicity, as demonstrated by the LEED image in Fig. 8.2b. The red rhombus depicts the substrate surface unit cell. Indicative for such a surface reconstruction is the identical in-plane lattice constant as the substrate. The red and gray height profiles from Figs. 8.2a and d, depicted in Fig. 8.2c, indeed prove this relationship. The orange corrugation profile further highlights the inequivalence between the A and B half of the unit cell introduced by the C atom of the first bilayer of the substrate.

An indenene layer next to the uncovered SiC substrate, as shown in Fig. 8.2d, highlights the structural equivalence between both triangular lattices appearing in STM. However, their electronic properties unveiled in the differential conductivity curve differ significantly, as shown in Fig. 8.2e. Here, indenene exhibits pronounced electronic states within the wide band gap of SiC [49].

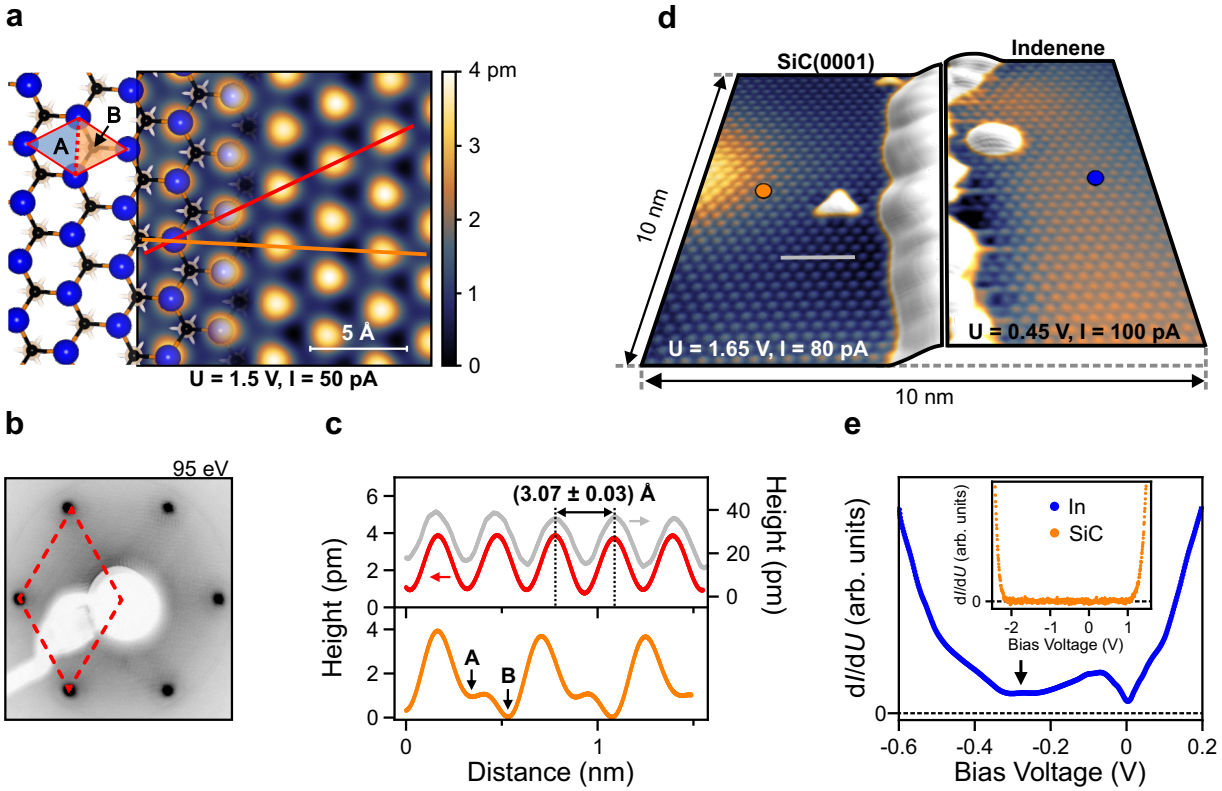

Figure 8.2: Structural and spectroscopic characterization of indenene by LEED, STM, and STS – **a**, STM topography image of indenene overlayed with the structural model from DFT. This lattice configuration yields a (1×1) surface reconstruction confirmed in LEED (**b**). **c**, The orange corrugation profile demonstrates the structural inequivalence between the A and B side of the indenene unit cell induced by the C atom of the topmost SiC bilayer. **d**, A film edge showing uncovered SiC next to the indenene layer illustrates their identical lattice structures, which is further confirmed by the gray and red height profile in **c**. Electronically, however, they differ significantly as shown by the $\mathrm{d}I/\mathrm{d}U$ spectra (**e**) measured on either side of the edge in **d**. The tip stabilization and lock-in parameters for the indenene and SiC STS spectrum were $U = -600\,\mathrm{mV}$, $I = 500\,\mathrm{pA}$, $U_{mod} = 10\,\mathrm{mV}$ and $U = 1.75\,\mathrm{V}$, $I = 70\,\mathrm{pA}$, $U_{mod} = 20\,\mathrm{mV}$, respectively. The conductance minimum indicated by the black arrow is attributed to the Dirac point. Figures in **a, c-e** were taken from [110]. Figure in **b** was adapted from the supplemental material of [110].

8.2 Massive Dirac fermions in indenene mapped by ARPES

Figure 8.3a shows, in addition to the experimental ARPES data, the theoretically predicted band dispersion of the fully relaxed indenene-substrate combination from DFT (red curve; cf. Fig. 7.4c). It is directly evident that the experimental and theoretical dispersion agree well. The theoretical energy scale was adapted here to the experimental one. In the process, the DFT bands were shifted by approximately 250 meV towards higher binding energies to account for the large electronic charge transfer induced by the strong n-doped SiC substrate (see Sec. 8.2.1 for more information). This rigid band shift allows for the band gap to be probed directly in ARPES. However, before a detailed gap-fitting procedure is employed, a first indication of the presence of this energy gap can be seen in the inset of Fig. 8.3a, depicting a close-up of the bands around the K-point. Highlighted by white lines, the quasi-linear dispersing valence and conduction bands are clearly not connected. Figure 8.3b depicts the K-point band dispersion on a larger energy

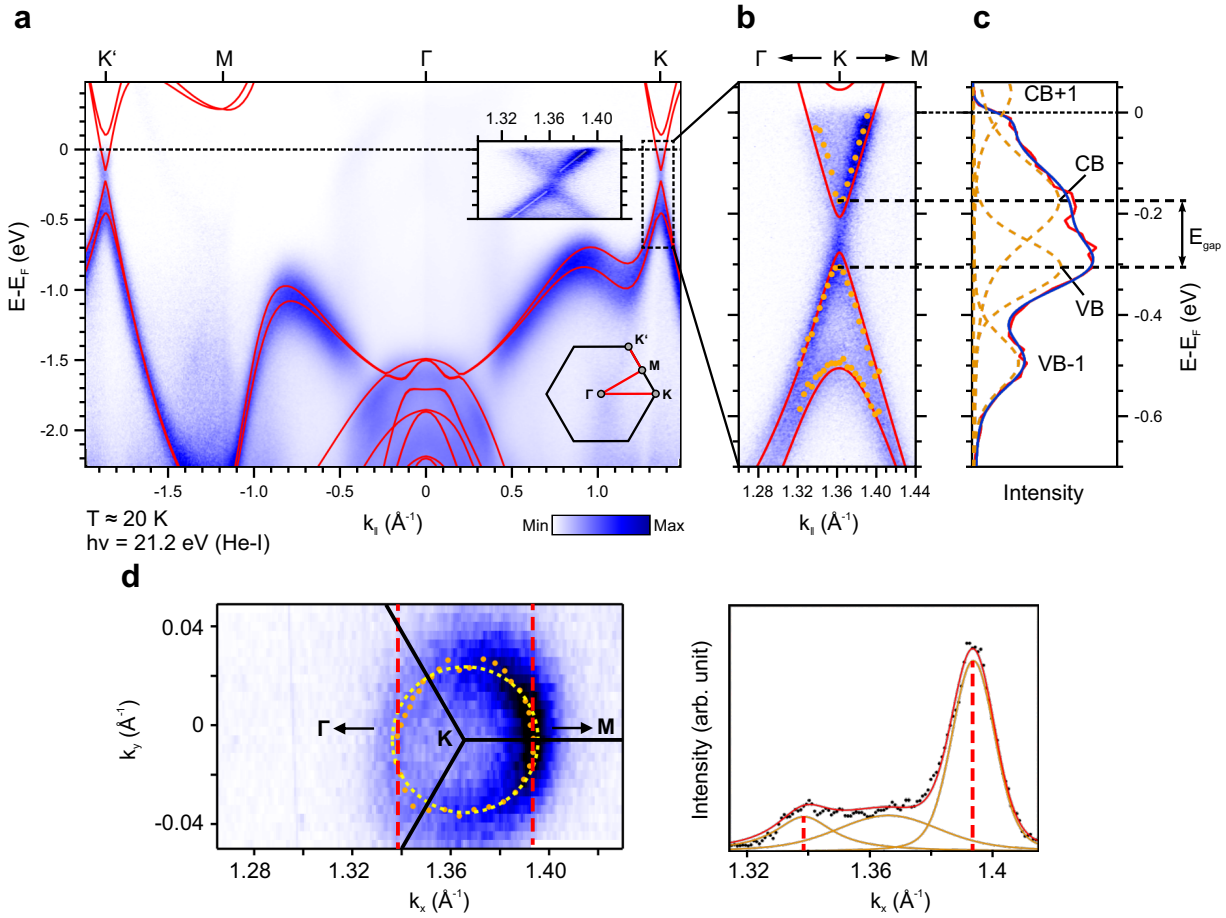

Figure 8.3: Band gap and charge transfer estimation in indenene by ARPES – **a**, DFT band structure from Fig. 7.4c (red curve) overlayed on the experimental ARPES data. The probed high symmetry directions in the Brillouin zone are illustrated in the lower right inset. The presence of an energy gap at the K-point is demonstrated with non-connectable linear dispersing valence and conduction bands in the upper inset. **b**, Close-up of the K-point overlayed with the DFT predicted Dirac bands. **c**, EDC (red curve) fitting at the K-point (sum: blue curve) decomposed the spectrum in three distinct peaks (dashed orange lines) of the valence (VB, VB-1) and conduction band states (CB, CB+1), respectively. This yields the orange markers in **b** and allows a band gap E_{gap} estimation of 125 meV. **d**, CEC at the Fermi level around the K-point averaged over an energy interval of 14.76 meV. MDC spectra (black data points) taken horizontally through the circular electron pocket were fitted with three single Voigt peaks (orange curves) accounting for the branches of the first conduction band (CB) and additional intensity induced by the second conduction band (CB+1). This fitting yields orange markers that trace the electron pocket and is highlighted with a dashed yellow circle on top. With that, the charge transfer from the substrate can be estimated. An unmonochromatized helium discharge lamp that produces faint satellite bands close to the Fermi level was used as a light source. Figures in **a-c** were taken from [110]. Figure in **d** was adapted from the supplemental material of [110].

scale. By fitting the peaks of the energy distribution curve (EDC) spectra for selected k values, as demonstrated for the K-point in Figure 8.3c, the ARPES band dispersion can be retraced by orange markers, which agree well with the DFT predicted bands on top. The employed fit procedure is based on three distinct peaks representing the first two valence band states (denoted as VB-1 and VB) and the lowest lying conduction band state (CB). The next higher conduction band state is cut-off by the Fermi-Dirac function. With this fitting, a band gap value for the smallest separation between the valence and conduction band state at the K-point is derived

to approximately $E_{gap} = 125\,\text{meV}$. Compared to the DFT value ($E_{gap,\,DFT} = 70\,\text{meV}$), this is in acceptable correspondence, as DFT predicted band gaps typically tend to be lower than the experimental values [131]. The conductance minimum around $-0.3\,\text{eV}$ in the LDOS, marked by an arrow in Fig. 8.2e, can then be identified as the Dirac point.

8.2.1 Charge transfer induced by the heavily *n*-doped SiC substrate

As mentioned earlier, the strongly n-doped SiC substrate induces the metallic behavior in indenene. With a nominal specific resistance of $\rho = (0.01 - 0.03)\,\Omega\,\text{cm}$ of the SiC substrate, the sheet charge carrier concentration at room-temperature amounts to $n_{SiC} = (1.0 - 8.5) \cdot 10^{12}\,\text{cm}^{-2}$ [44] (see Sec. 3.1). In the following, the charge carrier concentration in indenene will be estimated experimentally. For this, the size of the electron pocket centered around the K-point at the Fermi level was measured in a CEC by ARPES (see Fig. 8.3d). By fitting the momentum distribution curve (MDC) spectra (black data points; total fit: red curve) taken horizontally through the circular pocket with three single Voigt peaks (orange curves), a Fermi wave vector of $k_F = (0.029 \pm 0.009)\,\text{Å}^{-1}$ can be identified. Two peaks account for the outer branch of the first conduction band (CB) while the third peak in the center represents additional intensity induced by the second conduction band (CB+1). Repeating this fitting procedure for many MDCs, the circular electron pocket (dashed yellow circle) can be retraced by orange markers. The relationship $n \approx k_F^2/\pi = (2.7 \pm 1.7) \cdot 10^{12}\,\text{cm}^{-2}$ allows the charge carrier concentration in indenene to be estimated [132]. And indeed, the experimentally derived charge carrier concentration is of the same order as the one from the substrate, which proves the strong charge transfer. The uncertainty of the fit, the instrumental resolution, and local Fermi level fluctuation contribute to the error bar in k_F.

8.2.2 Fermi level fluctuations at the atomic scale

As presented above, a strongly doped substrate can alter the local electronic structure of the adlayer. Dopants are in general stochastically distributed in the bulk substrate material. The inhomogeneous dopant distribution in the subsurface of SiC causes a spatial Fermi level fluctuation, which leads to an uneven lattice corrugation of the indenene layer on top, as displayed in Figs. 8.4a and 8.1c. In the vicinity of film defects, marked by a red arrow in Fig. 8.4a, the detected height is for example lower than in the surrounding area. It is important to note that due to the topography as well as the local electronic properties contributing to the tunneling current, the STM technique is unsuitable to detect a clear structural influence of the dopant distribution on the indenene lattice on top. Atomically resolved atomic force microscopy (AFM), however, would be a qualified method that in principle would be able to obtain structural information.

In order to show the impact of the fluctuating potential landscape on the electronic structure, different locations on indenene separated by several nanometers were investigated by STS. To exclude any z-dependent effects induced by the tip, the tip-sample distance, at which point spectra were taken, was readjusted to the height difference between probing sites. The onsets of

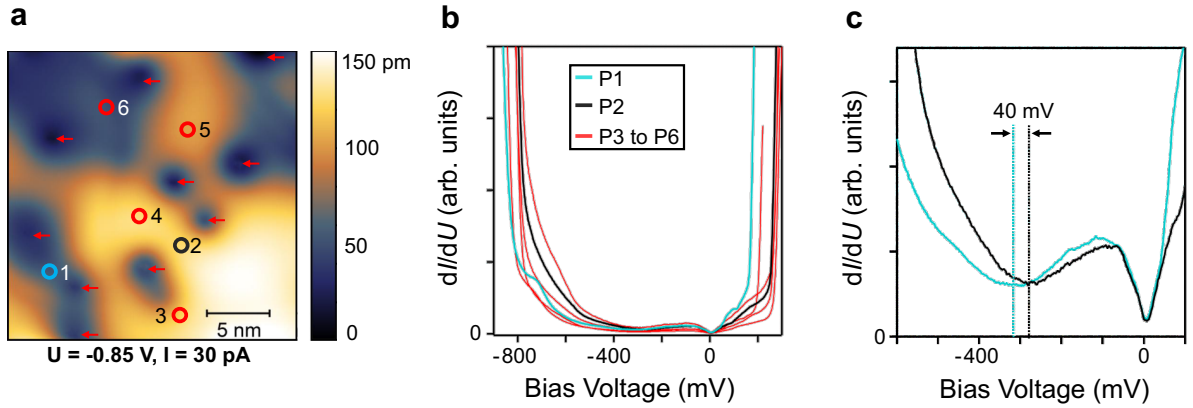

Figure 8.4: Fermi level fluctuation of indenene displayed in STM and STS – **a**, The apparent height in the STM topography image of indenene varies strongly over the scanned area, which is a result of an inhomogeneous dopant distribution in the SiC subsurface. In the vicinity of dopants (red arrows) the indenene film above appears in STM with a particularly low height. **b**, STS spectra, averaged over 100 single $\mathrm{d}I/\mathrm{d}U$ curves, taken at different positions in the scan area are highlighted by colored circles in **a**. Band onsets created by p_z-dominated states at $\sim -800\,\mathrm{mV}$ and $\sim 150\,\mathrm{mV}$ differ strongly in energy. **c**, $\mathrm{d}I/\mathrm{d}U$ curves (1 and 2 in **a**) with two extremal energy shifts. The two pronounced minima, marked by vertical lines, are separated by approximately 40 mV, which yields an average fluctuation amplitude of $\pm 20\,\mathrm{mV}$ on the nm-scale. Adapted from the supplemental material of [110].

the p_z-derived states at approximately $\sim -800\,\mathrm{mV}$ and $\sim 150\,\mathrm{mV}$ of the cyan $\mathrm{d}I/\mathrm{d}U$ curve in Fig. 8.4b (probing site P1 in Fig. 8.4a) are used here as a reference. This spectrum was taken in the vicinity of a film defect that renders the surrounding area to appear at lower height (darker color code). With respect to this spectrum, $\mathrm{d}I/\mathrm{d}U$ curves taken at other positions at higher apparent heights several nanometers away show, however, a shift to lower binding energies. Such shifts in energy have already been reported for Zn-doped GaAs(110) samples and attributed to a tip-induced band bending, which is strongly influenced by dopant atoms nearby [133]. The amplitude of the fluctuation in indenene is estimated with two representative, extremal shifted STS curves as depicted in Fig. 8.4c. Analogous to a method applied to graphene [134], the pronounced minimum in the $\mathrm{d}I/\mathrm{d}U$ signal of indenene, highlighted by dashed vertical line in Fig. 8.4c, is shifted by approximately 40 mV. This translates to an average energy shift of $\pm 20\,\mathrm{meV}$ in the investigated area. For bilayer graphene on SiC a similar value was identified [135]. Fermi level fluctuations detected on the μm-scale, however, reveal values on the order of $\pm 40\,\mathrm{meV}$ and are attributed to significant changes in the dopant concentration. This pronounced uneven potential landscape on the μm-scale leads to a blurred band structure that is probed and averaged on a macroscopic length scale in ARPES (photon spot diameter $\approx 1\,\mathrm{mm}$). In particular, the EDC peak widths shown in Fig. 8.3c exhibit a considerable broadening caused by the Fermi level fluctuation.

Interestingly, due to the population of the conduction band states, a constant tunneling contribution produces a finite conductance within the band gap in contrast to a vanishing $\mathrm{d}I/\mathrm{d}U$ signal, as expected for a true insulator [136–138]. The differential conductivity displays another interesting feature: a so-called zero-bias anomaly (ZBA), i.e. a global minimum pinned to zero bias, which occurs irrespectively of the local potential variation (see Figs. 8.2e and 8.4b, c).

Although there are several hypotheses explaining the formation of this ZBA, this phenomenon's signatures strongly depend on the probing details [139–141]. As a result, the ZBA is not an inherent feature of the electronic structure.

After characterizing the electronic properties and identifying a substantial band gap in indenene, the topological nature will be investigated. As presented in Figure 7.4b, the topology in indenene depends strongly on the bonding distance between the In-monolayer and the substrate. In the following, XSW measurement results reveal this bonding distance, and therefore begin to uncover the topology of indenene.

8.3 The indenene-substrate bonding distance – a first indication of non-trivial topology

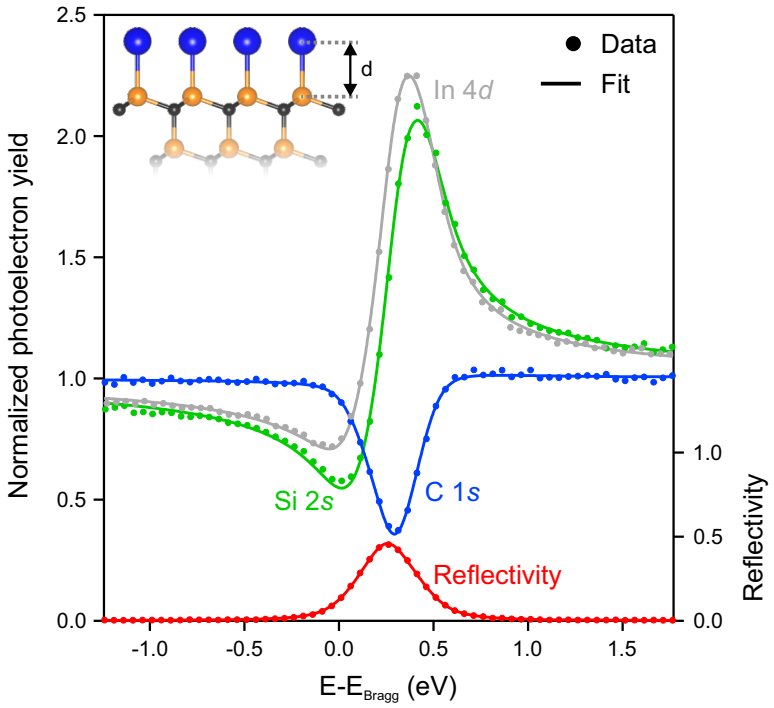

Figure 8.5: Determining the In-SiC bonding distance by XSW – Normalized photoelectron yield profiles and a reflectivity curve of indenene on SiC(0001) obtained in a normal incidence X-ray standing wave (NIXSW) experiment measured at room-temperature. The inset depicts the structural model with the bonding distance d from Fig. 7.4b. Adapted from the supplemental material of [110].

To reveal the bonding distance, a normal incidence X-ray standing wave experiment was employed. Through the interference of an X-ray beam impinging on the sample and Bragg reflected from the (0004) plane of the SiC crystal, the X-ray standing wave itself was created. Details on the XSW method are provided in Sec. 4.4. This experiment was conducted with the sample at room-temperature (RT) and at low temperatures in the range of $20 - 30\,\mathrm{K}$ (LT) in order to learn more about a potential temperature dependency of the bonding distance. In Figure 8.5 all XSW results of indenene measured at room-temperature are summarized. The photoelectron

yield measured for the C 1s, Si 2s, and In 4d core-levels as well as the X-ray reflectivity curve are depicted. To calculate the bonding distance from these curves information on the coherent position and the coherent fraction is needed. These two values are the average vertical position and variation modulo of the SiC (0004) lattice spacing. They are obtained via a standard fitting procedure applied to the measured XSW profiles and are described in Ref. [142]. For both temperatures the results are summarized in Table 8.1. As can be seen no temperature dependency was found. The uncertainty in the vertical positions is adjusted by the SiC(0001) bilayer distance taken from Ref. [42]. Coherent fraction values close to 1 (see Tab. 8.1) imply a highly ordered crystal lattice as observed for the indenene film (see Sec. 8.1.1). Values above 1, however, are the result of non-linear effects in the photoelectron detector.

Element	RT (LT) Coherent position (Å)	RT (LT) Coherent fraction
Si	0.009 ± 0.025 (0.012 ± 0.025)	1.109 (1.085)
C	-0.623 ± 0.025 (-0.609 ± 0.025)	1.026 (1.006)
In	2.678 ± 0.025 (2.683 ± 0.025)	0.982 (1.016)

Table 8.1: XSW results for the bonding distance of indenene to SiC(0001) – Average coherent positions and fractions of In, Si and C atoms measured at room-temperature (RT) and at low temperature (LT; $20 - 30$ K). The absolute values are calculated with the SiC(0001) bilayer distance from Ref. [42]. Taken from the supplemental material of [110].

The bonding distance between the indenene layer and the uppermost Si atoms of the substrate is calculated from their coherent positions to (2.669 ± 0.036) Å at RT and (2.671 ± 0.036) Å at LT, respectively. Both values correspond well to the equilibrium distance of $d^{DFT} = 2.68$ Å of the structurally relaxed heterostructure derived from DFT (see Sec. 7.2 for more information). Moreover, the obtained XSW values are significantly larger than the theoretically proposed critical distance of $d^{crit} = 2.57$ Å. Thus, based on the XSW results, indenene is placed in the topologically non-trivial regime (cf. Fig. 7.4b). An unambiguous topological characterization, however, is the charge localization within the unit cell presented in the following.

8.4 Topological classification based on charge localization

As presented in the previous chapter, the real-space charge localization of the Dirac fermions at K/K' is directly linked to the topology in indenene (see Sec. 7.2). Spatially resolved STS is ideally suited to identify this energy-dependent local charge distribution pattern of the Dirac bands. The results are depicted in the upper row of Figure 8.6a. The dI/dU maps comprising several indenene unit cells and were measured at selected bias voltages to provide a comparison with the DFT prediction shown in the row below. Here, the energy scale from DFT adapts the rigid band shift induced by the strong n-doped substrate (see Fig. 8.6b). Again, probing the p_z-dominated states at 300 mV bias voltage allows a precise registration of the unit cell with the underlying lattice. Using spatially resolved STS, the conduction bands at 190 mV and -150 mV reveal a clear shift of the maximum charge accumulation from the B to the A side of

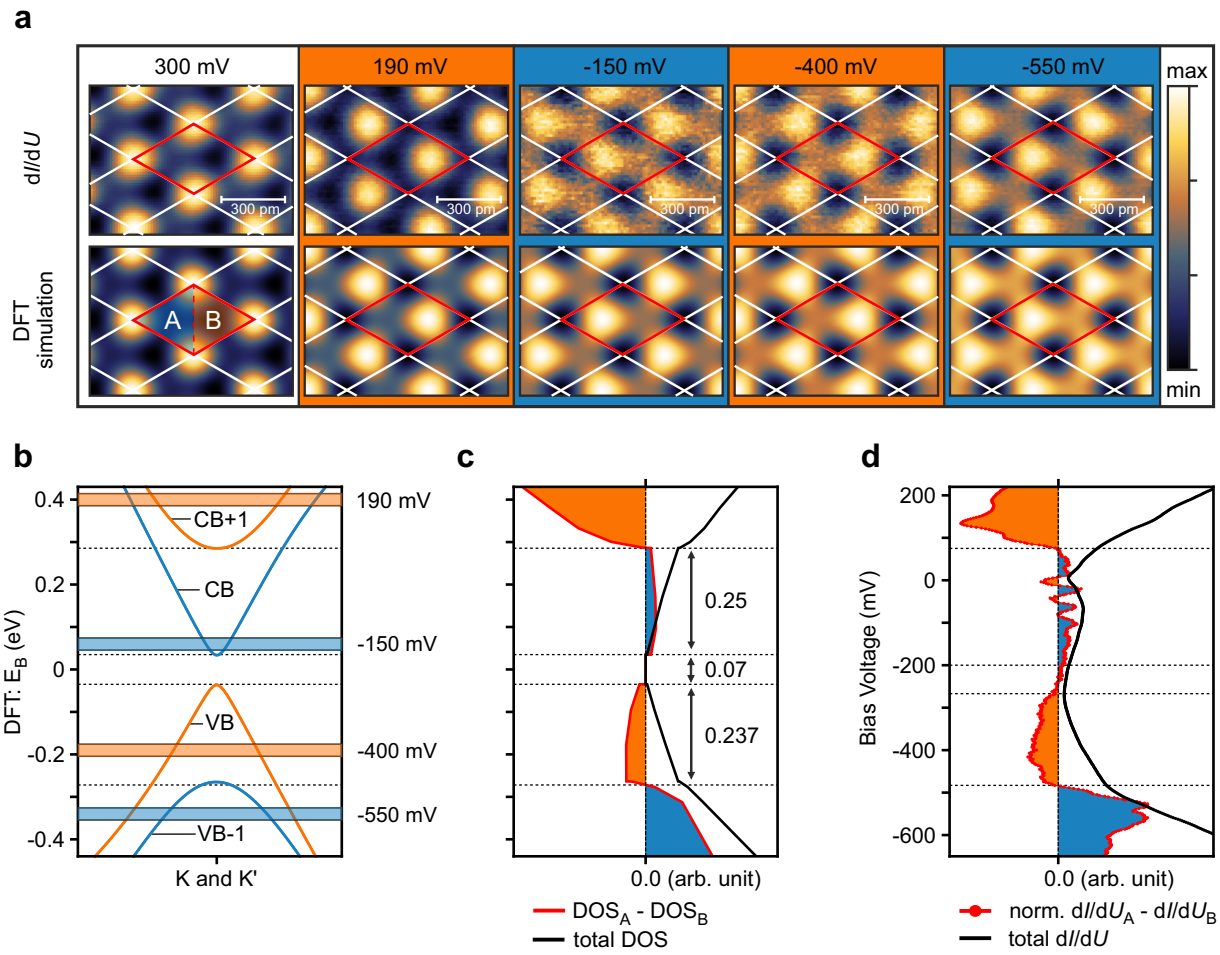

Figure 8.6: Identification of indenene as a QSHI by probing the unique charge localization sequence at the atomic scale – **a**, Spatially resolved constant height $\mathrm{d}I/\mathrm{d}U$ maps measured at different bias voltages (upper row) compared with their respective DFT simulation (lower row). A topologically non-trivial charge localization between A and B is detected. The modulation voltage and frequency of the lock-in amplifier was set to $U_{mod} = 10\,\mathrm{mV}$ and $f = 971\,\mathrm{Hz}$, respectively. Indium atom positions and registry of the unit cell are identified by probing p_z-orbital dominated states. **b**, Close-up of the Dirac bands around K/K' from DFT. The bias voltages of the $\mathrm{d}I/\mathrm{d}U$ maps used in **a** are highlighted in orange and blue representing the A and B side of the unit cell, respectively. **c**, Difference between the DOS of the A and B side (red curve) compared to the total DOS (black curve). At transitions between the valence and conduction bands, the difference in DOS changes sign indicating a switch in the charge localization. **d**, Normalized difference of $\mathrm{d}I/\mathrm{d}U$ point spectra taken on the A and B side, covering the relevant energy range of the Dirac bands at K/K'. The STS spectra were recorded with the same lock-in settings described in **a**. A constant tip to sample distance was achieved here by choosing, firstly, suitable tunneling parameters to obtain a featureless topography in the constant current mode and then, secondly, approach the tip to the sample surface by $\Delta z = -2.8\,\text{Å}$ to achieve an adequate $\mathrm{d}I/\mathrm{d}U$ signal. The signal normalization is discussed in Sec. C.3. Adapted from [110].

the triangular unit cell. Moreover, by lowering the bias voltage further to $-400\,\mathrm{mV}$, STS only probes the first valence band state and identifies the maximum charge localization on the B side again. And lastly, the $\mathrm{d}I/\mathrm{d}U$ map taken at $-550\,\mathrm{mV}$ shows a clear charge localization in the A void. This energy-dependent BABA charge localization sequence was also experimentally identified in the difference of $\mathrm{d}I/\mathrm{d}U$ point spectroscopies taken on either side of the unit cell (see Fig. 8.6d). Also here, the theoretical predicted difference in DOS between the A and B

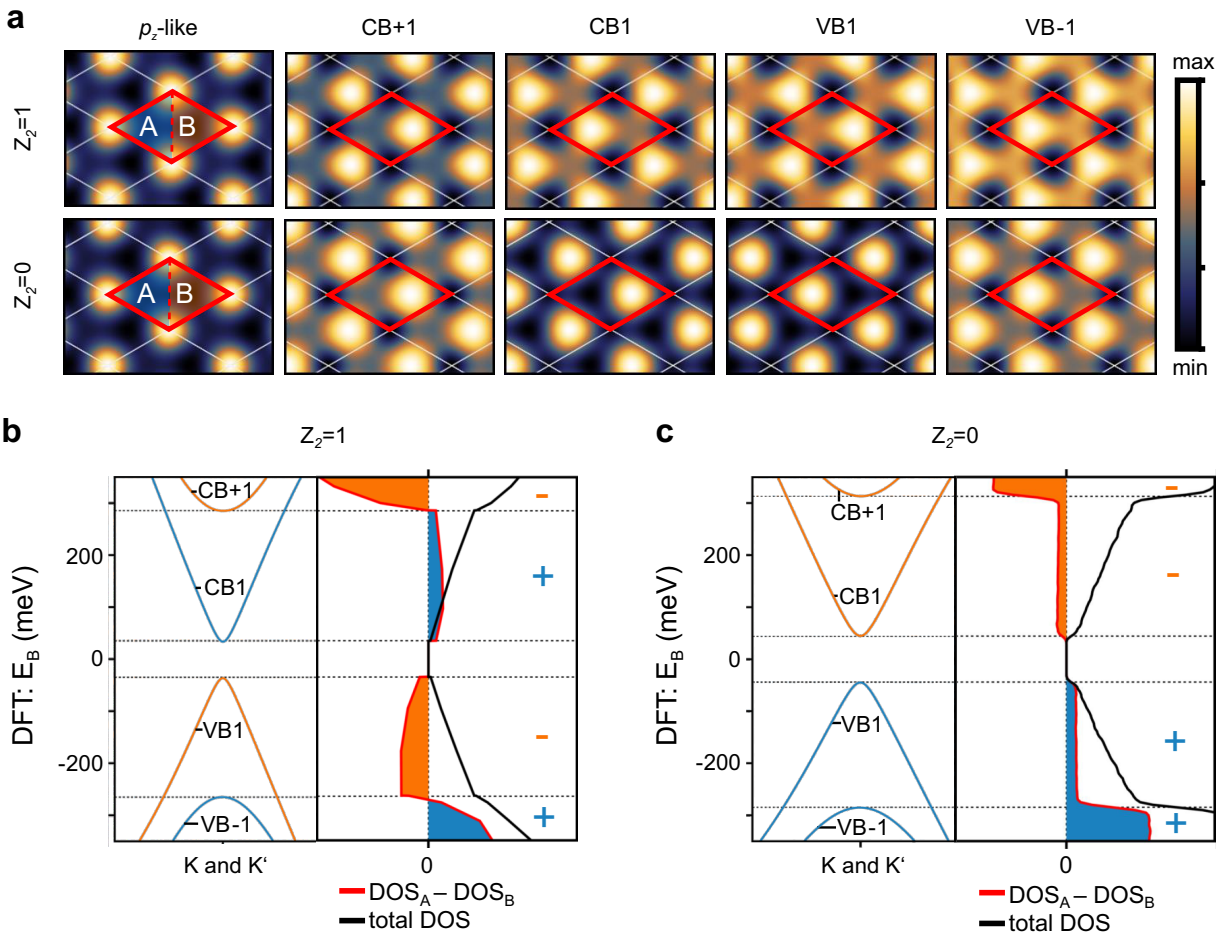

Figure 8.7: Topologically trivial and non-trivial charge localization in theory – **a**, Comparison between DFT simulated charge localization pattern addressing the valence (VB, VB-1) and conduction band states (CB, CB+1) at K/K', respectively, in the topologically non-trivial ($Z_2 = 1$; upper row; cf. Fig. 8.6a) and trivial case ($Z_2 = 0$; lower row). The non-trivial ABAB sequence is in strong contrast to the trivial AABB sequence (cf. Fig. 7.1d). The topologically trivial indenene phase was theoretically established by artificially shortening the indenene-SiC bonding distance to $d = 2.5\,\text{Å}$, which is smaller than the critical distance of $d^{crit} = 2.57\,\text{Å}$ (see Sec. 7.2 for more information). Dirac band structure and energy-resolved DOS in the non-trivial (**b**; cf. Fig. 8.6b, c) and trivial case from DFT (**c**). Only in the non-trivial phase appears an alternating sign of the difference DOS signal over the relevant energy range. Adapted from the supplemental material of [110].

side (see Fig. 8.6c) matches excellently with the experimental result. In particular, it is clearly evident that a reversal of the charge localization from A to B, or vice versa, leads to a switch of the sign of the difference LDOS signal. Close to zero bias, the difference signal in Fig. 8.6d exhibits a pronounced noisy character. This can be attributed to the ZBA shown in the total $\mathrm{d}I/\mathrm{d}U$ curve, which leads to small fluctuations in the respective signals taken at the A and B side. When calculating the difference in DOS between the A and B sides, these fluctuations are amplified. Overall, an ABAB charge localization sequence is experimentally detected and in great accordance with the DFT prediction. This is a proof of the non-trivial character in indenene.

However, a complete characterization of the topological nature of indenene is only possible

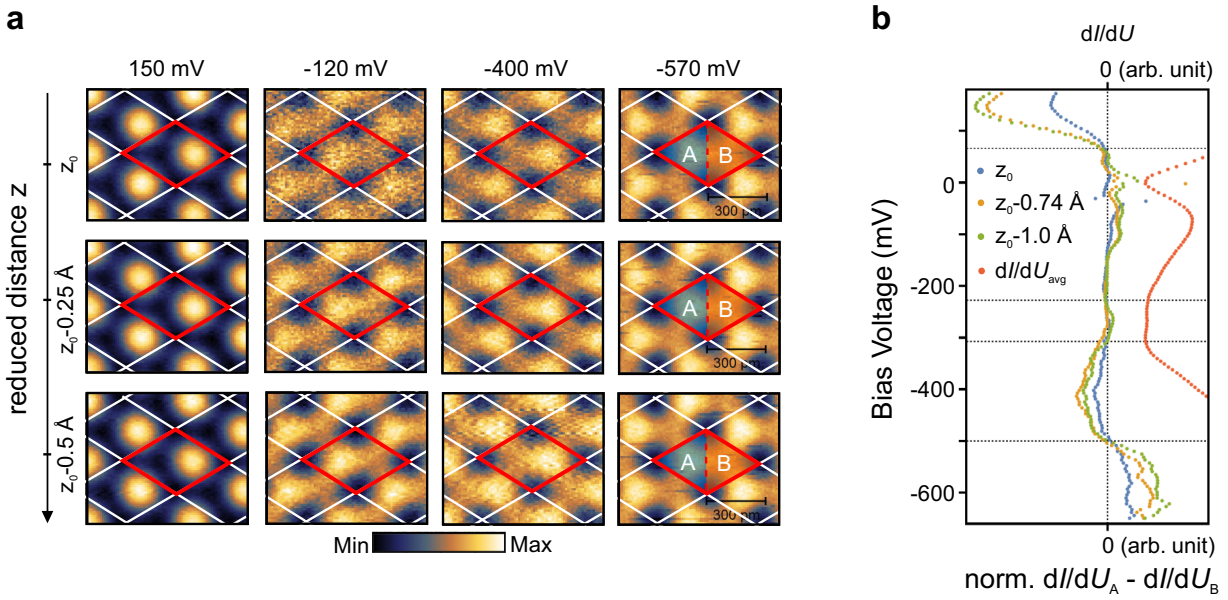

Figure 8.8: Influence of the tip-sample distance on the charge localization behavior – **a**, dI/dU maps recorded for various constant heights z at comparable energies used in Fig. 8.6a. **b**, Difference dI/dU spectrum between the A and B side of the indenene unit cell taken at several tip-sample distances. All spectra illustrated in **a** and **b** demonstrate a strong robustness of the topological character upon varying the tip-sample distance. The spatially averaged STS signal (red) acquired at $z_0 - 1.0$ Å is depicted. All difference spectra are averaged over 100 single dI/dU measurements per site A and B, respectively. Adapted from the supplemental material of [110].

by comparing this localization pattern from experiment with its topologically trivial counterpart from theory. For this purpose, the bonding distance to the substrate was artificially shortened in the DFT calculation to a value of $d = 2.5$ Å. Figure 8.7a shows the theoretically simulated charge localization sequence as a comparison between the topologically non-trivial ($Z_2 = 1$) and trivial ($Z_2 = 0$) case. Directly evident is the non-alternating localization sequence in the trivial case for the valence and conduction states, respectively. Likewise, the difference in DOS between both halves of the unit cell demonstrate an AABB sequence in Figure 8.7c. This comparison proves the non-trivial nature of indenene on SiC(0001).

As a next step, the influence of the tip-sample distance on the detection of the charge localization is investigated. Recently, it has been shown for the topological Dirac semimetal Na_3Bi that a topological phase transition can be triggered locally by the electric field between the STM tip and the sample surface, rendering this material topologically trivial [143]. In order to learn more about tip-induced effects on the charge localization behavior in indenene, several spatially resolved dI/dU maps as well as local dI/dU measurements at different tip-sample distances z were conducted. In this way, the electric field induced by the tip is varied. The dI/dU maps were recorded at bias voltages close to the ones used in Fig. 8.6a. The amplitude of the tunneling signal restricts the utilizable z-range in experiment to approximately 1 Å, where the lower limit in particular is defined by the stability of the tunneling contact. In Figure 8.8 the results are presented. As can be seen for all used z-values the charge localization asymmetry in the indenene unit cell is detectable irrespective of the tip-sample distance. The same holds for the

characteristic sign changes in the difference spectra depicted in Fig. 8.8b. This implies a stable in-plane ISB-induced splitting of the Dirac bands at K/K'. Overall, the topological character in indenene is robust against the local influence of the tip-induced effects investigated here.

In summary, the structural and spectroscopic results from STM, STS, XSW, and ARPES agree well with the DFT prediction, which establishes indenene as a novel QSHI. Based on the detection of bulk observables by STS, the unique link between topology and charge localization was successfully utilized to identify the non-trivial character of indenene. The results from STS show robust signatures that differ significantly from the trivial case, irrespective of the tip-induced electric fields studied here. A sizeable band gap of approximately $E_{gap} = 125\,\mathrm{meV}$ separates the quasi-linear bands at the K-point and confirms the presence of massive Dirac fermions.

9 Conclusions and outlook

The focus of this thesis was the experimental realization of buffer layers made of Al and In on SiC(0001) in order to accommodate quasi-freestanding stanene while preserving its fragile topology. An in-depth structural and spectroscopic investigation however found no indications of the theoretically predicted ($\sqrt{3} \times \sqrt{3}$) lattices. A possible explanation could be that these surface reconstructions are thermodynamically unstable in experiment. While pursuing this investigation, a novel QSHI based on a triangular monolayer of In atoms was found.

In general, the growth and characterization of ultrathin metal films of group-III elements on SiC(0001) presented in this thesis sheds light on a rather untouched research field, which is indicated by few published experimental reports in literature to date. The reason might be the complex and elaborate hydrogen etching procedure necessary to obtain a well-ordered and atomically flat SiC substrate surface. In the following, an overall conclusion and outlook will be given to the respective investigations of Al and In overlayer, as well as indenene grown on SiC(0001).

Al on SiC(0001):

The observed unusually large triangular and rectangular surface unit cells of thick Al films ($\Theta_{ML} \approx 2.2$ ML) are most likely a product of the tensilely strained Al lattice epitaxially grown on SiC(0001). The exact coupling strength between both lattices however is not yet known. Another emerging surface reconstruction is the quasi-1D Al phase, which exhibits a strong resemblance to the herringbone structure known from Au(111). With the help of the latter, a tentative structural model based on an alternating occupation of Al atoms on hcp and fcc lattice sites and the transition between them was proposed, which fit well to the STM topography data. Similar structures were reported for other heterostructure systems of metal adlayers on metallic and semiconductor substrates [96–100].

In order to fully understand the structure and formation of these new surface reconstructions, future investigations should aim more at theoretically derived models based on the phase-field-crystal model for example [101, 102]. With this, the relaxed Al atom positions in the unit cells could be identified. Due to the immense sizes of the unit cells and the expected large number of Al atoms therein, the problem could be too computationally demanding for DFT calculations. From the experimental side, AFM with atomic resolution could reveal the in-plane position of Al atoms within the unit cell, whereas transmission electron microscopy (TEM) could gain valuable insights on the vertical stacking of these atoms.

In on SiC(0001):

Thick In overlayer with a coverage in the range of $\Theta_{ML} \approx 3$ to ≈ 2 ML produce a (7×7), $(6 \times 4\sqrt{3})$, and $(4\sqrt{3} \times 4\sqrt{3})$ surface reconstruction with a strong metallic behavior and a distinct In-induced band structure. In these cases, the electrons follow the nearly-free electron model.

In general, In surface reconstructions observed on semiconductor surfaces, such as Si(111) [28, 109, 144, 145] and Ge(111) [146–148], exhibit a plethora of different physical phenomena. Low-dimensional In phases, such as linear In chains on Si(111) exhibit a charge density wave [149], whereas a In monolayer on the same substrate shows superconductivity [150]. Other In phases, however, demonstrate ordinary nearly-free electron and metallic behavior [107, 151]. The structural and spectroscopic characterization of the In phases on SiC(0001), which were unknown to the literature before, thus contributed to and line up in this immense manifold of In phases on semiconductor surfaces.

Indenene on SiC(0001):

Arranging In p-orbitals in a triangular lattice on SiC(0001) promotes an electronic honeycomb network with massive Dirac fermions in which the band gap size and topological character is defined by the competition between atomic SOC and substrate-induced in-plane ISB. As a consequence, the topologically non-trivial nature in indenene manifests in a unique charge accumulation sequence within the unit cell that was experimentally exploited. The method of obtaining the topological character from this bulk observable is exceptional among most topological material systems, which primarily utilize the bulk-boundary correspondence.

The topology in indenene can also be obtained via other bulk observables, which could be the focus of future studies. For instance, the detection of the OAM polarization in the Dirac bands at K/K' with circularly polarized light by ARPES, as proposed for graphene by Schüler *et al.* [127], could provide direct access to the Berry curvature. This characteristic connection was already confirmed in WSe_2 [128, 129] and successfully exploited in TaAs [130].

A 2D triangular lattice design based on other group-III elements, such as Al and Ga, demonstrates a topologically trivial band arrangement according to preliminary theoretical results. In these cases, the greater influence of ISB, possibly due to a smaller bonding distance to the substrate, could outweigh the non-trivial atomic SOC. Future investigations could therefore reveal the opposite topological character in experiment and thus confirm the derived theory.

Another way of obtaining a clear topologically non-trivial signature is the experimental realization of the QSHE in indenene. However, transport measurements in general require breaking the UHV environment, leaving the surface exposed to ambient conditions, which results in the oxidation and degradation of the indenene layer, as an experimental study suggests [152]. A weakly van der Waals bonded capping layer on top, such as hexagonal boron nitride, could protect indenene without compromising its low-energy spectrum. Moreover, both the SiC substrate and capping layer must be electrically insulating to ensure that only indenene's properties are probed in transport. Un- or lowly n-doped SiC would also place the Fermi level between the

valence and conduction band in indenene, which would be in contrast to the metallic situation observed in this work.

In general, the perception of triangular 2D lattices changes drastically with the demonstration of indenene and expands the collective understanding of how novel QSHI materials can be designed. The work presented here is therefore only the beginning, and fascinating results are still awaiting that may contribute to the realization of future room-temperature quantum computing devices.

Appendix

A Al on SiC(0001)

A.1 Chemical characterization and Al coverage estimation with XPS

The growth quality and the chemical composition is investigated by XPS directly after both Al deposition steps. Figure A.1 displays an overview spectrum of all measured core-levels of the SiC substrate and the Al overlayer. The intense Al $2p$ core-level at approximately 72.8 eV exhibits a small shoulder at roughly 75 eV (red arrow), which indicates a low degree of Al oxidation on the surface. This observation is further supported by the notable but still minute oxygen O $1s$ peak height shown in the inset of the overview scan. A potential source of this small amount of oxygen could be the adsorption of residual gas species during *in situ* transfers. Overall, high quality Al film growth is demonstrated.

All core-levels depicted next to the overview spectrum and the O $1s$ in the inset are normalized by the area under the Si $2p$ core-level peak after subtraction of a Shirley background, respectively, including the Si $2p$ core-levels itself.

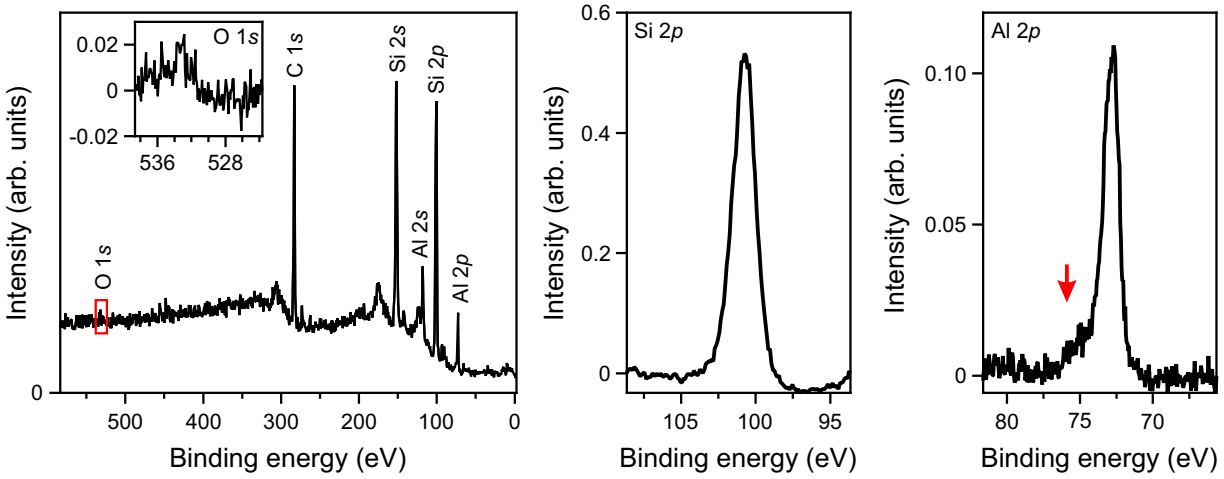

Figure A.1: Chemical characterization of Al-SiC by XPS – Overview XPS spectrum of a representative Al-SiC sample with measured core-levels of the substrate and the Al overlayer. Inset: Close-up of the O $1s$ core-level. Al $2p$ core-level spectrum with a noticeable shoulder of oxidized Al content pointed out by the red arrow. The Al, Si, and O peak are normalized with the area under the Si $2p$ peak after a Shirley background is subtracted, respectively. During the measurement the sample was at room temperature and a unmonochromatized Al-Kα X-ray tube with 1486.6 eV photon energy was used as a light source.

Element i	$E_{kin,i}$ (eV)	I_i (arb. units)	σ_i (Å^2)	$T(E_i)$ (arb. units)	λ_i (Å)
Al $2p$	1411	403	0.000072 [77]	49 [153]	27.3 [154]
Si $2p$	1384	2264	0.00011 [77]	48 [153]	26.1 [154]

Element i	β_i (arb. units)	δ_i (Å)	a_i (Å)	$\rho_{2D,i}$ (Å^{-2})
Al $2p$	0.9535 [77]	2.34	2.86	0.14
Si $2p$	1.026 [77]	2.51	3.07	0.12

Table A.1: Parameters to estimate the Al film coverage by XPS with Equations 4.22 and 4.23 – $E_{kin,i\,2p}$ represents the kinetic energy of the $2p$ core-level photoelectrons and I_i the core-level intensity. σ_i stands for the cross section, $T(E_i)$ is the analyzer transmission function, and λ_i is the inelastic mean free path at the respective core-level energies. Additionally, $\lambda_{Al/SiC} = 26.9\,\text{Å}$ is the inelastic mean free path of the Al overlayer at the kinetic energy of the Si $2p$ peak [154]. β_i features the asymmetry parameter, δ_i the layer distance, a_i the in-plane lattice constant, and $\rho_{2D,i}$ the 2D layer density. All structural parameters from the last row are taken from crystal structures of the respective materials visualized with the *VESTA* software [45].

With the core-level intensities of the Al overlayer and Si-terminated SiC substrate at hand (see Table A.1), the Al coverage can be estimated according to Equations 4.22 and 4.23. The coverage amounts to approximately 2.2 ML (layer thickness of 5.1 Å). This means that a rather thick Al overlayer was grown on the SiC substrate. As stated in Sec. 4.3.3, due to many uncertainties and assumptions, the resulting coverage and layer thickness bears a large error bar. Therefore, this coverage should only represent a rough estimation, which eventually places the discovered Al phases in the high coverage regime ($\Theta_{ML} > 1$ ML).

A.2 Step heights at the atomic scale on Al/SiC(0001)

The step heights of the Al film are further analyzed in STM with the results depicted in Figure A.2. The majority of identified step heights are related to the 4H-SiC(0001) substrate unit cell and occur in the 2H- and 4H-unit cell heights (see Fig. A.2b). Due to the finite film thickness of different Al phases (see, e.g., Fig. 5.5e and f), the red height profile between a triangular and rectangular domain depicted in Fig. A.2b shows a substrate unit cell step influenced by the distinct film thicknesses of the respective Al phases. In principle, the obtained height could also stem from a substrate step edge of 1.25 unit cells high. However, since ¼ steps are energetically unfavorable, they can be excluded here [155]. Moreover, the threefold symmetry of the SiC(0001) surface is imprinted on the Al film, as can be seen by the terrace edge orientations highlighted by two dashed gray lines in Fig. A.2a. Both are rotated by an angle of 120° with respect to each other.

The double-tip present in this STM experiment produces further measurement artifacts as can be seen in Fig. A.2a (white arrows), which are also schematically illustrated in Fig. A.2c (red line). A small side-tip establishes a tunneling contact on only one side of the step based on the scanning direction of the tip. Eventually, this leads to the appearance of a false step in the topography. The true step height d, however, can be still identified on the "backside" of the step, where the side-tip does not affect the topography.

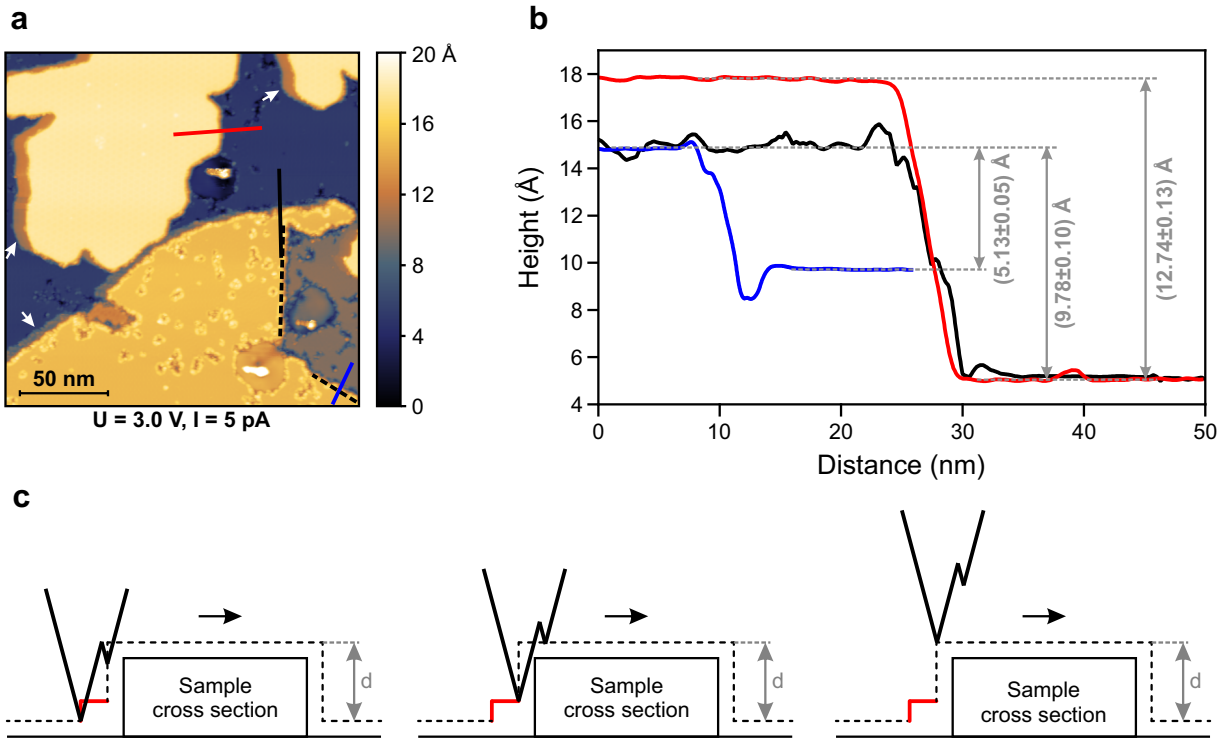

Figure A.2: Step height characterization of Al on SiC by STM – **a**, Overview STM image of Al-SiC as shown in Fig. 5.3a with line profiles across (red, black, and blue line) and two gray dashed lines along terrace edges. The white arrows mark the false steps, i.e., measurement artifacts. **b**, Height profiles of the respective lines shown in **a**. **c**, Schematic explanation of a double-tip artifact in the STM topography image and step height analysis. The tip trajectory is depicted with a gray dashed line. The true step height d is not affected by the double-tip.

B In on SiC(0001)

B.1 Chemical characterization and In coverage estimation with XPS

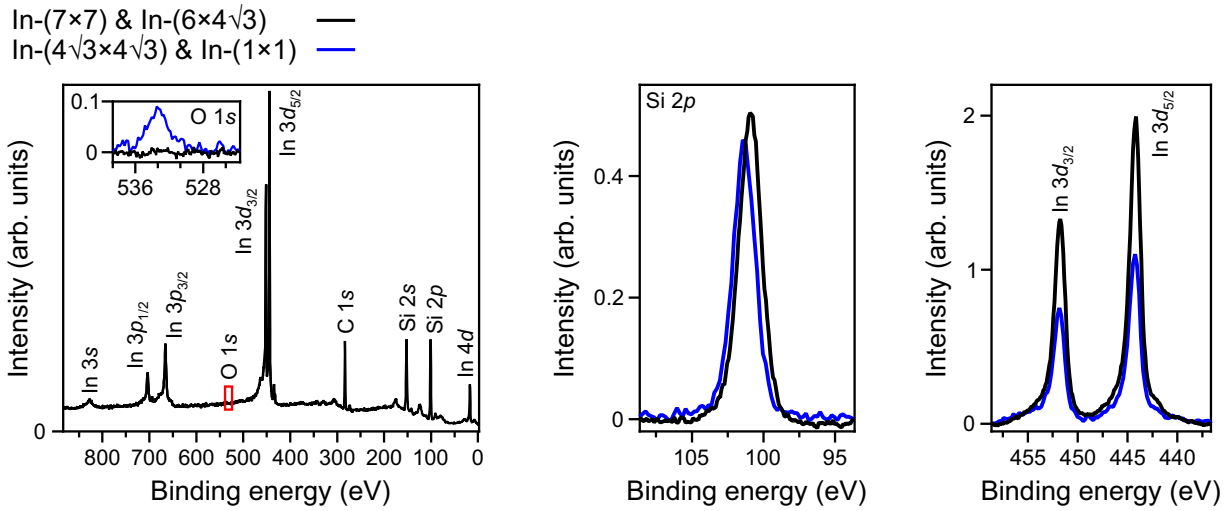

Figure B.1: Chemical characterization of In-(7×7), -$(6 \times 4\sqrt{3})$, and -$(4\sqrt{3} \times 4\sqrt{3})$ phases by XPS – XPS overview spectrum of representative In-SiC samples with Si $2p$ and In $3d$ core-levels. Both Si $2p$ core-level spectra are normalized by the area under their respective peaks. The In $3d$ and O $1s$ core-level spectra are further normalized by the associated Si $2p$ peak area, respectively. The spectra were recorded with a unmonochromatized Al-Kα radiation source with a photon energy of 1486.6 eV at room-temperature.

With XPS the growth quality and the chemical composition of the In overlayer is investigated. The results for the In-(7×7) and -$(6 \times 4\sqrt{3})$ reconstructions (black line) and the In-$(4\sqrt{3} \times 4\sqrt{3})$ (blue line) phase are illustrated in Figure B.1. The overview XPS spectrum reveals intense In $3d$ core-levels, which are much higher in intensity than the Si $2p$ and C $1s$ core-levels from the SiC substrate. In addition, no trace of oxygen (O $1s$) or other adsorbates can be identified, which shows the high chemical quality of the grown In films in accordance with the STM topography images presented in Fig. 6.1a, c and Fig. 6.2a, b. After annealing, the In-$(4\sqrt{3} \times 4\sqrt{3})$ phase emerges. The surface is also partially covered with a In-(1×1) lattice, as confirmed by STM and ARPES (cf. Fig. 6.8). Nonetheless, the overview XPS spectrum (not shown here) exhibits qualitatively the same features as depicted in Fig. B.1. Interestingly, a minute O $1s$ core-level appeared (see inset of Fig. B.1), which is attributed to oxygen-containing adsorbates introduced by several *in situ* transfers.

All core-levels depicted next to the overview spectrum and the O $1s$ in the inset are normalized by the area under the associated Si $2p$ core-level peak after subtraction of a Shirley background, including the Si $2p$ core-levels itself. At closer inspection both Si $2p$ core-level display almost an identical intensity for all In overlayer reconstructions, whereas the intensity of the In $3d$ core-levels drastically reduces after several annealing steps. This reduction is attributed to the thermal treatment that promotes desorption of In atoms from the surface. Eventually the In-$(4\sqrt{3} \times 4\sqrt{3})$ reconstruction is formed.

With all core-level parameters at hand (see Table B.1), the In coverage of the respective In

reconstructions can be estimated according to Equations 4.22 and 4.23. For the In-(7×7) and In-$(6 \times 4\sqrt{3})$ reconstruction a coverage of approximately 2.9 ML (layer thickness of 6.2 Å) is derived, whereas after several annealing steps the In-$(4\sqrt{3} \times 4\sqrt{3})$ phase exhibits a coverage of about 1.9 ML (layer thickness of 4.0 Å). The In-(7×7) and -$(6 \times 4\sqrt{3})$ reconstructions can therefore be placed certainly in the high coverage regime ($\Theta_{ML} > 1$ ML). Although the In-$(4\sqrt{3} \times 4\sqrt{3})$ phase has a significantly lower coverage, it can be placed in this regime as well.

From Chapter 7 and 8 it is known that the In-(1×1) exhibits a coverage of 1 ML. Here, both phases, i.e., the $(4\sqrt{3} \times 4\sqrt{3})$ and (1×1), are investigated simultaneously by XPS and thus contribute to the same In $3d$ core-level signal. The amount of the (1×1) reconstruction on the surface is estimated from STM (not shown here) to approximately 30 to 40%. This would translate to a In-$(4\sqrt{3} \times 4\sqrt{3})$ coverage of about 2.3 to 2.6 ML. Note, however, as already stated in the XPS methods in Sec. 4.3.3, the resulting thicknesses and coverages of these estimations bear a significant error bar and, thus, only lead to an approximate positioning in the coverage phase diagram. Therefore, in the following a coverage value of 1.9 ML for the In-$(4\sqrt{3} \times 4\sqrt{3})$ reconstruction is used.

Element i	I_i (arb. units) of In-(7×7) and In-$(6 \times 4\sqrt{3})$	I_i (arb. units) of In-$(4\sqrt{3} \times 4\sqrt{3})$
In $3d$	15042	10306
Si $2p$	2484	2757

Element i	$E_{kin,i}$ (eV)	σ_i (Å^2)	$T(E_i)$ (arb. units)	λ_i (Å)
In $3d$	1036	0.003098 [77]	52 [153]	16.9 [154]
Si $2p$	1383	0.00011 [77]	49 [153]	26.1 [154]

Element i	β_i (arb. units)	δ_i (Å)	a_i (Å)	$\rho_{2D,i}$ (Å^{-2})
In $3d$	1.208 [77]	2.09	5.92	0.08
Si $2p$	1.026 [77]	2.51	3.07	0.12

Table B.1: Parameters to estimate the In film coverage by XPS with Equations 4.22 and 4.23 – $E_{kin,i}$ represents the kinetic energy of the respective core-level photoelectrons and I_i the core-level intensity. σ_i stands for the cross section, $T(E_i)$ the analyzer transmission function, and λ_i the inelastic mean free path at the respective core-level energy. Additionally, $\lambda_{In/SiC} = 20.79$ Å is the inelastic mean free path of the In overlayer at the kinetic energy of the Si $2p$ peak [154]. Further, β_i features the asymmetry parameter, δ_i the layer distance, a_i the in-plane lattice constant, and $\rho_{2D,i}$ the 2D layer density. All structural parameters from the last row are taken from crystal structures of the respective materials visualized with the *VESTA* software [45].

C Indenene

All results presented in this appendix are adapted from the supplemental material of the publication by Bauernfeind *et al.* [110].

C.1 Overview of triangular and hexagonal adsorbate systems

Table C.1 gives an excerpt of experimentally realized surface adsorbate systems with the respective elements yielding either a hexagonal or triangular lattice symmetry. Throughout this periodic table, triangular adsorbate lattices (▲ and △) occur more often than hexagonal ones (⬡ and ⬢), in particular when going to higher atomic numbers Z. Interestingly, metallic substrates were often used as substrates for hexagonal adlayers. Such substrates, however, impose a certain charge transfer on the adlayer, which would impede a sole edge conductance in the QSHE. Utilizing insulating substrates to circumvent this problem primarily results in triangular adlayer lattices, which therefore constitutes a promising design environment.

			B	**C** ⬡ [156]	**N**
			Al △ [31]	**Si** ⬡ [157] ⬢ [159–161] △ [162]	**P** △ [158]
Ni	**Cu** ▲ [163]	**Zn**	**Ga** △ [164]	**Ge** ⬡ [25] ⬢ [167–169]	**As** △ [165, 166]
Pd	**Ag** ▲ [170]	**Cd**	**In** indenene [110] △ [28]	**Sn** ▲ [106, 171] ⬢ [16, 20, 21] △ [173–176]	**Sb** △ [172]
Pt △ [177]	**Au** ▲ [178] △ [182–184]	**Hg**	**Tl** △ [179, 180]	**Pb** ⬢ [181] △ [175, 185]	**Bi** ⬡ [118] △ [186, 187]

Table C.1: Periodic table of literature overview on adsorbate systems – Schematic overview of adsorbate systems in the (sub-) monolayer regime on insulating (empty symbols) and metallic substrates (filled symbols). The surface lattice symmetry is either hexagonal or triangular. Intercalation layers between graphene and the substrate (denoted as ▲) exhibit triangular symmetry. Indenene belongs to the triangular lattice group. The sum of all triangular (hexagonal) surface lattices is 28 (14). This table was adapted from the supplemental material of [110].

C.2 Indium adsorption site

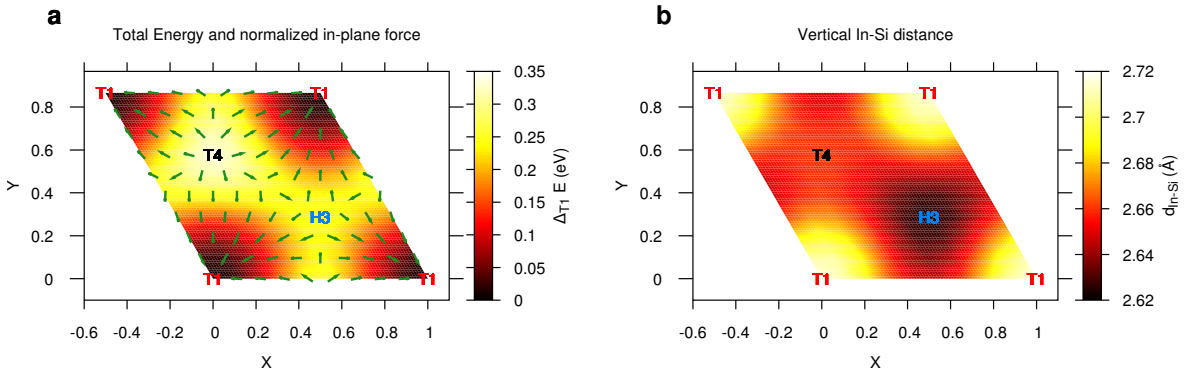

Figure C.1: DFT adsorption study of In atoms on SiC(0001) – **a**, Total energies mapped over the indenene unit cell. The energies are given with respect to the T1 site. **b**, Map of the bonding distance between an In and Si atom d_{In-Si} over the indenene unit cell. The in-plane coordinates are given in units of the lattice constant. In **a** and **b**, the adsorption sites on the SiC(0001) surface are denoted as T1, T4, and H3, respectively. Taken from the supplemental material of [110].

In order to theoretically determine the adsorption site of In atoms on SiC(0001) a map over the indenene unit cell comprising the total energies and in-plane forces acting on them was calculated in DFT using the generalized-gradient approximation parametrized by Perdew-Burke-Ernzerhof [188]. The indenene in-plane coordinate was sampled on a 9×9 grid while relaxing the out-of-plane coordinate. The energies are given with respect to the T1 site. As shown in Figure C.1a the most energetically favorable adsorption site with the lowest in-plane force acting on the In atoms is the T1 position, i.e., vertically above a Si atom. All other considered positions exhibit a larger total energy.

The T1 adsorption site further exhibits the largest bonding distance d_{In-Si} to the substrate (see Fig. C.1b). Due to the small influence of in-plane ISB on the In layer this configuration is topologically non-trivial (cf. Sec. 7.2). Indium atoms adsorbed on the other considered lattice sites yield shorter bonding distances, which would render indenene trivial. Note, that the Perdew-Burke-Ernzerhof (PBE) functional used for this analysis slightly overestimates the bonding distance. However, a more sophisticated functional, such as HSE, still confirms the non-trivial nature of indenene adsorbed on the T1 site.

The T1 adsorption site becomes further evident when comparing the experimental ARPES band structure (see Fig. 8.3) to the one from DFT, calculated for all considered adsorption sites (see Fig. C.2). Both, the T4 and H3 bonding situations yield a metallic band structure with bands at K/K' possessing strong p_z-orbital character far away from the Fermi level in clear contrast to the experimental ARPES result.

From the experimental side, the lateral position of the In atom can be determined by using a film edge imaged in STM, where the uncovered SiC substrate interfaces an indenene film (see Fig. C.3a and Fig. 8.2d). Here, atomic resolution on SiC(0001) and indenene (see Fig. C.3b) was achieved with a tunneling bias of 1.65 V and 0.45 V, respectively. In the case of indenene,

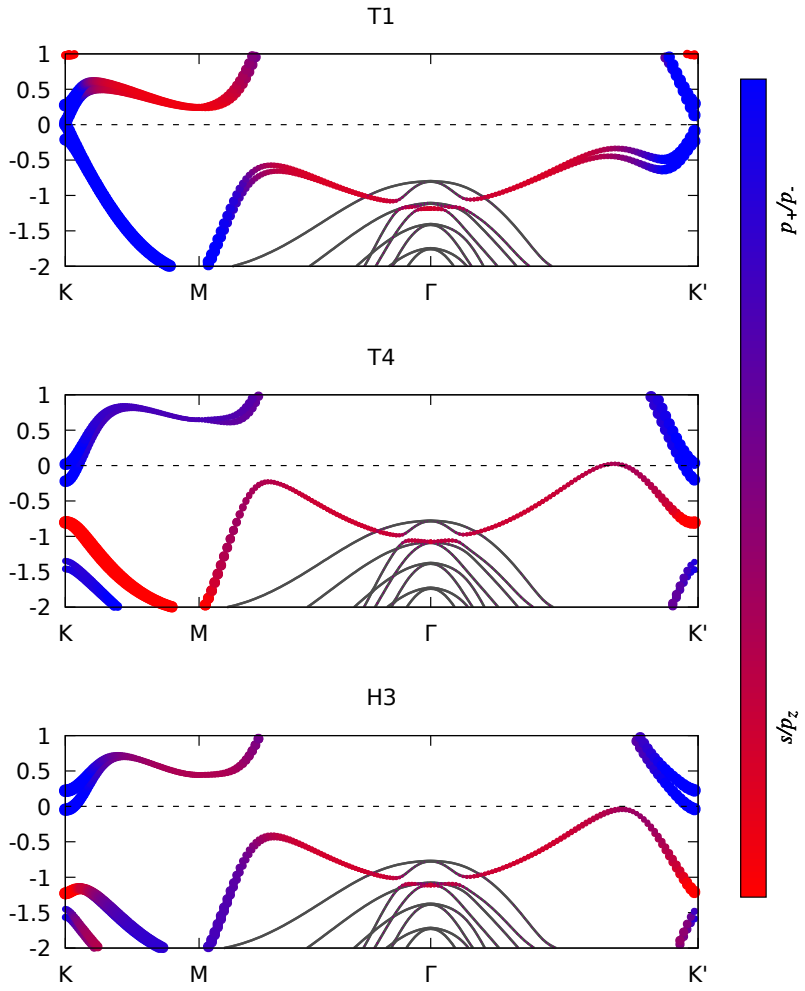

Figure C.2: DFT band structure analysis for different adsorption sites – Relaxed indenene unit cell adsorbed to the T1, T4, and H3 sites, respectively. The size marker represents the In character of the band, the color denotes the orbital composition. Taken from the supplemental material of [110].

the STM topography at this relatively high tunneling bias is dominated by the In p_z-orbital character (see Fig. C.2 for the T1 case). DFT supported STM studies of H-saturated SiC(0001) show an analogous relationship for the Si atoms on SiC(0001) at a bias voltage of 3.0 V [50]. This argument also holds for the bias voltage of 1.65 V. A surface defect, which is present in both topography images and marked by a red arrow in Fig. C.3, allows the corrugation profiles on indenene and SiC (orange and blue curve, respectively) to be aligned. These two line profiles are depicted in Figure C.3c. The periodic SiC(0001) lattice corrugation was extrapolated with a periodic function over the indenene side. As can be seen, the height maxima on the indenene side overlap with the maxima of the periodic function, which proves that In adsorbs on top of the Si atoms, i.e., the T1 position.

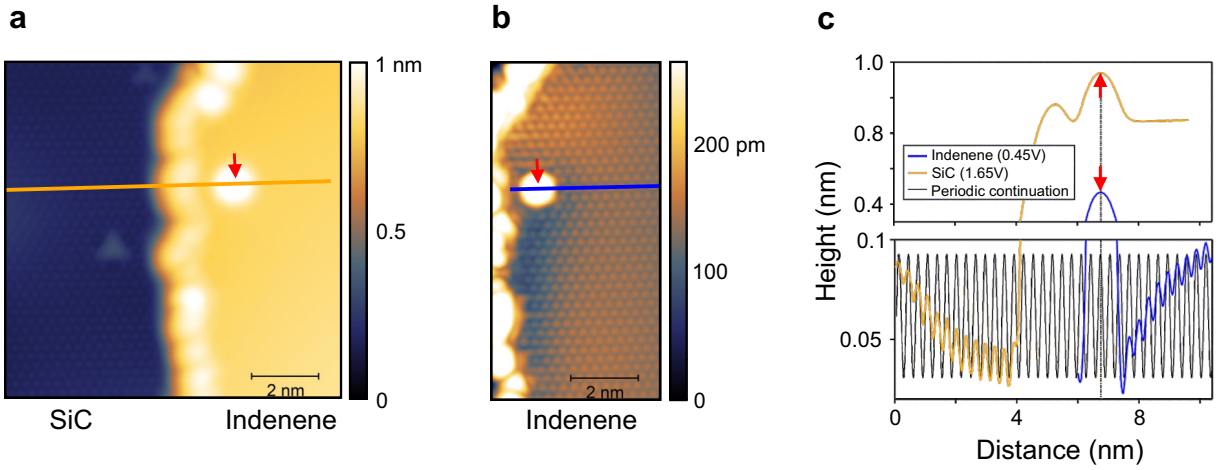

Figure C.3: Determination of indium adsorption site in STM – **a**, STM topography image of a film edge showing uncovered SiC on the left and the indenene film on the right recorded with tunneling parameters of $U = 1.65\,\mathrm{V}$ and $I = 80\,\mathrm{pA}$. **b**, STM topography image of the indenene side mapped with tunneling parameters of $U = 0.45\,\mathrm{V}$ and $I = 100\,\mathrm{pA}$. The corrugation profiles of the SiC (orange) and indenene side (blue) are depicted in **c**. A surface defect, marked by a red arrow in **a** and **b**, was used to align both profiles. The indenene lattice periodicity matches with the one from SiC(0001) proving the T1 adsorption site for In atoms. Adapted from the supplemental material of [110].

C.3 Normalization of STS data

As laid out in Section 4.2.3, the derivation of the tunneling current $I(U)$, i.e. $\mathrm{d}I/\mathrm{d}U$, is proportional to the local density of states at the sample surface (see Equation 4.12). However, with the transmission function still included, the resulting signal exhibits an exponential dependency on the tip-sample distance. To exclude any z-dependency of the transmission function the resulting signal is normalized with the conductance I/U leading to an expression of $\frac{\mathrm{d}I/\mathrm{d}U}{I/U}$ [189].

In the case of indenene, constant height STS measurements were mainly used to determine the charge localization asymmetry between the A and B side of the unit cell (see Sec. 8.4 for details). Here, only indium p-orbitals contribute to the transmission function $T(r, z, E, eU)$ at position $r = A$ and B for a constant distance z. The transmission function can therefore be safely assumed to be position independent:

$$T(A, z, E, eU) = T(B, z, E, eU) \equiv T(z, E, eU)\,. \tag{C.1}$$

Thus, the difference spectrum of the differential conductance depicted in Fig. C.4a was calculated to:

$$(\mathrm{d}I/\mathrm{d}U)_A - (\mathrm{d}I/\mathrm{d}U)_B \propto eT(z, eU, eU)(\rho(A, eU) - \rho(B, eU))\,. \tag{C.2}$$

In fact, the alternating sign switches in the curve, necessary to identify indenene as a QSHI, are already present here.

To exclude any transmission function dependency, Equation C.2 was further normalized with the tunneling conductance I_{avg}/U averaged over both sites A and B. The resulting spectrum is displayed in Fig. C.4b (cf. Fig. 8.6d). As can be seen, both curves represent qualitatively the

same behavior and clearly identify the topologically non-trivial character in indenene.

However, an individual normalization by site-specific I/U curves, i.e. $\frac{\mathrm{d}I/\mathrm{d}U_A}{I_A/U} - \frac{\mathrm{d}I/\mathrm{d}U_B}{I_B/U}$, would result in misleading site-dependent factors. These factors originate in different LDOS contributions on site A and B and would enter the tunneling current $I(U)$ expression given in Equation 4.9.

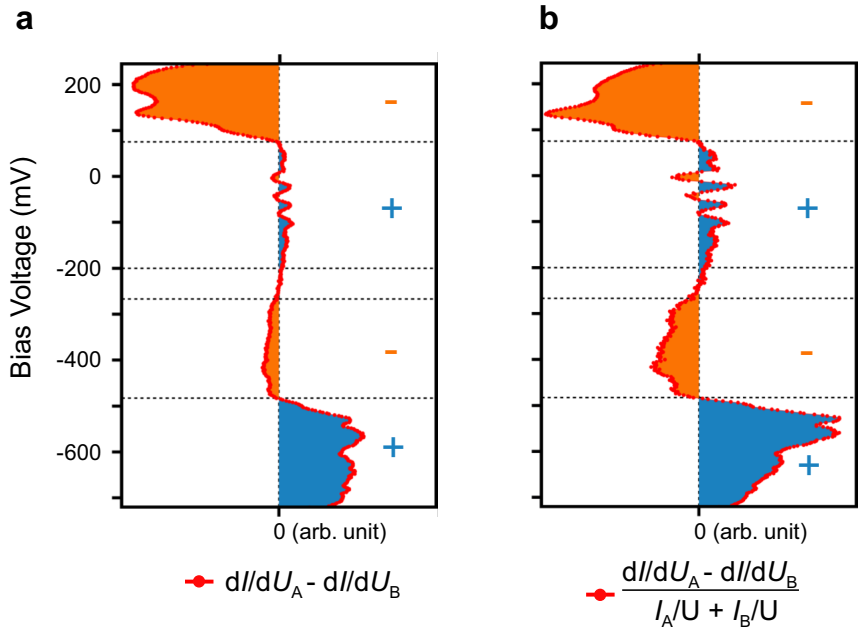

Figure C.4: Influence of normalization procedure on charge localization – **a**, Measured $\mathrm{d}I/\mathrm{d}U$ difference between the A and B site of the indenene unit cell according to expression C.2. **b**, Normalized $\mathrm{d}I/\mathrm{d}U$ difference between the A and B site of the indenene unit cell from experiment (cf. Fig. 8.6d). The normalization was conducted with the tunneling conductance I_{avg}/U averaged over both sites A and B. The spectra contain at least 30 averaged $\mathrm{d}I/\mathrm{d}U$ curves per site A and B, respectively. Adapted from the supplemental material of [110].

Bibliography

[1] F. Arute, K. Arya, R. Babbush, D. Bacon, J. C. Bardin, R. Barends, R. Biswas, S. Boixo, F. G. S. L. Brandao, D. A. Buell, B. Burkett, Y. Chen, Z. Chen, B. Chiaro, R. Collins, W. Courtney, A. Dunsworth, E. Farhi, B. Foxen, A. Fowler, C. Gidney, M. Giustina, R. Graff, K. Guerin, S. Habegger, M. P. Harrigan, M. J. Hartmann, A. Ho, M. Hoffmann, T. Huang, T. S. Humble, S. V. Isakov, E. Jeffrey, Z. Jiang, D. Kafri, K. Kechedzhi, J. Kelly, P. V. Klimov, S. Knysh, A. Korotkov, F. Kostritsa, D. Landhuis, M. Lindmark, E. Lucero, D. Lyakh, S. Mandrà, J. R. McClean, M. McEwen, A. Megrant, X. Mi, K. Michielsen, M. Mohseni, J. Mutus, O. Naaman, M. Neeley, C. Neill, M. Y. Niu, E. Ostby, A. Petukhov, J. C. Platt, C. Quintana, E. G. Rieffel, P. Roushan, N. C. Rubin, D. Sank, K. J. Satzinger, V. Smelyanskiy, K. J. Sung, M. D. Trevithick, A. Vainsencher, B. Villalonga, T. White, Z. J. Yao, P. Yeh, A. Zalcman, H. Neven, and J. M. Martinis, Nature **574**, 505 (2019).

[2] J. E. Moore, Nature **464**, 194 (2010).

[3] C. Nayak, S. H. Simon, A. Stern, M. Freedman, and S. Das Sarma, Reviews of Modern Physics **80**, 1083 (2008).

[4] M. He, H. Sun, and Q. L. He, Frontiers of Physics **14**, 43401 (2019).

[5] M. Z. Hasan and C. L. Kane, Reviews of Modern Physics **82**, 3045 (2010).

[6] X.-L. Qi and S.-C. Zhang, Physics Today **63**, 33 (2010).

[7] M. König, S. Wiedmann, C. Brüne, A. Roth, H. Buhmann, L. W. Molenkamp, X.-L. Qi, and S.-C. Zhang, Science **318**, 766 (2007).

[8] M. S. Lodge, S. A. Yang, S. Mukherjee, and B. Weber, Advanced Materials **33**, 2008029 (2021).

[9] A. Molle, J. Goldberger, M. Houssa, Y. Xu, S.-C. Zhang, and D. Akinwande, Nature Materials **16**, 163 (2017).

[10] C. L. Kane and E. J. Mele, Physical Review Letters **95**, 146802 (2005).

[11] C. L. Kane and E. J. Mele, Physical Review Letters **95**, 226801 (2005).

[12] H. Min, J. E. Hill, N. A. Sinitsyn, B. R. Sahu, L. Kleinman, and A. H. MacDonald, Physical Review B **74**, 165310 (2006).

[13] Y. Yao, F. Ye, X.-L. Qi, S.-C. Zhang, and Z. Fang, Physical Review B **75**, 041401 (2007).

[14] C.-C. Liu, W. Feng, and Y. Yao, Physical Review Letters **107**, 076802 (2011).

[15] Y. Xu, B. Yan, H.-J. Zhang, J. Wang, G. Xu, P. Tang, W. Duan, and S.-C. Zhang, Physical Review Letters **111**, 136804 (2013).

[16] J. Yuhara, Y. Fujii, K. Nishino, N. Isobe, M. Nakatake, L. Xian, A. Rubio, and G. L. Lay, 2D Materials **5**, 025002 (2018).

[17] T. Ogikubo, H. Shimazu, Y. Fujii, K. Ito, A. Ohta, M. Araidai, M. Kurosawa, G. Le Lay, and J. Yuhara, Advanced Materials Interfaces **7**, 1902132 (2020).

[18] Y. Liu, N. Gao, J. Zhuang, C. Liu, J. Wang, W. Hao, S. X. Dou, J. Zhao, and Y. Du, The Journal of Physical Chemistry Letters **10**, 1558 (2019).

[19] J. Gou, L. Kong, H. Li, Q. Zhong, W. Li, P. Cheng, L. Chen, and K. Wu, Physical Review Materials **1**, 054004 (2017).

[20] J. Deng, B. Xia, X. Ma, H. Chen, H. Shan, X. Zhai, B. Li, A. Zhao, Y. Xu, W. Duan, S.-C. Zhang, B. Wang, and J. G. Hou, Nature Materials **17**, 1081 (2018).

[21] F.-f. Zhu, W.-j. Chen, Y. Xu, C.-l. Gao, D.-d. Guan, C.-h. Liu, D. Qian, S.-C. Zhang, and J.-f. Jia, Nature Materials **14**, 1020 (2015).

[22] J. Li, T. Lei, J. Wang, R. Wu, J. Zhao, L. Zhao, Y. Guo, H. Qian, and K. Ibrahim, The Journal of Physical Chemistry C **124**, 4917 (2020).

[23] J. Li, T. Lei, J. Wang, R. Wu, H. Qian, and K. Ibrahim, Applied Physics Letters **116**, 101601 (2020).

[24] Y. Zang, T. Jiang, Y. Gong, Z. Guan, C. Liu, M. Liao, K. Zhu, Z. Li, L. Wang, W. Li, C. Song, D. Zhang, Y. Xu, K. He, X. Ma, S.-C. Zhang, and Q.-K. Xue, Advanced Functional Materials **28**, 1802723 (2018).

[25] L. Zhang, P. Bampoulis, A. N. Rudenko, Q. Yao, A. van Houselt, B. Poelsema, M. I. Katsnelson, and H. J. W. Zandvliet, Physical Review Letters **116**, 256804 (2016).

[26] F. Matusalem, F. Bechstedt, M. Marques, and L. K. Teles, Physical Review B **94**, 241403 (2016).

[27] D. Di Sante, P. Eck, M. Bauernfeind, M. Will, R. Thomale, J. Schäfer, R. Claessen, and G. Sangiovanni, Physical Review B **99**, 035145 (2019).

[28] J. J. Lander and J. Morrison, Surface Science **2**, 553 (1964).

[29] J. M. Nicholls, B. Reihl, and J. E. Northrup, Physical Review B **35**, 4137 (1987).

[30] J. E. Northrup, Physical Review Letters **53**, 683 (1984).

[31] R. J. Hamers, Physical Review B **40**, 1657 (1989).

[32] M. Gmitra, S. Konschuh, C. Ertler, C. Ambrosch-Draxl, and J. Fabian, Physical Review B **80**, 235431 (2009).

[33] G. Yang, L. Li, W. B. Lee, and M. C. Ng, Science and Technology of Advanced Materials **19**, 613 (2018).

[34] R. Saito, G. Dresselhaus, and M. S. Dresselhaus, *Physical Properties of Carbon Nanotubes* (Imperial College Press & Distributed by World Scientific Publishing Co. Pte. Ltd., 1998).

[35] K. S. Novoselov, A. K. Geim, S. V. Morozov, D. Jiang, M. I. Katsnelson, I. V. Grigorieva, S. V. Dubonos, and A. A. Firsov, Nature **438**, 197 (2005).

[36] A. H. Castro Neto, F. Guinea, N. M. R. Peres, K. S. Novoselov, and A. K. Geim, Reviews of Modern Physics **81**, 109 (2009).

[37] Y. Ren, Z. Qiao, and Q. Niu, Reports on Progress in Physics **79**, 066501 (2016).

[38] P. Avouris and C. Dimitrakopoulos, Materials Today **15**, 86 (2012).

[39] M. Tarnowski, F. N. Ünal, N. Fläschner, B. S. Rem, A. Eckardt, K. Sengstock, and C. Weitenberg, Nature Communications **10**, 1728 (2019).

[40] F. D. M. Haldane, Physical Review Letters **61**, 2015 (1988).

[41] S.-Q. Shen, *Topological Insulators: Dirac Equation in Condensed Matters*, 1st ed., Springer Series in Solid-State Sciences (Springer, Berlin, Heidelberg, 2012).

[42] M. Stockmeier, R. Müller, S. A. Sakwe, P. J. Wellmann, and A. Magerl, Journal of Applied Physics **105**, 033511 (2009).

[43] S. Eltinge and S. Ismail-Beigi, Physical Review Materials **6**, 014007 (2022).

[44] T. Kimoto, "Wide Bandgap Semiconductor Power Devices: Materials, Physics, Design, and Applications," (Elsevier Science - Woodhead Publishing, 2019) Chap. SiC material properties, pp. 21–42.

[45] K. Momma and F. Izumi, Journal of Applied Crystallography **44**, 1272 (2011).

[46] U. Starke, J. Schardt, and M. Franke, Applied Physics A **65**, 587 (1997).

[47] K. V. Emtsev, T. Seyller, L. Ley, A. Tadich, L. Broekman, J. D. Riley, R. C. G. Leckey, and M. Preuss, Surface Science **600**, 3845 (2006).

[48] K. V. Emtsev, T. Seyller, L. Ley, L. Broekman, A. Tadich, J. D. Riley, R. G. C. Leckey, and M. Preuss, Physical Review B **73**, 075412 (2006).

[49] T. Seyller, Applied Physics A **85**, 371 (2006).

[50] S. Glass, F. Reis, M. Bauernfeind, J. Aulbach, M. R. Scholz, F. Adler, L. Dudy, G. Li, R. Claessen, and J. Schäfer, The Journal of Physical Chemistry C **120**, 10361 (2016).

[51] G. S. Higashi, Y. J. Chabal, G. W. Trucks, and K. Raghavachari, Applied Physics Letters **56**, 656 (1990).

[52] G. W. Trucks, K. Raghavachari, G. S. Higashi, and Y. J. Chabal, Physical Review Letters **65**, 504 (1990).

[53] S. Miyazaki, J. Schäfer, J. Ristein, and L. Ley, Applied Physics Letters **68**, 1247 (1996).

[54] H. Tsuchida, I. Kamata, and K. Izumi, Applied Physics Letters **70**, 3072 (1997).

[55] S. Dhar, O. Seitz, M. D. Halls, S. Choi, Y. J. Chabal, and L. C. Feldman, Journal of the American Chemical Society **131**, 16808 (2009).

[56] T. Seyller, Journal of Physics: Condensed Matter **16**, 1755 (2004).

[57] S. Doğan, D. Johnstone, F. Yun, S. Sabuktagin, J. Leach, A. A. Baski, H. Morkoç, G. Li, and B. Ganguly, Applied Physics Letters **85**, 1547 (2004).

[58] M. W. Chase, *NIST-JANAF Thermochemical Tables - Fourth Edition - Part I*, 4th ed., Vol. Monograph No. 9 (Published by the American Chemical Society and the American Institute of Physics for the National Institute of Standards and Technology, 1998).

[59] C. Davisson and L. H. Germer, The Physical Review **30**, 705 (1927).

[60] M. P. Seah and W. A. Dench, Surface and Interface Analysis **1**, 2 (1979).

[61] S. Hüfner, *Photoelectron Spectroscopy: Principles and Applications*, 3rd ed., Advanced Texts in Physics (Springer, Berlin, Heidelberg, 2003).

[62] G. Ertl and J. Küppers, *Low Energy Electrons and Surface Chemistry*, 2nd ed. (VCH Verlagsgesellschaft mbH, Weinheim, 1985).

[63] M. Henzler and W. Göpel, *Oberflächenphysik des Festkörpers*, 2nd ed. (B. G. Teubner Stuttgart, Stuttgart, 1994).

[64] M. H. von Hoegen, Zeitschrift für Kristallographie - Crystalline Materials **214**, 591 (1999).

[65] G. Binnig, H. Rohrer, C. Gerber, and E. Weibel, Physical Review Letters **49**, 57 (1982).

[66] R. Wiesendanger, *Scanning Probe Microscopy and Spectroscopy: Methods and Applications* (Cambridge University Press, 1994).

[67] J. Tersoff and D. R. Hamann, Physical Review Letters **50**, 1998 (1983).

[68] J. Tersoff and D. R. Hamann, Physical Review B **31**, 805 (1985).

[69] R. J. Hamers, Annual Review of Physical Chemistry **40**, 531 (1989).

[70] C. J. Chen, Physical Review B **42**, 8841 (1990).

[71] A. Damascelli, Physica Scripta **2004**, 61 (2004).

[72] H. Hertz, Annalen der Physik **267**, 983 (1887).

[73] A. Einstein, Annalen der Physik **14**, 164 (1905).

[74] F. Reinert and S. Hüfner, New Journal of Physics **7**, 97 (2005).

[75] A. Lanzara, P. V. Bogdanov, X. J. Zhou, S. A. Kellar, D. L. Feng, E. D. Lu, T. Yoshida, H. Eisaki, A. Fujimori, K. Kishio, J.-I. Shimoyama, T. Noda, S. Uchida, Z. Hussain, and Z.-X. Shen, Nature **412**, 510 (2001).

[76] B. D. Ratner and D. G. Castner, "Electron Spectroscopy for Chemical Analysis," in *Surface Analysis – The Principal Techniques*, edited by J. C. Vickerman and I. S. Gilmore (John Wiley & Sons, Ltd, 2009) Chap. Chapter 3, pp. 47–112, 2nd ed.

[77] J. J. Yeh and I. Lindau, Atomic Data and Nuclear Data Tables **32**, 1 (1985).

[78] R. F. Reilman, A. Msezane, and S. T. Manson, Journal of Electron Spectroscopy and Related Phenomena **8**, 389 (1976).

[79] P. J. Cumpson and M. P. Seah, Surface and Interface Analysis **25**, 430 (1997).

[80] J. Zegenhagen, Japanese Journal of Applied Physics **58**, 110502 (2019).

[81] D. P. Woodruff, Progress in Surface Science **57**, 1 (1998).

[82] R. Gross and A. Marx, *Festkörperphysik*, 3rd ed. (Walter de Gruyter GmbH, 2018).

[83] S. Ansell, S. Krishnan, J. K. Weber, J. J. Felten, P. C. Nordine, M. A. Beno, D. L. Price, and M. L. Saboungi, Physical Review Letters **78**, 464 (1997).

[84] "Cold Lip SUMO Source for Aluminum - The Best Source for Aluminum Evaporation in MBE," Information retrieved on 18.04.2022.

[85] N. Sieber, T. Seyller, L. Ley, D. James, J. D. Riley, R. C. G. Leckey, and M. Polcik, Physical Review B **67**, 38 (2003).

[86] M. Bauernfeind, *Bismuten auf SiC(0001): Optimierung der Substratgüte und Charakterisierung des Materialsystems*, Master thesis, Julius-Maximilians-Universität Würzburg (2016).

[87] M. E. Straumanis and C. L. Woodward, Acta Crystallographica Section A **27**, 549 (1971).

[88] "LEEDpat4 (LEED pattern analyzer)," Information retrieved on 28.09.2021.

[89] A. Bauer, J. Kräusslich, P. Kuschnerus, K. Goetz, P. Käckell, and F. Bechstedt, Materials Science and Engineering: B **61-62**, 217 (1999).

[90] C. Wöll, S. Chiang, R. J. Wilson, and P. H. Lippel, Physical Review B **39** (1989).

[91] J. V. Barth, H. Brune, G. Ertl, and R. J. Behm, Physical Review B **42**, 9307 (1990).

[92] N. Takeuchi, C. T. Chan, and K. M. Ho, Physical Review B **43**, 13899 (1991).

[93] S. Narasimhan and D. Vanderbilt, Physical Review Letters **69**, 1564 (1992).

[94] F. Reinert and G. Nicolay, Applied Physics A: Materials Science and Processing **78**, 817 (2004).

[95] M. Will, *Growth and Characterization of Al on SiC(0001) and Ultrathin Sn layers on GaAs(111) - A Study by LEED and STM*, Master's thesis, Julius-Maximilians-Universität Würzburg (2018).

[96] C. Günther, J. Vrijmoeth, R. Q. Hwang, and R. J. Behm, Physical Review Letters **74** (1995), 10.1103/PhysRevLett.74.754.

[97] G. Pötschke, J. Schröder, C. Günther, R. Q. Hwang, and R. J. Behm, Surface Science **251-252**, 592 (1991).

[98] G. O. Pötschke, Physical Review B **44** (1991), 10.1103/PhysRevB.44.1442.

[99] S. Ouazi, T. Pohlmann, A. Kubetzka, K. Von Bergmann, and R. Wiesendanger, Surface Science **630**, 280 (2014).

[100] L. Seehofer, D. Daboul, G. Falkenberg, and R. L. Johnson, Surface Science **307-309**, 698 (1994).

[101] K. R. Elder, G. Rossi, P. Kanerva, F. Sanches, S. C. Ying, E. Granato, C. V. Achim, and T. Ala-Nissila, Physical Review Letters **108**, 1 (2012).

[102] K. R. Elder, G. Rossi, P. Kanerva, F. Sanches, S. C. Ying, E. Granato, C. V. Achim, and T. Ala-Nissila, Physical Review B **88**, 1 (2013).

[103] E. A. Khramtsova, A. V. Zotov, A. A. Saranin, S. V. Ryzhkov, A. B. Chub, and V. G. Lifshits, Applied Surface Science **82-83**, 576 (1994).

[104] B. M. McSkimming, A. Alexander, M. H. Samuels, B. Arey, I. Arslan, and C. J. K. Richardson, Journal of Vacuum Science & Technology A **35**, 021401 (2017).

[105] J. Erhardt, M. Bauernfeind, P. Eck, M. Kamp, J. Gabel, T.-L. Lee, S. Moser, G. Sangiovanni, and R. Claessen, "The phase diagram of In/SiC(0001): A roadmap to large scale growth of the quantum spin Hall insulator indenene," (2022), unpublished; in preparation for publication; After submission of this dissertation for evaluation, the manuscript referenced here was published as "Indium Epitaxy on SiC(0001): A Roadmap to Large Scale Growth of the Quantum Spin Hall Insulator Indenene" in The Journal of Physical Chemistry C **126**, 38, 16289-16296 (2022).

[106] N. Briggs, B. Bersch, Y. Wang, J. Jiang, R. J. Koch, N. Nayir, K. Wang, M. Kolmer, W. Ko, A. De La Fuente Duran, S. Subramanian, C. Dong, J. Shallenberger, M. Fu, Q. Zou, Y.-W. Chuang, Z. Gai, A.-P. Li, A. Bostwick, C. Jozwiak, C.-Z. Chang, E. Rotenberg, J. Zhu, A. C. T. van Duin, V. Crespi, and J. A. Robinson, Nature Materials **19**, 637 (2020).

[107] E. Rotenberg, H. Koh, K. Rossnagel, H. W. Yeom, J. Schäfer, B. Krenzer, M. P. Rocha, and S. D. Kevan, Physical Review Letters **91**, 1 (2003).

[108] T. Suzuki, J. Lawrence, M. Walker, J. M. Morbec, P. Blowey, K. Yagyu, P. Kratzer, and G. Costantini, Physical Review B **96**, 1 (2017).

[109] J. Kraft, M. Ramsey, and F. Netzer, Physical Review B **55**, 5384 (1997).

[110] M. Bauernfeind, J. Erhardt, P. Eck, P. K. Thakur, J. Gabel, T.-L. Lee, J. Schäfer, S. Moser, D. Di Sante, R. Claessen, and G. Sangiovanni, Nature Communications **12**, 5396 (2021).

[111] W. H. Choi, H. Koh, E. Rotenberg, and H. W. Yeom, Physical Review B **75**, 075329 (2007).

[112] H.-M. Guo and M. Franz, Physical Review B **80**, 113102 (2009).

[113] A. O'Brien, F. Pollmann, and P. Fulde, Physical Review B **81**, 235115 (2010).

[114] M. Kang, S. Fang, L. Ye, H. C. Po, J. Denlinger, C. Jozwiak, A. Bostwick, E. Rotenberg, E. Kaxiras, J. G. Checkelsky, and R. Comin, Nature Communications **11**, 4004 (2020).

[115] M. Kang, L. Ye, S. Fang, J.-S. You, A. Levitan, M. Han, J. I. Facio, C. Jozwiak, A. Bostwick, E. Rotenberg, M. K. Chan, R. D. McDonald, D. Graf, K. Kaznatcheev, E. Vescovo, D. C. Bell, E. Kaxiras, J. van den Brink, M. Richter, M. Prasad Ghimire, J. G. Checkelsky, and R. Comin, Nature Materials **19**, 163 (2020).

[116] S. G. Kwon and M. H. Kang, Physical Review B **89**, 165304 (2014).

[117] P. Eck, A. Consiglio, J. Erhardt, M. Bauernfeind, S. Moser, R. Claessen, D. Di Sante, and G. Sangiovanni, "Emergent Honeycomb Physics from Chiral Atomic Orbitals on the

Triangular Lattice," (2022), unpublished; in preparation for publication; After submission of this dissertation for evaluation, the manuscript referenced here was published as "Real-space obstruction in quantum spin Hall insulators" in Physical Review B **106**, 195143 (2022).

[118] F. Reis, G. Li, L. Dudy, M. Bauernfeind, S. Glass, W. Hanke, R. Thomale, J. Schäfer, and R. Claessen, Science **357**, 287 (2017).

[119] Y.-F. Jiang and H.-C. Jiang, Physical Review Letters **125**, 157002 (2020).

[120] K. Takada, H. Sakurai, E. Takayama-Muromachi, F. Izumi, R. A. Dilanian, and T. Sasaki, Nature **422**, 53 (2003).

[121] L. Balents, Nature **464**, 199 (2010).

[122] M. L. Kiesel, C. Platt, W. Hanke, and R. Thomale, Physical Review Letters **111**, 097001 (2013).

[123] C. Weber, A. Läuchli, F. Mila, and T. Giamarchi, Physical Review B **73**, 014519 (2006).

[124] Z. F. Wang, K.-H. Jin, and F. Liu, Nature Communications **7**, 12746 (2016).

[125] M. I. Aroyo, D. Orobengoa, G. de la Flor, E. S. Tasci, J. M. Perez-Mato, and H. Wondratschek, Acta Crystallographica Section A **70**, 126 (2014).

[126] D. Kochan, S. Irmer, and J. Fabian, Physical Review B **95**, 165415 (2017).

[127] M. Schüler, U. D. Giovannini, H. Hübener, A. Rubio, M. A. Sentef, and P. Werner, Science Advances **6** (2020), 10.1126/sciadv.aay2730.

[128] S. Cho, J.-H. Park, J. Hong, J. Jung, B. S. Kim, G. Han, W. Kyung, Y. Kim, S.-K. Mo, J. D. Denlinger, J. H. Shim, J. H. Han, C. Kim, and S. R. Park, Physical Review Letters **121**, 186401 (2018).

[129] S. Beaulieu, J. Schusser, S. Dong, M. Schüler, T. Pincelli, M. Dendzik, J. Maklar, A. Neef, H. Ebert, K. Hricovini, M. Wolf, J. Braun, L. Rettig, J. Minár, and R. Ernstorfer, Physical Review Letters **125**, 216404 (2020).

[130] M. Ünzelmann, H. Bentmann, T. Figgemeier, P. Eck, J. N. Neu, B. Geldiyev, F. Diekmann, S. Rohlf, J. Buck, M. Hoesch, M. Kalläne, K. Rossnagel, R. Thomale, T. Siegrist, G. Sangiovanni, D. Di Sante, and F. Reinert, Nature Communications **12**, 3650 (2021).

[131] J. P. Perdew, International Journal of Quantum Chemistry **28**, 497 (1985).

[132] A. Tadich, M. T. Edmonds, L. Ley, F. Fromm, Y. Smets, Z. Mazej, J. Riley, C. I. Pakes, T. Seyller, and M. Wanke, Applied Physics Letters **102**, 241601 (2013).

[133] P. H. Weidlich, R. E. Dunin-Borkowski, and P. Ebert, Physical Review B **84**, 085210 (2011).

[134] P. Lauffer, K. V. Emtsev, R. Graupner, T. Seyller, L. Ley, S. A. Reshanov, and H. B. Weber, Physical Review B **77**, 155426 (2008).

[135] S. Zhang, D. Huang, L. Gu, Y. Wang, and S. Wu, 2D Materials **8**, 035001 (2021).

[136] R. M. Feenstra and J. A. Stroscio, Journal of Vacuum Science & Technology B: Microelectronics Processing and Phenomena **5**, 923 (1987).

[137] L. J. Whitman, J. A. Stroscio, R. A. Dragoset, and R. J. Celotta, Physical Review B **42**, 7288 (1990).

[138] H. A. Al-Brithen, A. R. Smith, and D. Gall, Physical Review B **70**, 045303 (2004).

[139] F. Ming, T. S. Smith, S. Johnston, P. C. Snijders, and H. H. Weitering, Physical Review B **97**, 075403 (2018).

[140] Y. Zhang, V. W. Brar, F. Wang, C. Girit, Y. Yayon, M. Panlasigui, A. Zettl, and M. F. Crommie, Nature Physics **4**, 627 (2008).

[141] V. Y. Butko, J. F. DiTusa, and P. W. Adams, Physical Review Letters **84**, 1543 (2000).

[142] D. P. Woodruff, B. C. C. Cowie, and A. R. H. F. Ettema, Journal of Physics: Condensed Matter **6**, 10633 (1994).

[143] J. L. Collins, A. Tadich, W. Wu, L. C. Gomes, J. N. B. Rodrigues, C. Liu, J. Hellerstedt, H. Ryu, S. Tang, S.-K. Mo, S. Adam, S. A. Yang, M. S. Fuhrer, and M. T. Edmonds, Nature **564**, 390 (2018).

[144] S. Baba, H. Hirayama, J. M. Zhou, and A. Kinbara, Thin Solid Films **90**, 57 (1982).

[145] H. Öfner, S. L. Surnev, Y. Shapira, and F. P. Netzer, Physical Review B **48**, 10940 (1993).

[146] Z. Gai, R. G. Zhao, Y. He, H. Ji, C. Hu, and W. S. Yang, Physical Review B **53**, 1539 (1996).

[147] T. Ichikawa, Surface Science **111**, 227 (1981).

[148] D. V. Gruznev, D. A. Olyanich, D. N. Chubenko, A. V. Zotov, and A. A. Saranin, Physical Review B **76**, 073307 (2007).

[149] H. W. Yeom, S. Takeda, E. Rotenberg, I. Matsuda, K. Horikoshi, J. Schaefer, C. M. Lee, S. D. Kevan, T. Ohta, T. Nagao, and S. Hasegawa, Physical Review Letters **82**, 4898 (1999).

[150] T. Zhang, P. Cheng, W.-J. Li, Y.-J. Sun, G. Wang, X.-G. Zhu, K. He, L. Wang, X. Ma, X. Chen, Y. Wang, Y. Liu, H.-Q. Lin, J.-F. Jia, and Q.-K. Xue, Nature Physics **6**, 104 (2010).

[151] S. Yamazaki, Y. Hosomura, I. Matsuda, R. Hobara, T. Eguchi, Y. Hasegawa, and S. Hasegawa, Physical Review Letters **106**, 116802 (2011).

[152] T. Wagner, *Working title: Characterization of Sb-based surface reconstructions on Ag(111), InSb(111) and SiC(0001) & Oxidation of monolayer lattices of (In, Bi, Sb) on SiC(0001)*, Ph.D. thesis, Julius-Maximilians-Universität Würzburg, unpublished; in preparation.

[153] R. C. Wicks and N. J. C. Ingle, Review of Scientific Instruments **80**, 053108 (2009).

[154] C. J. Powell and A. Jablonski, *NIST Electron Inelastic-Mean-Free-Path Database*, Vol. Version 1.2 (National Institute of Standards and Technology, Gaithersburg (MD, USA), 2010).

[155] H. Ando, A. Visikovskiy, T. Nakagawa, S. Mizuno, and S. Tanaka, Physical Review B **99**, 235434 (2019).

[156] W. A. de Heer, C. Berger, M. Ruan, M. Sprinkle, X. Li, Y. Hu, B. Zhang, J. Hankinson, and E. Conrad, Proceedings of the National Academy of Sciences **108**, 16900 (2011).

[157] D. Chiappe, E. Scalise, E. Cinquanta, C. Grazianetti, B. van den Broek, M. Fanciulli, M. Houssa, and A. Molle, Advanced Materials **26**, 2096 (2014).

[158] L. Vitali, M. G. Ramsey, and F. P. Netzer, Physical Review B **63**, 165320 (2001).

[159] P. Vogt, P. De Padova, C. Quaresima, J. Avila, E. Frantzeskakis, M. C. Asensio, A. Resta, B. Ealet, and G. Le Lay, Physical Review Letters **108**, 155501 (2012).

[160] L. Meng, Y. Wang, L. Zhang, S. Du, R. Wu, L. Li, Y. Zhang, G. Li, H. Zhou, W. A. Hofer, and H.-J. Gao, Nano Letters **13**, 685 (2013).

[161] A. Fleurence, R. Friedlein, T. Ozaki, H. Kawai, Y. Wang, and Y. Yamada-Takamura, Physical Review Letters **108**, 245501 (2012).

[162] L. I. Johansson, F. Owman, and P. Mårtensson, Surface Science **360**, L478 (1996).

[163] S. Forti, A. Stöhr, A. A. Zakharov, C. Coletti, K. V. Emtsev, and U. Starke, 2D Materials **3**, 035003 (2016).

[164] A. Kawazu and H. Sakama, Physical Review B **37**, 2704 (1988).

[165] M. A. Olmstead, R. D. Bringans, R. I. G. Uhrberg, and R. Z. Bachrach, Physical Review B **34**, 6041 (1986).

[166] R. D. Bringans, R. I. G. Uhrberg, R. Z. Bachrach, and J. E. Northrup, Physical Review Letters **55**, 533 (1985).

[167] M. E. Dávila, L. Xian, S. Cahangirov, A. Rubio, and G. Le Lay, New Journal of Physics **16**, 095002 (2014).

[168] M. Derivaz, D. Dentel, R. Stephan, M.-C. Hanf, A. Mehdaoui, P. Sonnet, and C. Pirri, Nano Letters **15**, 2510 (2015).

[169] L. Li, S.-z. Lu, J. Pan, Z. Qin, Y.-q. Wang, Y. Wang, G.-y. Cao, S. Du, and H.-J. Gao, Advanced Materials **26**, 4820 (2014).

[170] P. Rosenzweig and U. Starke, Physical Review B **101**, 201407 (2020).

[171] S. Hayashi, A. Visikovskiy, T. Kajiwara, T. Iimori, T. Shirasawa, K. Nakastuji, T. Miyamachi, S. Nakashima, K. Yaji, K. Mase, F. Komori, and S. Tanaka, Applied Physics Express **11**, 015202 (2017).

[172] C.-Y. Park, T. Abukawa, T. Kinoshita, Y. Enta, and S. Kono, Japanese Journal of Applied Physics **27**, 147 (1988).

[173] S. Glass, G. Li, F. Adler, J. Aulbach, A. Fleszar, R. Thomale, W. Hanke, R. Claessen, and J. Schäfer, Physical Review Letters **114**, 247602 (2015).

[174] R. I. G. Uhrberg, H. M. Zhang, T. Balasubramanian, S. T. Jemander, N. Lin, and G. V. Hansson, Physical Review B **62**, 8082 (2000).

[175] P. J. Estrup and J. Morrison, Surface Science **2**, 465 (1964).

[176] T. Ichikawa and S. Ino, Surface Science **105**, 395 (1981).

[177] S. Okada, Y. Kishikawa, K. Oura, and T. Hanawa, Surface Science **100**, L457 (1980).

[178] S. Forti, S. Link, A. Stöhr, Y. Niu, A. A. Zakharov, C. Coletti, and U. Starke, Nature Communications **11**, 2236 (2020).

[179] S. S. Lee, H. J. Song, N. D. Kim, J. W. Chung, K. Kong, D. Ahn, H. Yi, B. D. Yu, and H. Tochihara, Physical Review B **66**, 233312 (2002).

[180] S. Hatta, C. Kato, N. Tsuboi, S. Takahashi, H. Okuyama, T. Aruga, A. Harasawa, T. Okuda, and T. Kinoshita, Physical Review B **76**, 075427 (2007).

[181] G. Bihlmayer, J. Sassmannshausen, A. Kubetzka, S. Blügel, K. von Bergmann, and R. Wiesendanger, Physical Review Letters **124**, 126401 (2020).

[182] T. Okuda, H. Daimon, H. Shigeoka, S. Suga, T. Kinoshita, and A. Kakizaki, Journal of Electron Spectroscopy and Related Phenomena **80**, 229 (1996), proceedings of the 11th International Conference on Vacuum Ultraviolet Radiation Physics.

[183] P. B. Howes, C. Norris, M. S. Finney, E. Vlieg, and R. G. van Silfhout, Physical Review B **48**, 1632 (1993).

[184] E. Hilner, A. Mikkelsen, J. Eriksson, J. N. Andersen, E. Lundgren, A. Zakharov, H. Yi, and P. Kratzer, Applied Physics Letters **89**, 251912 (2006).

[185] L. Seehofer, G. Falkenberg, and R. L. Johnson, Surface Science **290**, 15 (1993).

[186] R. Shioda, A. Kawazu, A. A. Baski, C. F. Quate, and J. Nogami, Physical Review B **48**, 4895 (1993).

[187] Y. Ohtsubo, S. Hatta, M. Iwata, K. Yaji, H. Okuyama, and T. Aruga, Journal of Physics: Condensed Matter **21**, 405001 (2009).

[188] J. P. Perdew, K. Burke, and M. Ernzerhof, Phys. Rev. Lett. **77**, 3865 (1996).

[189] R. M. Feenstra, J. A. Stroscio, and A. P. Fein, Surface Science **181**, 295 (1987).

List of own publications

- P. Eck, C. Ortix, A. Consiglio, J. Erhardt, M. Bauernfeind, S. Moser, R. Claessen, D. Di Sante, and G. Sangiovanni, *Real-space obstruction in quantum spin Hall insulators*, Physical Review B **106**, 195143 (2022)
  This article was published after the submission of this dissertation and was therefore not considered in the evaluation of the dissertation.

- J. Erhardt, M. Bauernfeind, P. Eck, M. Kamp, J. Gabel, T.-L. Lee, G. Sangiovanni, S. Moser, and R. Claessen, *Indium Epitaxy on SiC(0001): A Roadmap to Large Scale Growth of the Quantum Spin Hall Insulator Indenene*, The Journal of Physical Chemistry C **126**, 38, 16289-16296 (2022)
  This article was published after the submission of this dissertation and was therefore not considered in the evaluation of the dissertation.

- M. Bauernfeind, J. Erhardt, P. Eck, P. K. Thakur, J. Gabel, T.-L. Lee, J. Schäfer, S. Moser, D. Di Sante, R. Claessen, and G. Sangiovanni, *Design and realization of topological Dirac fermions on a triangular lattice*, Nature Communications **12**, 5396 (2021)

- V. A. Rogalev, F. Reis, F. Adler, M. Bauernfeind, J. Erhardt, A. Kowalewski, M. R. Scholz, L. Dudy, L. B. Duffy, T. Hesjedal, M. Hoesch, G. Bihlmayer, J. Schäfer, and R. Claessen, *Tailoring the topological surface state in ultrathin α-Sn(111) films*, Physical Review B **100**, 245144 (2019)

- T. Rauch, V. A. Rogalev, M. Bauernfeind, J. Maklar, F. Reis, F. Adler, S. Moser, J. Weis, T.-L. Lee, P. K. Thakur, J. Schäfer, R. Claessen, J. Henk, and I. Mertig, *Nontrivial topological valence bands of common diamond and zinc-blende semiconductors*, Phyiscal Review Materials **3**, 064203 (2019)

- D. Di Sante, P. Eck, M. Bauernfeind, M. Will, R. Thomale, J. Schäfer, R. Claessen, and G. Sangiovanni, *Towards topological quasifreestanding stanene via substrate engineering*, Physical Review B **99**, 035145 (2019)

- F. Reis, G. Li, L. Dudy, M. Bauernfeind, S. Glass, W. Hanke, R. Thomale, J. Schäfer, and R. Claessen, *Bismuthene on a SiC substrate: A candidate for a high-temperature quantum spin Hall material*, Science **357**, 287-290 (2017)

- S. Glass, F. Reis, M. Bauernfeind, J. Aulbach, M. R. Scholz, F. Adler, L. Dudy, G. Li, R. Claessen, and J. Schäfer, *Atomic-Scale Mapping of Layer-by-Layer Hydrogen Etching and Passivation of SiC(0001) Substrates*, The Journal of Physical Chemistry C **120**, 10361–10367 (2016)

Danksagung

An dieser Stelle möchte ich mich bei allen Menschen bedanken, die mich während meines Studiums und der Promotion begleitet und unterstützt haben.

Bei Herrn Prof. Dr. Ralph Claessen bedanke ich mich für die Aufnahme an seinen Lehrstuhl der Experimentellen Physik IV und die mir gegebene Möglichkeit meine Promotion dort durchzuführen. Durch sein fortwährendes Interesse an meiner Arbeit und seinen kritischen Fragen ermöglichte er mir ein tiefgreifenderes Verständnis der physikalischen Vorgänge. Zudem unterstützte er mich in eher schwierigeren und turbulenten Zeiten wo es nur ging und hatte für mich immer ein offenes Ohr. Bei meinem Doktorvater Prof. Dr. Jörg Schäfer bedanke ich mich für die Unterstützung und die Labor-Diskussionen, aus denen über die Jahre viele tolle Ideen hervorgeganen sind. Die hilfreichen und auf den Punkt formulierten Kommentare und Fragestellungen zu meiner Arbeit, Papern, Postern, und allerlei Abstracts haben mich einiges gelehrt, das ich auch im weiteren Leben noch durchaus gebrauchen kann. Auch möchte ich mich bei ihm für die entgegengebrachte Motivation bedanken, die mich immer wieder ermutigt hat mich neuen Herausforderungen zu stellen. Meinem Kollegen Jonas Erhardt danke ich sehr für die gute kollegiale Zusammenarbeit im Labor und Büro, sowie die großartige Unterstützung bei allerlei Messungen und Auswertungen. Ohne ihn wäre das Indium-Projekt mit Sicherheit nicht so weit fortgeschritten. Auch für das Korrekturlesen meiner Arbeit möchte ich mich an dieser Stelle bedanken. Dem Arbeitsgruppenleiter des Nano-Teams Dr. Simon Moser danke ich für die strukturierte Leitung und das Korrekturlesen meiner Dissertation mit vielen hilfreichen und kritischen Vorschlägen, die mir oft völlig neue Sichtweisen auf Problemstellungen ermöglicht haben.

Den Postdocs des Nano-Teams, allen voran Dr. Lenart Dudy und Dr. Victor Rogalev, die die ARPES- und Präparationskammer in Schuss gehalten haben, gebührt auch ein sehr großer Dank. Daneben haben sie mich auch bei Photoemissionsmessungen und -auswertungen tatkräftig unterstützt, von legendären Messzeiten an Synchrotrons ganz zu schweigen. Die neueren Postdocs Dr. Bing Liu und Dr. Kyungchan Lee sollten hierbei natürlich nicht vergessen werden. Ich bedanke mich für die tolle Unterstützung am STM und im ARPES-Labor. Meinen Kollegen aus dem Nano-Team Florian Adler, Alexander Burger, Jonas Erhardt, André Kowalewski, Julian Maklar, Felix Reis, Raúl Stühler, Tim Wagner, Johannes Weis und Jan Wittemann möchte ich für die tolle Zeit, kollegiale Zusammenarbeit, und vielen Hilfestellungen im Labor über die Jahre außerordentlich danken. Im Laufe meiner Jahre in der EP4 hatte ich auch die Möglichkeit einige Bachelor- und Masterstudenten zu betreuen. Durch ihre hervorragende Arbeit, Fleiß, und tollen Ideen haben sich die Projekte, die auch in diese Arbeit eingeflossen sind, enorm

weiterentwickelt. Ich bedanke mich hier insbesondere bei Marius Will und Jonas Erhardt. Bei meinen vielen anderen Arbeitskollegen aus der EP4 möchte ich mich für die sehr schönen Jahre und die familiäre Arbeitsatmosphäre bedanken. Mit euch war es eine ganz wunderbare und unvergessliche Zeit.

Ein großes Dankeschön geht auch an Prof. Dr. Giorgio Sangiovanni, Dr. Domenico Di Sante, und Philipp Eck aus der Theoretischen Physik, mit denen wir eine enorm ergebnisreiche Kollaboration auf kollegialer Basis haben konnten. An dieser Stelle möchte ich mich auch bei Philipp Eck für das Korrekturlesen meiner Arbeit, insbesondere der Theorie-Kapitel, bedanken. I would also like to gratefully acknowledge the beamline staff at I09 from Diamond Light Source, in particular Dr Tien-Lin Lee, Dr Pardeep Kumar Thakur, and Dr Judith Gabel, for the fast XSW and LEED measurements with analysis, including the prompt UHV suitcase deliveries and assistance.

Bei der Wissenschaftlichen Werkstatt unter der Leitung von Dr. Utz Baß bedanke ich mich für die langjährige Zusammenarbeit, Hilfestellungen, und die präzisen Anfertigungen verschiedenster Teile für unsere Vorhaben im Labor. Ein ganz besonderen Dank gebührt hier Rainer Brauner und seinem Team. Auch dem Team der Helium-Verflüssigung um Cornelius Ziga und Roland Ebert danke ich sehr für die Bereitstellung von flüssigem Helium und Stickstoff und anderen technischen Hilfen im Labor. Im Weiteren möchte ich auch noch Monika Seifer für die administrative Unterstützung während meiner Promotion danken. Durch ihr unermüdliches Handeln und die Hilfen bei so vielen bürokratischen Hürden, die während der Promotion auftraten, hielt sie alles am Laufen. Zusammen mit Monika Armer aus dem SFB-Büro danke ich beiden auch für die tatkräftige Unterstützung während der Organisation der "4th International Fall School ToCoTronics 2018" in Würzburg.

Zu guter Letzt gebührt ein großer Dank meiner Familie und meinen Freunden, die mich auf dem langen Weg meines Studiums und der Promotion begleitet und unterstützt haben. Hier gilt ein ganz besonders großer Dank meinen Eltern und meiner Schwester samt Familie, die immer für mich da waren. I also would like to thank my girlfriend Daphne and her family in the U.S. and Greece for their great support and encouragement and the wonderful time I was able to spend with them during my PhD. Meinen besten Freunden aus Schulzeiten Florian, Simon, und Tobias danke ich auch für die tollen Pokerabende und andere Ausflüge, die mir immer eine nette Ablenkung zu meinem Studium und meiner Promotion geboten haben.